University of Alabama in Huntsville

## LOUIS

2021

# Network based pressure drop modeling of heterogeneous porous hybrid rocket motor grains

Joseph Robert Kennedy Buckley

Follow this and additional works at: https://louis.uah.edu/uah-dissertations

## Recommended Citation

# NETWORK BASED PRESSURE DROP MODELING OF

# HETEROGENEOUS POROUS HYBRID ROCKET
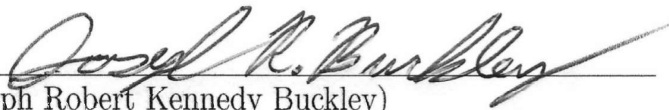
# MOTOR GRAINS

by

## JOSEPH ROBERT KENNEDY BUCKLEY

## A DISSERTATION

Submitted in partial fulfillment of the requirements
for the degree of Doctor of Philosophy
in
The Department of Mechanical and Aerospace Engineering
to
The School of Graduate Studies
of
The University of Alabama in Huntsville

HUNTSVILLE, ALABAMA

2021

In presenting this dissertation in partial fulfillment of the requirements for a doctoral degree from The University of Alabama in Huntsville, I agree that the Library of this University shall make it freely available for inspection. I further agree that permission for extensive copying for scholarly purposes may be granted by my advisor or, in his/her absence, by the Chair of the Department or the Dean of the School of Graduate Studies. It is also understood that due recognition shall be given to me and to The University of Alabama in Huntsville in any scholarly use which may be made of any material in this dissertation.

(Joseph Robert Kennedy Buckley)                    3/18/21
                                                    (date)

# DISSERTATION APPROVAL FORM

Submitted by Joseph Robert Kennedy Buckley in partial fulfillment of the requirements for the degree of Doctor of Philosophy in Mechanical Engineering and accepted on behalf of the Faculty of the School of Graduate Studies by the dissertation committee.

We, the undersigned members of the Graduate Faculty of The University of Alabama in Huntsville, certify that we have advised and/or supervised the candidate of the work described in this dissertation. We further certify that we have reviewed the dissertation manuscript and approve it in partial fulfillment of the requirements for the degree of Doctor of Philosophy in Mechanical Engineering.

| | | |
|---|---|---|
| Dr. George J. Nelson | 3/23/21 (Date) | Committee Chair |
| Dr. Robert A. Frederick | 3/15/2021 (Date) | |
| Dr. Jason Cassibry | 3/15/21 (Date) | |
| Dr. David Lineberry | 3/23/21 (Date) | |
| Dr. Gabe Xu | 3/15/21 (Date) | |
| Dr. Keith Hollingsworth | 3/26/2021 (Date) | Department Chair |
| Dr. Shankar Mahalingam | Digitally signed by Shankar Mahalingam Date: 2021.03.31 16:56:05 -05'00' (Date) | College Dean |
| Dr. Sean Lane | Yeqing Bao 4/1/2021 (Date) | Acting Associate Graduate School Provost |
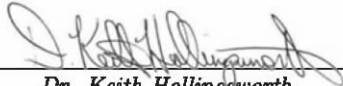
# ABSTRACT

School of Graduate Studies
The University of Alabama in Huntsville

Degree  <u>Doctor of Philosophy</u>  College/Dept. <u>Engineering/Mechanical and</u>

<u>Aerospace Engineering</u>

Name of Candidate  <u>Joseph Robert Kennedy Buckley</u>

Title  <u>Network Based Pressure Drop Modeling of</u>

<u>Heterogeneous Porous Hybrid Rocket Motor Grains</u>

Analytic Transport Network Theory (ATN), a heuristic model developed for electrochemical systems, is adapted to predict the gas pressure drop across heterogeneous porous hybrid rocket motor grains. Experimental pressure drop estimations from previous studies of these grains disagree with existing empirical correlations that assume uniform morphology. An adapted ATN model could significantly improve the gas pressure drop prediction with relatively low resource requirements. To test the applicability of ATN, porous hybrid motor grain samples with length 40 mm, diameter 20 mm, and nominal pore size (NPS) of 200 and 100 microns, based on manufacturer specifications, were studied using microstructural analysis and pressure drop measurements. Microstructural data for twenty samples was acquired via x-ray computed tomography (XCT) at a pixel size of $\sim$32 microns. Pore and solid regions were segmented using visual inspection and comparison to a plexiglass calibration sample. Microstructural properties including porosity, phase size distributions, and ATN-based transport coefficients were estimated from the segmented data. A baseline resistance was derived from the estimated pressure drop for an empirical correlation

applied to a highly porous case. Using the baseline result in combination with the ATN predicted transport coefficient ratio, an equivalent resistance is calculated to estimate the pressure drop as a function of Reynolds number (Re). Grain porosities of approximately 50% were estimated with the XCT data. These estimates agreed well with estimates from the Archimedes method. XCT data indicated the porous 200 and 100 NPS grains had average pore diameters of 339 and 356 microns, respectively. These pore sizes were verified by comparison to higher resolution XCT data and scanning electron microscope data. After imaging, the pressure drop was measured for ten grains of each NPS for 200 $<$Re $<$16000. The measured pressure drops ranged from less than 1 psig to 200 psig. ATN model predictions agreed well with experimental measurements. Computational times and memory required were relatively low, resulting in a very resource-efficient modeling approach. The results presented are among the first experimental validations of a novel modeling approach that may enable the rapid design and optimization of heterogeneous porous hybrid motor grains in various applications.

Abstract Approval:  Committee Chair   _____

                                       *Dr. George J. Nelson*

            Department Chair   _____  3/26/2021

                                      *Dr. Keith Hollingsworth*

Acting Associate
Graduate School
Provost                 *Yeqing Bao  4/1/2021*

                          _____
                            *Dr. Sean Lane*

# ACKNOWLEDGMENTS

Dr. John Bennewitz, Evan Unruh, Joseph Agnew, Dr. Matthew Hitt, Hernando Gonzalez, Prehit Patel, Gabriela Martines, and Zach Van Zandt.

Finally, I would like to thank my parents for their support throughout this and all of my life endeavours. I would like to thank Dr. Williams, Dr. Marais, Dr. Longuski, Dr. Heister, Dr. Collicott, and Dr. Shih from Purdue University for taking a leap of faith in recommending me in my graduate studies. I want to thank Ryan Pratt, Ben Hutchins, Cory Sell, Hernando Gonzalez, Shannon Hagarty, Dan Yap, Brian Kennedy, and Ryan Schultz. You are my closest friends, and I stand strong because of you.

# TABLE OF CONTENTS

# LIST OF FIGURES

# LIST OF TABLES

# LIST OF SYMBOLS

| SYMBOL | DEFINITION |
|--------|------------|
| $\delta$ | Symbol of Change |
| $\epsilon$ | Porosity (Ratio of Porous Volume to Total Volume) |
| $\mu$ | Coefficient of viscosity (N-s/m) |
| $\rho$ | Density (kg/m$^3$) |
| p | Static Pressure |
| $A$ | Area ($m^2$) |
| $A_c$ | Cross sectional area ($m^2$) |
| $A_g$ | Porous hybrid grain area ($m^2$) |
| $A_{crit}$ | Critical flow choke area ($m^2$) |
| $A_*$ | Sonic area ($m^2$) |
| $D_p$ | Average solid particle diameter ($\mu m$) |
| $f_p$ | Friction factor |
| $Re$ | Reynolds number |
| $Re_m$ | Modified reynolds number |
| $Re_1$ | Modified reynolds number |
| $R_{RSVcirc}$ | Radial representative sub volume radius (mm) |

| | |
|---|---|
| $R_{RSVaxial}$ | Axial representative sub volume length (mm) |
| $u$ | Velocity |
| $u_{p1}$ | Sample upstream pressure transducer uncertainty |
| $u_{p2}$ | Sample downstream pressure transducer uncertainty |
| $\epsilon$ | Porosity |
| $\sigma$ | Standard deviation |
| $\xi$ | Total uncertainty |
| $\mu_{mat,min}$ | Baseline transport coefficient $(m^2/s$ |
| $\mu_{eff}$ | Effective transport coefficient $(m^2/s$ |
| $W$ | Mass (kg) |
| $V$ | Volume $(m^3)$ |
| $R$ | Resistance $(Pa/kg/m^2 - s)$ $(Psig/lbm/ft^2 - s)$ |
| $\frac{\Delta p}{L}$ | Pressure drop per unit length |
| $\rho$ | Density $(kg/m^3)$ |

*For Grandpa, Brian, and all those that risk there lives for the defense of freedom.*

*"For God did not give us a spirit of timidity, but a spirit of power, of love, and of self-discipline."*

—2 Timothy 1:7

# CHAPTER 1

# INTRODUCTION

*A theory can be proven by experiment; but
no path leads from experiment to the birth
of a theory.*

—Albert Einstein

## 1.1  Motivation

Porous media serve a wide range of purposes in daily life. These applications
include battery electrodes [10], models for soil beds [11], and the sponges used for
regular household maintenance. The flow behavior of porous media within these
examples at low speeds are fairly well understood, but there is one case that provides
an interesting and novel challenge: the use of a porous material as a hybrid rocket
fuel. In many porous media examples, from soil beds to hybrid rocket motors, there
is one parameter of great interest: the pressure drop of the fluid while traveling
through the porous medium. While many empirical models of pressure drop behavior
exist for common applications, few cover the flow regime of high Reynolds numbers
(Re). Furthermore, many of these empirical models focus on packed particle beds, in
which general bulk properties are assumed to accurately describe the entire porous
structure. In this circumstance, evaluating a specific controlled porous geometry

that deviates from a homogeneous structure is difficult as this violates governing assumptions supporting the current suite of models based on empirical correlations. The challenge of evaluating porous medium flow behavior is compounded if one seeks to design a porous medium to achieve a desired objective, such as a target pressure drop to support combustion. In these cases, a more detailed understanding of the porous medium's structure and computationally efficient methods to predict its flow behavior are desirable.

## 1.2 Rocket Propulsion Fundamentals

While porous media are perhaps most noteworthy in other engineering applications such as soil behavior, catalysis, and energy conversion and storage, they have recently seen an increased use in the aerospace field as well. Specifically, porous media have recently seen action in aerospace applications such as catalyst beds for mono-propellant reactions [12], flashback arrestors for fuel injectors [13], and heat-shield material [14]. Among aerospace applications, porous hybrid rocket motors present an intriguing application of porous media that is the focus of the present work [15] [3] [16]. In order to appreciate their full use of porous media in aerospace applications, it is helpful to have an understanding of the fundamental concepts relevant to the systems in which they are used.

Rocket propulsion systems operate by Newton's Second Law of Motion. By accelerating a propellant in a chamber and expanding it through a nozzle, momentum is imparted on the parent system. The most common propulsion systems in rockets today are chemical propulsion systems that primarily operate through combustion.

Combustion is a process that is encountered in countless facets of everyday life. The easiest analogy to use is that of a campfire. The campfire generally needs three things to exist: fuel, oxidizer, and the right ignition conditions. The fuel is usually the wood logs in the pit, the oxidizer is the air we all breathe, and the right ignition conditions are provided by the match used to start the fire.

Chemical rockets need the same things, and the form in which the first two ingredients is provided is often the defining characteristic of the system. They come in three types: solid, liquid, and hybrid.
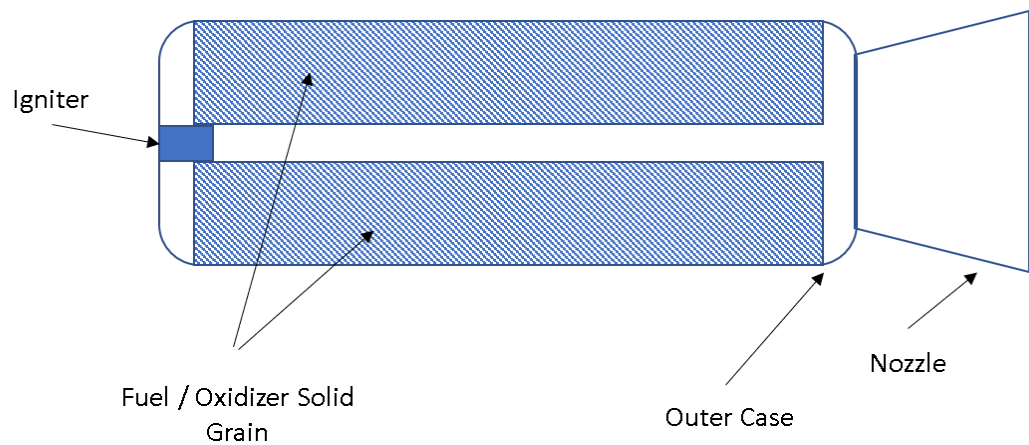


**Figure 1.1**: Typical Solid Rocket Motor [1]

In a solid rocket propulsion system, the fuel and oxidizer are mixed together in one solid material defined as a propellant( Figure 1.1). The "match" in this system usually consists of a special igniter. This can be an electrical wire with a small piece of flammable material that combusts when an electrical current travels through the wire, or it can be a full torch. A solid rocket propulsion system's advantages over its liquid and hybrid counterparts can be summed up in one word: simplicity. There

are few moving parts (though some systems have adjusting nozzles and actuators), require little servicing, and can be stored for long periods of time [1]. Ignition is usually very simple: light the surface with an igniter (i.e. match) and let it burn to completion. The regression rate, the rate at which a solid rocket material burn surface propagates, is often described by St. Robert's Law [1]:

$$r = aP_o{}^n \qquad (1.1)$$

However, there are disadvantages to solid propellants as well. The simplicity of the propulsion system requires the sacrifice of burn rate control. Once the motor is ignited, it will burn to completion at a rate that typically isn't actively controlled. The specific impulse, the rocket's "miles per gallon" fuel efficiency, is also typically lower than its liquid counterparts.
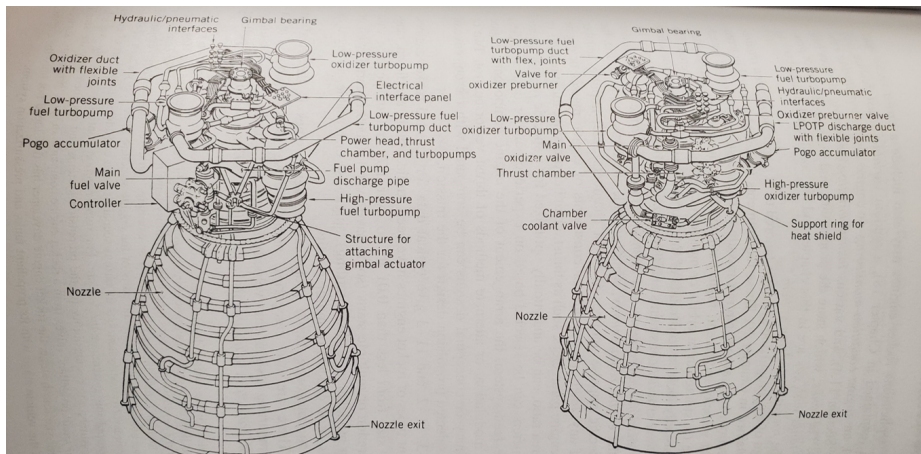


**Figure 1.2**: Two views of the Space Shuttle Main Engine (SSME), a liquid propulsion system [1]

Liquid rockets are the second category of chemical propulsion systems. In these systems the fuel and oxidizer are stored as liquids. Stored separately they are known as bipropellant systems, and stored together as one propellant they are classified as monopropellant systems. While solid rocket propulsion systems are commonly referred to as motors, liquid rocket propulsion systems are termed as engines. Sutton describes a rocket engine as containing one or more thrust chambers, a feed mechanism source to provide energy for the feed mechanism, suitable plumbing or piping to transfer liquid propellants, a structure to transmit the thrust force, and control devices (including valves) to start and stop and sometimes also vary the propellant flow and thus the thrust [1]. As one can see in Figure 1.2, a liquid propulsion system is often much more complicated than its solid counterpart. The advantage to this added complexity is more control over the burning process. The pumps can often be adjusted to alter the flow rate of fuel and oxidizer, allowing the rocket to be throttled or even completely shut down and restarted. The specific impulse of these rockets is typically higher as well. The main disadvantage to this added complexity is a higher cost, both monetarily and in the added mass of propulsion hardware. One could also argue that these systems have a lower reliability due to the fact that there are more moving parts.

A hybrid rocket, shown in Figure 1.3, is a part solid part liquid propulsion system. Typically the fuel is solid and the oxidizer is a fluid. In Sutton's opinion, hybrid rockets have the advantages of: (1) enhanced safety from explosion in fabrication, storage, and operation; (2) start-stop-restart capabilities; (3) relative simplicity which may translate into low overall system cost compared to liquid systems; (4)
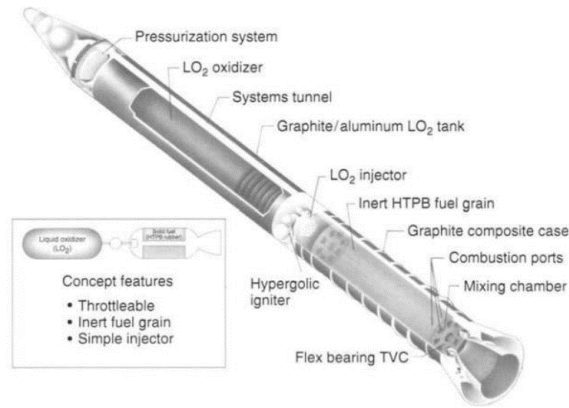
**Figure 1.3**: Traditional Hybrid Rocket [1]

higher specific impulse than solid rocket motors and higher density-specific impulse than liquid bipropellant engines; and (5) the ability to smoothly change thrust over a wide range on demand [1]. These come with the disadvantages of: (1) varying mixture ratio and consequently specific impulse during steady operation; (2) complicated fuel geometries with significant unavoidable residual fuel slivers at the end of burn, which reduces the mass fraction and can vary with random throttling; (3) prone to large-amplitude, low-frequency pressure fluctuations (known as chugging); and (4) relatively complicated internal motor ballistics resulting in difficulty of modeling of regression rates and motor-scaling effects [1].

Hybrids are in essence a compromise of solid and liquid propulsion systems. As such, they have humorously been described by critics as a "bridesmaid" that cannot match the performance of a liquid system nor the packing efficiency of a solid propulsion system [17]. This is arguably the reason hybrid systems have not been seen nearly as much as its counterparts. However, there exists a distinct example in

the propulsion system of the Virgin Galactic Spaceship I and II vehicles [17]. The burn rate of hybrid rocket motor grains is described in a slightly different matter than that of solids [1]:

$$r = aG_o{}^n \qquad (1.2)$$

The relatively low regression rate of hybrid motors is a significant contributor to its "bridesmaid" status as it requires fairly complicated geometries to fulfill mission criteria compared to solids [1]. A major objective in hybrid rocket research has been improving the regression rate of hybrid rocket fuel grains. One method of achieving this objective include imbedding oxidizer particles in the fuel grains, effectively creating a fuel-rich solid motor [2]. Another attempted concept has been multi-port axial oxidizer injection, in theory more evenly distributing the oxidizer within the fuel grain as well as introducing swirl to the flow [18] [19] [20]. Finally, Nagata et al. observed a concept known as a dry towel configuration, in which a collection of fuel fibers were packed into a tube creating random paths for the oxidizer [3]. In this configuration, numerous random small passageways transport the oxidizer from the injector to the burn surface at the end of the grain. Hitt expounded upon this concept by researching the burn rate of porous high-density polyethylene (HDPE) end-burning grains [15].

The advent of additive manufacturing could make hybrid systems more viable by enabling the rapid and inexpensive prototyping and manufacturing of fuel grains. This could enable the development of specialized grains tailored for specific applica-

tions. Some of the typical 3D printed materials applied to hybrid applications have shown increased regression rates compared to traditional HTPB counterparts [21].

## 1.3 Technical Objectives

In reviewing previous burn data for hybrid rocket motors acquired by Hitt [15], it was observed that the difference between the injector and chamber pressure, a first-order estimate of grain pressure drop (pressure drop due to combustion is typically fairly small and neglected), is quite different from the empirical model predictions when referring to x-ray computed tomography (XCT data) for the relevant microstructural parameters, as shown in Figure 1.4. When the porosity is increased to a level typically seen in the center of the grains studied by Hitt, the correlations tend to agree better with the measured data, as shown in Figure 1.5.
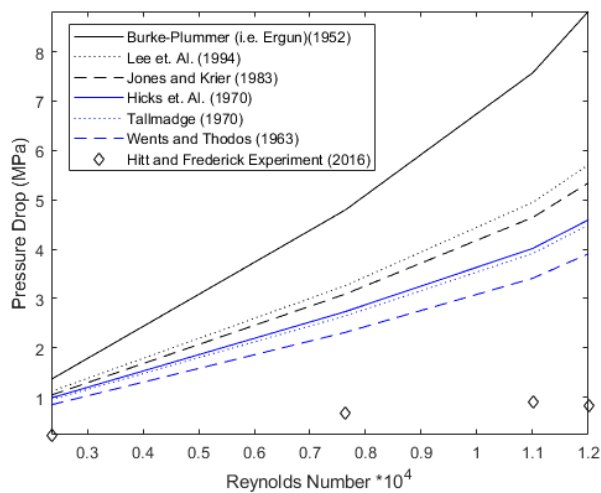


**Figure 1.4**: Hitt Pressure Drop Data [15]
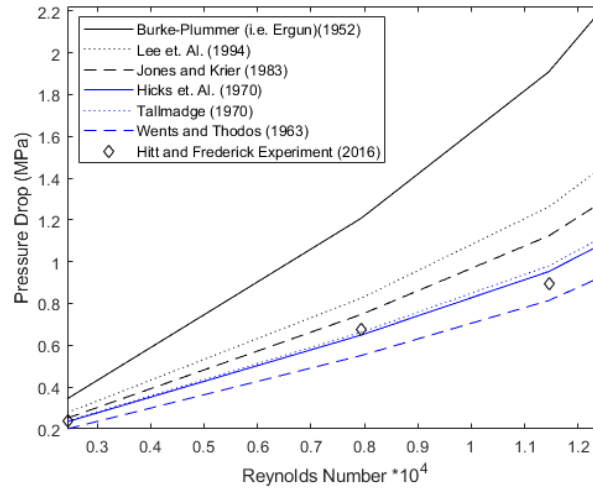
**Figure 1.5**: Hitt Pressure Drop Higher Porosity [15]

This observation results in a question being raised: is the non-homogeneous structure of the grain resulting in the empirical correlation discrepancy? It suggests a theory as well that the flow may have a preference for the more porous region of the grain, resulting in this region becoming more "dominant" of the overall flow. If this is the case, an improved model that can account for these variations in structure and their influence on pressure drop and attendant combustion performance would be very beneficial.

The objective of this research is adapt a heuristic model previously applied to electrochemical research into a mechanical pressure drop scenario. This model is based on the Analytical Transport Network (ATN) theory developed by Cocco et al. [5] [22] [23] [24]. Unlike bulk empirical models, this model will be based on a collection of individual porous paths that form a network ascertained from XCT data. These individual porous paths will be modeled as resistors in a "circuit", in

which the resistances contribute to the pressure drop. The resistances are directly determined by properties that quantify each individual channel's deviation from an idealized straight and smooth flow channel.

The structural data for hybrid motor grains will be acquired primarily through the use of XCT. This data will be validated through scanning electron microscope (SEM), archimedes method tests, and additional external high-resolution x-ray tomography data. This image data is used to observe variations in structural grain properties both axially and radially. Tests using a standard Archimedes method will provide additional verification for porosity measurements.

A series of pressure drop tests for XCT scanned samples are conducted across a wide range of Reynolds numbers. The Reynolds number is controlled through modifying the mass flow by using two different venturi tubes and varying the upstream pressure. The pressure drop behavior measured across the samples are compared to the network model predictions. It is shown that the ATN model provides an accurate estimate for pressure drop behavior in porous hybrid motor grains. This estimate can be achieved in computational times that are orders of magnitudes lower than existing detailed models for flow in porous media, such computational fluid dynamics or Lattice-Boltzmann method. The results presented are among the first experimental validations of a novel modeling approach that may enable the rapid and deterministic design and optimization of hybrid motor grains with complex internal geometry.

# CHAPTER 2

# LITERATURE REVIEW

*My story is a lot like yours, only more in-*
*teresting 'cause it involves robots*

—Futurama

## 2.1 General Overview

A literature review was conducted to define the problem and further examine the physics governing porous media in porous hybrid rocket fuel grains. This review covers an overview of hybrid rocket fundamentals, and also includes many other applications of porous media. It then goes into the genesis of pressure drop correlations of porous media, and process in which most of the structural data for this work was collected: X-ray computed tomography (XCT).

## 2.2 Aerospace Applications of Porous Media

As noted in Chapter 1, porous media have recently seen an increased use in aerospace applications. Specifically, porous have recently seen action in applications such as catalyst beds for monopropellant reactions [12], flashback arrestors for fuel injectors [13], and heat-shield material [14]. Most relevant to the present work, porous media have also received interest in hybrid rocket motor applications [3] [16] [15].

## 2.2.1   Monopropellant Catalyst Beds

Hydrazine and its derivatives have been used as liquid fuels in many aerospace applications, especially in small altitude adjustment scenarios. Hydrazine is hypergolic, meaning it will spontaneously ignite when combined with nitric acid, nitrogen tetroxide, or concentrated hydrogen peroxide. Pure anhydrous hydrazine has been stored in sealed tanks for over 15 years [1].

Although it is a very convenient fuel, hydrazine is also highly toxic. Harmful effects to personnel may result from ingestion, inhalation of vapors, or prolonged contact with skin [1]. This makes it potentially very dangerous, and requires tedious safety measures. This has provided a motivation for an alternative green propellant that is safer while matching the performance of hydrazine-based systems. Baek et al. investigated using a hydrogen peroxide-ethanol premixed monopropellant system in combination with a catalyst bed [12]. The reaction products would be oxygen, water vapor, and carbon dioxide. The catalyst bed consisted of aluminum oxide-based 1/8" samples crushed and polished into 1-1.2 mm sized pellets presumably to increase surface area for reactions. They found that the performance of their test thruster matched and in some cases even surpassed that of the hydrazine alternative. Further optimization of the catalyst bed could improve the performance of this green monopropellant system even further.

### 2.2.2 Flashback Arrestors for Injectors

One of the main challenges in creating a liquid propulsion system is designing an injector that effectively satisfies the requirements of the mission. In the case of a premixed $N_2O/C_2H_4$ green monopropellant alternative to hydrazine, flashback from the rocket combustion chamber into the feed system could be a potential issue. If a hole is small enough in the right conditions, a flame will not travel through it. This is known as quenching the flame. This critical diameter that results in flame quenching can be found as follows [25]:

$$d_q = \frac{Pe_c \alpha_u}{S_L} \tag{2.1}$$

In this equation, $Pe_c$ is the critical Peclet number for quenching, $S_L$ is the laminar flame speed, and $\alpha_u$ is the thermal diffusivity of the unburned mixture. By including a porous flashback arrestor on an injector, Werling et al. were trying to create an injection face with enough combined area to satisfy the flow requirements while quenching the flames from the combustion chamber [13]. They found that the length of the porous flashback arrestor as well as the material affected the conditions that resulted in quenching.

### 2.2.3 Hybrid Motor Grains

Many of the previously alluded to disadvantages of hybrid rocket motors are direct consequences of the relatively low regression rates [1]. In order to mitigate many of the disadvantages of hybrid rocket motors, researchers have attempted to

find ways of increasing the regression rate of the fuels. One approach taken has been

the embedding of solid oxidizer particles in the fuel grain, in effect creating a fuel rich

solid grain augmented with a fluidic oxidizer [2]. Specifically, Frederick et. Al. looked

at modifying a hydroxyl-terminated-polybutadiene grain (HTPB) to include varying

quantities of ammonium perchlorate (AP) and ferric oxide. They found that every

instance of augmentation resulted in an increase of the regression rate. In the case of a

70 percent HTPB, 27.5 percent AP, and 2.5 percent ferric composition the regression

rate increased to 400 percent of the normal pure HTPB composition ( Figure 2.1.
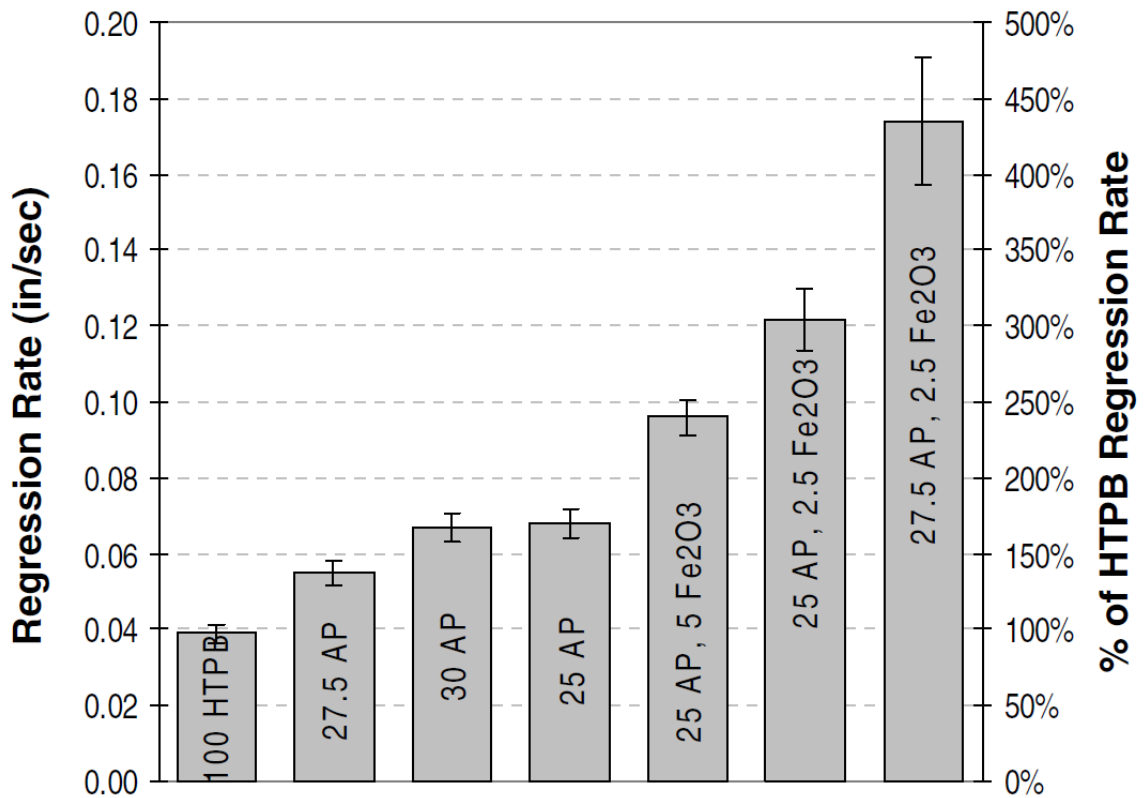


**Figure 2.1**: Mixed Hybrid Results [2]

Another method has been the use of a dry-towel configuration [3] [16]. Unlike

a traditional hybrid, this grain is end-burning, meaning it burns from the aft end

forward ( Figure 2.2). Fuel fibers are placed within a volume, and the oxidizer flows through the gap spaces between the fibers. In theory, these researchers believed that the dry towel hybrid rocket would improve combustion efficiency since the flame is directly behind the propellant surface simulating premixed gasses blowing from the burning surface, and higher thrust resulting from the diffusion flame being closer to the fuel surface [3].
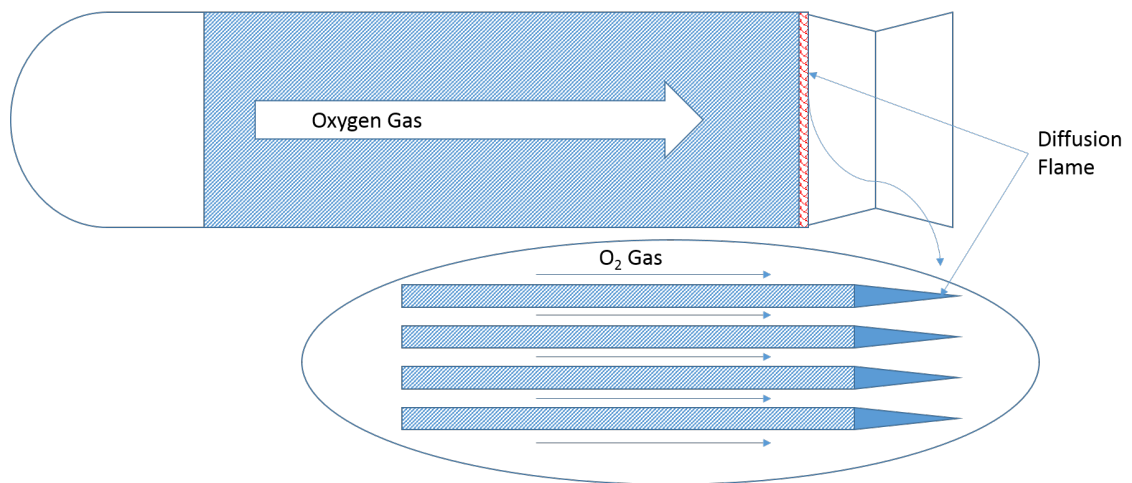


**Figure 2.2**: Dry towel hybrid rocket motor grain concept adapted from Nagata *et al.* [3]

As a sequel to the dry-towel configuration, Hitt [15] examined the concept of porous hybrid motor grains, the focus of this work. Unlike the dry-towel configuration, the fuel structure in this case is one continuous porous body. He developed a burn rate model, and conducted tests using GOX and $N_2O_4$ as oxidizers. A unique finding of this concept is that unlike traditional hybrids, the burn rate is much more dependent on the chamber pressure than the oxidizer mass flux [15]. In this way, it behaves like a solid rocket which is goverened by St. Robert's Law [1].

## 2.3   Porous Media Physics Fundamentals and Transport Modeling

The structure of porous media is very chaotic and hard to predict, but there are ways of making sense of this structure. Like many problems, porous media are often modeled by scenarios that are more structured and easier to understand. One common model for a porous media is simply a tube filled with spheres of a uniform diameter. This breaks the problem into a combination of two common flows in fluid dynamics: flow in a circular cross-section channel of uniform diameter, and flow around a submerged sphere.

In a circular channel, the flow requires a force to maintain velocity or accelerate (denoted by $F_p$) by overcoming the frictional force provided by the medium (denoted by $F_{fs}$). This force is most often the result of a pressure differential from one end of the channel to the other, manifesting itself in the pressure differential from one side of the fluid element to the other (Figure 2.3).

A sphere submerged undergoes many of the same physics as an open channel. The main difference is the fact that this is considered an external flow, while the previous example is internal (Figure 2.4).

This becomes apparent in the terms of characteristic area, A, and characteristic kinetic energy per unit volume, K. Following the approach of Bird, Stewart, and Lightfoot [26], the driving force of the fluid in both models can be described as:

$$F_k = AKf \tag{2.2}$$

Flow Direction

$F_{fs}$

$F_k$

$F_{fs}$

Flow Element Free
Body Diagram (FBD)
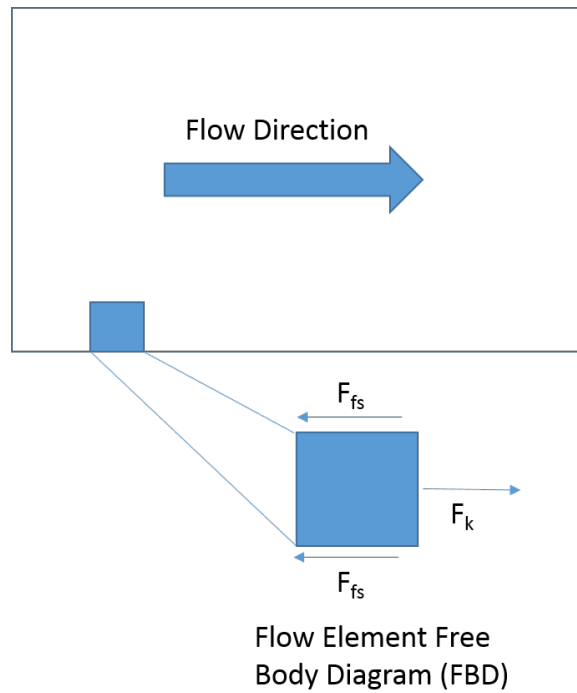
**Figure 2.3**: Open Channel with Fluid Element FBD

$$K = \frac{1}{2}\rho < v >^2 \qquad (2.3)$$

In a conduit flow, the characteristic area (A) is the wetted surface, and K is the dynamic pressure component with superficial velocity, and $f$ is the friction factor. In this case, Equation 2.24 becomes:

$$F_k = (2\pi RL)(0.5\rho < v >^2)f \qquad (2.4)$$

The force term $F_k$ is actually a representation of the net force on the fluid resulting from the pressure difference and the gravitational potential force of elevation difference:
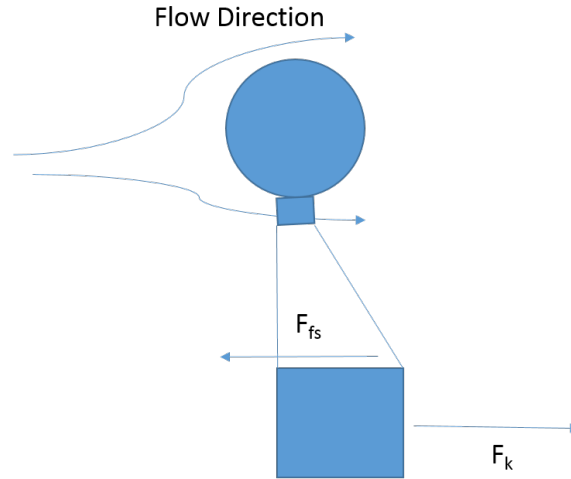
**Figure 2.4**: Submerged Sphere with Fluid Element FBD

$$F_k = ((p_o - p_L) + \rho g(h_o - h_L))\pi R^2 = (P_o - P_L)\pi R^2 \tag{2.5}$$

By combining Equations (2.4) and (2.5) an expression for the friction factor can be defined:

$$f = 0.25\frac{D}{L}\frac{P_o - P_L}{(0.5\rho < v >^2)} \tag{2.6}$$

This equation is often used to calculate the friction factor from experimental data for correlations.

For flow around a sphere falling through a fluid, the equation is analogous to (2.4) with the characteristic length as the surface area of the sphere:

$$F_k = (\pi R^2)f(0.5\rho v_\infty^2) \tag{2.7}$$

The net force term in this equation is the result of the weight of the sphere in the fluid and the buoyant force on the sphere in the fluid:

$$F_k = \frac{4}{3}\pi R^3 \rho_{sph} g - \frac{4}{3}\pi R^3 \rho g \tag{2.8}$$

Equating (2.7) and (2.8) we arrive at this expression for the friction coefficient:

$$f = \frac{4}{3}\frac{gD}{v_\infty{}^2}\left(\frac{\rho_{sph} - \rho}{\rho}\right) \tag{2.9}$$

Equations (2.6) and (2.9) provide accurate estimates of the friction coefficients for two simple flow cases, but in the case of a packed bed with non-uniform geometries, the complexity of the channel geometry makes analysis much more difficult. An approximation can be made by modeling the porous passageways as a bundle of crooked tubes in which the solid particles that make up the tube walls consist of spheres of uniform diameter. As such Equation (2.6) applied to this model becomes:

$$f = 0.25\frac{D_p}{L}\frac{P_o - P_L}{(0.5\rho v_o{}^2)} \tag{2.10}$$

The pressure drop from a single tube "path" within the tube bundle is given as:

$$f_{tube} = \frac{P_o - P_L}{0.5\rho < v >^2 \left(\frac{L}{R_h}\right)} \tag{2.11}$$

In this equation, the term $R_h$ is known as the hydraulic radius. This is the ratio of the total cross sectional area available for flow to the wetted perimeter. It is related to the local Reynolds number via the following equation:

$$Re_h = \frac{4R_h <v> \rho}{\mu} \tag{2.12}$$

Substituting the pressure drop in Equation (2.11) into Equation (2.10) the friction factor for the packed bed can be estimated:

$$f = \frac{D_p f_{tube}}{4\epsilon^2 R_h} \tag{2.13}$$

In which the term $\varepsilon$ denotes the porosity, or ratio of porous volume to total volume. The hydraulic radius ultimately becomes a function of the ratio of porosity to the surface per unit volume of bed $\varepsilon/a$. In turn, the specific surface $a_v$ and mean solid particle diameter are defined:

$$a_v = \frac{a}{1 - \epsilon} \tag{2.14}$$

$$D_p = \frac{6}{a_v} \tag{2.15}$$

Putting together (2.15),(2.14), and the definition of hydraulic radius results in:

$$R_h = \frac{D_p \epsilon}{6(1 - \epsilon)} \tag{2.16}$$

Inserting this into (2.13):

$$f = \frac{3}{2}\frac{1-\epsilon}{\epsilon^3}f_{tube}$$

(2.17)

At this point, $f_{tube}$ is determined empirically through experimental studies and then used to form a correlation.

## 2.4 Modeling of Transport in Porous Media

Perhaps the most famous correlation for laminar flow through a porous medium is a relationship developed by Henry Darcy in designing the water-supply system for the French city of Dijon. This equation is known as Darcy's law [27] which written in terms of pressure loss is as follows:

$$\nabla p = (\rho \dot{m} + v_o)\frac{-\mu}{\kappa A_c}$$

(2.18)

This equation is sufficient for applications involving slow seepage of fluids through porous media, such as a stagnant puddle resting above a soil bed. This equation can be derived from the Navier-Stokes equations. It is important in these applications to ensure that the region of flow is large with respect to the pore size in these applications.

One unique aspect of this research effort is the investigation is occuring in the high Re flow regime. At Reynolds numbers greater than 10, inertial effects become significant and therefore Darcy's Law becomes innefective at modeling. In 1901,

Forchheimer attempted to adapt Darcy's model with the addition of a second order velocity term to account for inertial effects [28]:

$$\nabla p = \frac{\mu v_o}{\alpha} + \frac{\rho v_o{}^2}{\beta} \tag{2.19}$$

This equation is impossible to derive from the Navier-Stokes equations. The terms $\alpha$ ans $\beta$ are referred to as the permeability and non-Darcy coefficient respectively, and were intended to be constants for each material.

In these circumstances, a more commonly used correlation is the Ergun equation [29]:

$$\frac{\Delta p}{L} = (\frac{\dot{m}^2}{A_c{}^2 D_p} \frac{1-\epsilon}{\epsilon^3})(150\frac{1-\epsilon}{D_p Go/\mu} + \frac{7}{4}) \tag{2.20}$$

The derivation of this equation is detailed in Bird, Stewart and Lightfoot and further detailed by Erdim et al. [30] It models flow through a porous bed as flow within a packed bed of perfect spheres. The friction factor f is defined as such:

$$f = \frac{F_k}{AK} \tag{2.21}$$

In which $F_k$ is the total kinetic force of the fluid imparted on the solid material, $A_*$ is the characteristic area, and K is the characteristic kinetic energy per unit volume defined below:

$$A^* = \frac{6(1-\epsilon)A_c L}{d_p} \tag{2.22}$$

$$K = 0.5\rho(\frac{u}{\epsilon})^2 \tag{2.23}$$

$F_k$ is modeled as a force balance on the fluid:

$$F_k = (-\Delta P)A_c\epsilon \tag{2.24}$$

Combining equations (2.21), (2.22), (2.23), and (2.24), another representation of the friction factor results:

$$f = \frac{(-\Delta P)d_p\epsilon^3}{3L\rho u^2(1-\epsilon)} \tag{2.25}$$

Rewritten in terms of the pressure drop per unit length equation (2.25) becomes:

$$\frac{\Delta P}{L} = \frac{-3\rho u^2(1-\epsilon)f}{d_p\epsilon^3} \tag{2.26}$$

Another way to express these correlations is as follows:

$$\frac{\Delta p}{L} = (f_p\frac{\rho u^2}{D_s}) \tag{2.27}$$

In which $f_p$ is representative of a friction factor derived from the correlation. Friction factors from Jones and Krier [31], Tallmadge et al. [32], and Lee et al. [33] are displayed below:

$$f_p = (150 + 3.89(\frac{Re}{(1-\epsilon)})^{0.87})\frac{(1-\epsilon)^2}{\epsilon^3 Re} \tag{2.28}$$

$$f_p = (150 + 4.2(\frac{Re}{(1-\epsilon)})^{5/6})\frac{(1-\epsilon)^2}{\epsilon^3 Re} \tag{2.29}$$

$$f_p = 6.25(\frac{29.32}{Re} + \frac{1.56}{Re^n} + 0.1)\frac{(1-\epsilon)^2}{\epsilon^3}$$

$$n = 0.352 + 0.1\epsilon + 0.275\epsilon^2 \tag{2.30}$$

In many porous media, pressure drops are estimated via empirical correlations. The most well known of these is the Ergun equation [29]. Several other correlations exist as well and are detailed in a review article by Erdim et al [30]. In investigating porous media, the Ergun equation as well as several others tailored for high Reynolds number (Re) flows were applied to the conditions of previously conducted tests, and the predictions of pressure drops were compared to the measured difference of injector and chamber pressures. For the sake of this study, pressure loss from combustion was neglected. The observed experimental results differed substantially from those of the empirical predictions. In the case of the 200 micron grains, the observed pressure drops were far greater than those predicted. In the smaller grain size cases, the pressure drops were far less than what was predicted. There are numerous potential explanations for this discrepancy, but in general this discrepancy points to a major insufficiency of the existing empirical correlations rooted in three key aspects.

First, the existing correlations do not account for the porous media structural effects on the flow in a detailed manner. The only parameters included in the correlations are porosity and characteristic length (i.e. average pore size). The lack of

structural variables within these correlations fail to describe the unique geometry of the specimen at hand. In addition to this, characteristic length is a subject that is very debatable. However, if the empirical correlations were modified to include more structural variables, they would likely be more accurate at predicting experimental results, and apply to a broader range of Reynolds number.

A second major weakness of these correlations is the required underlying assumptions for these to be valid. In many of these cases, the porous geometries are assumed to mimic the behavior of homogeneous packed beds of spheres or tube bundles. This assumption results in the hydraulic diameter becoming a very convenient and steady factor. However in cases in which behavior deviates significantly from homogeneous geometry, this assumption may not be appropriate. Dietrich et al. observed this in their work with ceramic foams [34]. In their studies, Dietrich et al. found deviations as high as 40-50 percent less than those of experimental results in applying a modified Ergun equation.

Finally, the appropriateness of the chosen characteristic length may be brought into question. Ultimately, the hydraulic diameter, or ratio of surface area to volume, is the parameter of interest. In cases outside of predictable well-defined geometries like packed beds of spheres this property may be difficult to estimate. In well-defined morphological cases, this boils down to a convenient factor like the average pore size with a coefficient. However, in more complex cases, these correlations become unreliable in determining accurate results.

The shortcomings of established empirical models in predicting reliable fluidic behavior in porous media is of great concern. The causes of these shortcomings could

be a lack of terms that capture the physics within the media, an oversimplification of some of these complex terms such as hydraulic diameter, and the dependence of coefficients within the correlations to a specific set of physical situations covered by the experimental data set from which said coefficients are derived.

### 2.4.1   Computational Models

Computational models have existed for quite some time in engineering. This category refers to methods of discretizing model geometries into grids and points within a domain, and discreetly solving for properties within this domain by using boundary conditions. Specifically, a domain is discretized into a series of points, and governing equations are used to iteratively solve for a unique solution based on specified boundary conditions. The points within the domain are referred to as nodes, and the domain is broken into individual elements with nodes at the center point. Three common computational models include finite-difference, finite-element, and Lattice-Boltzmann methods.

### 2.4.1.1   Finite Difference

In a finite difference method, the governing partial differential equations derivative terms that describe the physics within a domain are described with a series of finite differences throughout the domain. Arguably, this is the easiest form to use and thus most often implemented. It has seen use in multi-dimensional flow modeling in porous media [35] [36].

### 2.4.1.2   Finite Element

In a finite element method, a complex structure is comprised of small representative elements. Approximate solutions to boundary-value PDEs are then used to capture the physics within the domain. The big advantage to this approach is the ability to calculate properties of interest for each individual element. The major disadvantage is the greater mathematical complexity of the method. It has seen use in transport modeling in porous media [37] [38] [39].

### 2.4.1.3   Lattice-Boltzmann

Lattice-Boltzmann methods (LBM) are a relatively new class of models in the Computational Fluid Dynamics (CFD) world. While the other computational methods function primarily by solving the conservation equations, LBM methods treat the fluids as a collection of random particles performing successive collisions and propagations across a discretized lattice grid. This model accounts for local particulate dynamics that the others do not, and as such has become useful in the realm of porous media simulation [40] [41] [42].

### 2.4.2   Heuristic Models

Heuristic models herein refer to combinations of individual mechanisms or transport pathways with respective property equations combined to form a network. Bulk properties for this network can then be estimated from the individual equations. Heuristic models offer a rapid and sufficient assessment of a problem and are often seen as a compromise between simplified correlations and complex computational

models. One of the areas that these types of models has seen the most use in is that of energy transport within electrochemical systems [10] [43] [4] [5] [44]. Two examples of heuristic models include that of electrochemical fin theory and analytical transport network theory.

### 2.4.2.1  Electrochemical Fin (ECF) Theory

Electrochemical fin theory works by modeling active layer of a composite electrode as a network of particle chains supporting the conduction of ions away from the bulk electrolyte [4] [10] [43] (Figure 2.5). These chains can be comprised of particles with various shapes that together are treated as an extended surface of charge conducting material with surface-level charge transfer reactions, enabling a mechanism to account for variations of cross-sectional area within the electrode. Each element within the network is assumed to follow a general solution of the common ordinary differential equation that describes diffusion through a medium in the presence of a source or sink term.

Networks of electrochemical fins may be constructed with constants of integration determined using standard matrix solution approaches. Nelson et al. demonstrated that the ECF method could assess behavior of real solid oxide fuel cell microstructures with significantly reduced computational cost, as measured by both computational time and memory required [43]. This reduced cost results from the fact that the computational cost of network-based heuristic models scales with network complexity as opposed to the volume of the structure. While demonstrated for solid oxide fuel cells these methods have been applied to other electrochemical de-
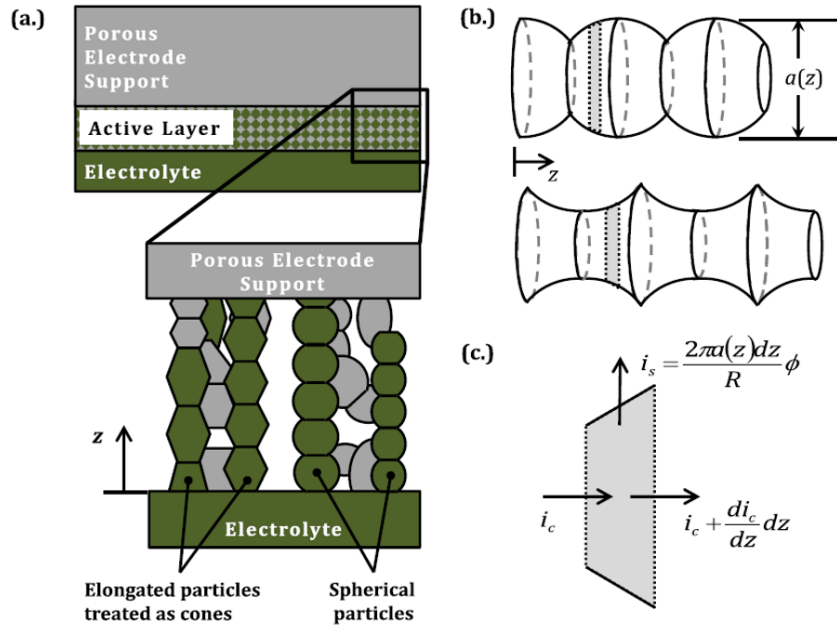
**Figure 2.5**: Electrochemical Fin Concept [4]

vices [45] [46] and may apply elsewhere. Examples of such cases include heat transfer from extended surfaces (fins) and porous structures [47] as well as the diffusion of a gas through a catalyst bed [26].

### 2.4.2.2   Analytical Transport Network Theory

The analytical transport network theory (ATN) approach was developed as an extension and generalization of the electrochemical fin method to other heterogeneous media (Figure 2.6). This approach models the diffusive potential flow through a 3-D network by combining graph theory, linear algebra, and geometry into a depiction that relates a microstructural network's morphology comprised of individual channels to an overall bulk transport coefficient [5] [22] [23] [24]. The porous pathways within a geometry are divided into individual pathways described by individual nodes and

vertices (Figure 2.7). Each pathway has an individual resistance ratio, and this ratio is used to go from a baseline case to the actual model scenario.
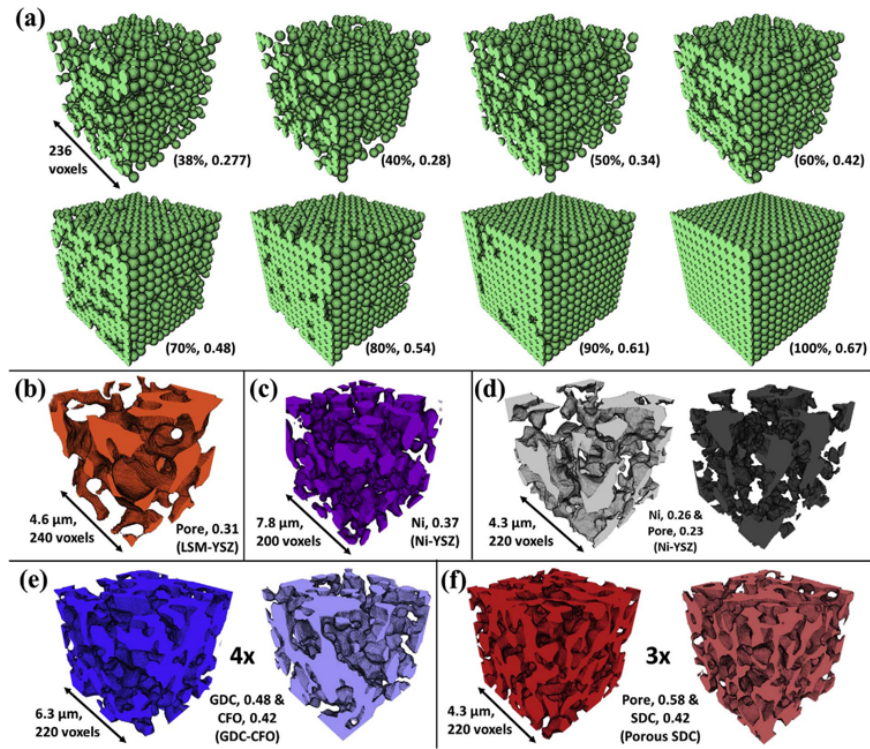


**Figure 2.6**: Analytical Transport Network Concept [5]
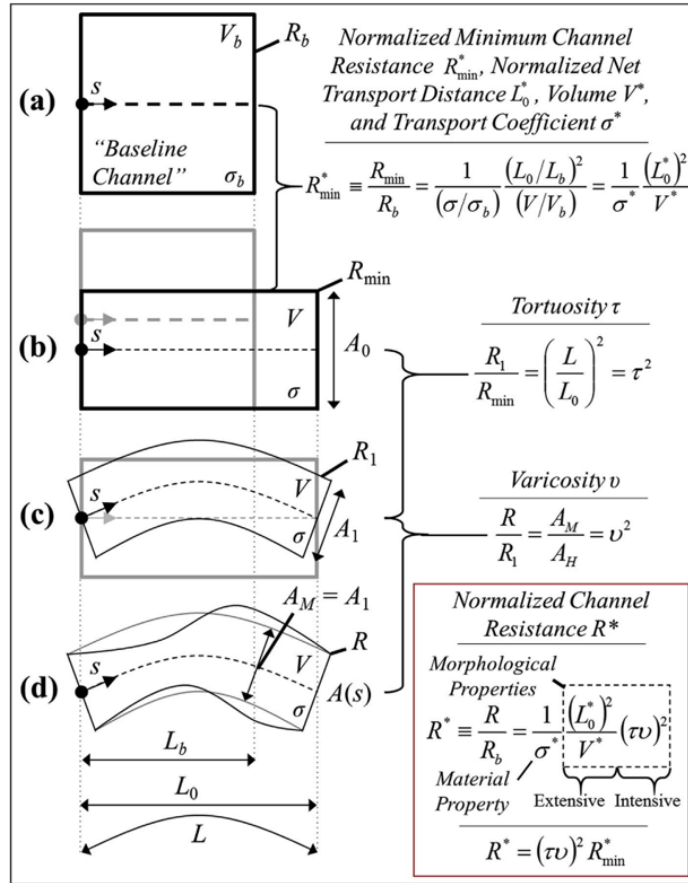
**Figure 2.7**: ATN channel Description [5]

Once resistance ratios for indidual channels within a network have been found, the channels are assembled into a network of nodes and edges modeling the potential transport passageways. Once again a "baseline" network case is defined, often an empty channel the size of the entire medium. An overall network resistance ratio is computed from the individual channel resistances, and this ratio is used to estimate transport property changes (Figure 2.8). Further details are included in the methodology chapter of this document.
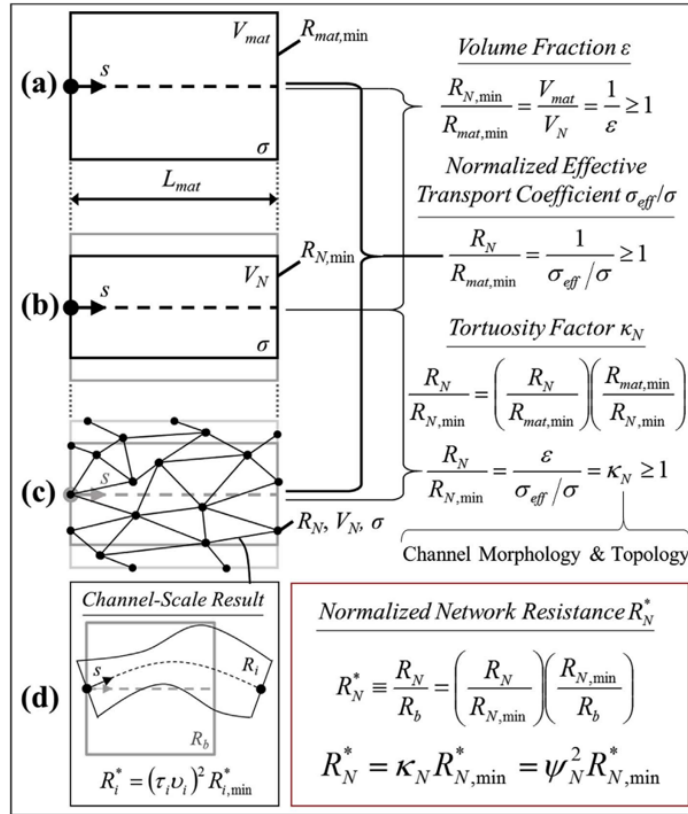
**Figure 2.8**: ATN network Description [5]

## 2.5 Porous Media Characterization Methods

In order for any of the previously described models to work, they must have solid foundational data for the porous structure to be implemented. This data may be acquired through several characterization methods. The traits of the porous medium that are sought include porosity ($\epsilon$), average pore size, connectivity of the pore domains, and tortuosity, a measure of actual transport path length relative to apparent transport path length. In chemically reactive systems such as catalyst beds or electrochemical systems interfacial surface areas may also be estimated.

### 2.5.1 Density/Archimedes Method

One of the most common methods for determining the overall density and porosity of a porous medium is known as the Archimedes Method. This approach involves using mass measurements before and after liquid intrusion to determine volumetric properties. There are several ways to apply these principles, take for example the ASTM Standard C20-00, a way to determine porosity for burned refractory brick (illustrated in Figure 2.9) [48].
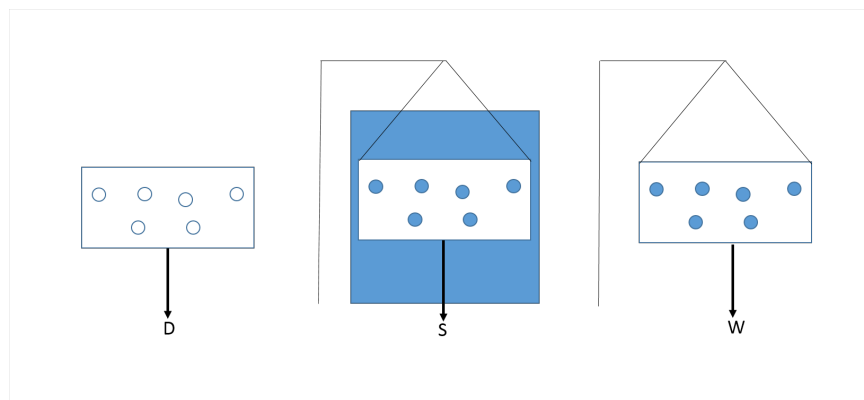


**Figure 2.9**: Archimedes test characterization. The dry Weight (D) (left), suspended weight (S) (center), and saturated weight (W) (right) are all used to determine relevant porous properties

In this test, the sample is often heated for a period beforehand to ensure that any residual fluid is removed via evaporation. The sample is then weighed after ensuring that it is dry. Next, the sample is boiled in water for 2 hours, and then allowed to cool to room temperature for 12 hours. At this point, further weighing is done.

The sample is weighed while suspended in water in order to yield a suspended weight. The specimen is then removed from the liquid medium, and residual drops on the external surface are removed via a cloth. At this point the saturated weight is taken. In all of these tests it is assumed that the density of water is $1g/cm^3$.

The Archimedes method is simple, convenient, and often non-destructive. Examples have been the determination of porosity in catalyst structures [49] and additively manufactured metallic components along with x-ray methods [50]. It requires many steps to ensure that accurate data is taken such as boiling the liquid or sonicating to remove entrained gases within the specimens, ensuring the specimens are saturated for an appropriate length of time, and calibrating instrumentation to accurately measure the specimen in the various states of suspension within and outside the liquid. In addition to this, another disadvantage is the fact that densities of the materials are vital parameters to know beforehand in order to calculate the volume. In situations that the density is difficult to determine such as certain additive manufacturing products, potential errors could be present. Human error can also play a significant role in Archimedes method measurements. Finally, Archimedes method is unable to account for pore spaces that are non-uniform or not connected to the surface of the sample.

### 2.5.2 Porosimetry and Pressure Driven Methods

Porosimetry and pressure driven methods work by calculating key porous characteristics by using pressurized fluid to intrude the porous network, and based on the fluid surface tension, membrane-surface contact angle, and required driving pressure,

calculating properties of interest. These methods are relatively easy to execute in the absence of imaging equipment, but they have several disadvantages. First, it may be difficult to remove the penetrating fluid from the sample after testing. This could result in sample alteration. Second, the factor that contributes to the required driving pressure most is the minimum diameter within a pore passageway. Thus, these methods often measure the "throats", and not the average diameters of the pores. This phenomena is referred to as the "ink bottle effect" [51].

### 2.5.2.1  Brunauer Emmet Teller (BET) Method

Another method for determining porosity, average pore size, and internal surface area is Brunauer Emmet Teller (BET) analysis [6] (Figure 2.10). This approach is based on gas adsorption, or the depositing of layers of molecules on solid materials that occurs at temperatures near condensation points, or isotherms. BET is an adaption of the Langmuir model [52] [53] [54] for adsorption in a monolayer for application to multilayer adsorption.

By adjusting the pressure of the adsorbing gas, one can determine whether a single layer, multiple layers, or a large scale condensation of gas deposit onto the porous media surface. The total mass of deposited agent in a single layer can give an estimate of internal surface area, and the mass at full saturation of pores in condensation can be used to determine average pore size, volume, and distribution. This method works well for most of the standard pore sizes, however at the micropore and smaller level researchers have found issues as the monolayer adsorbtion occurs at pressures well below the defined BET isotherm limits [55] [56].
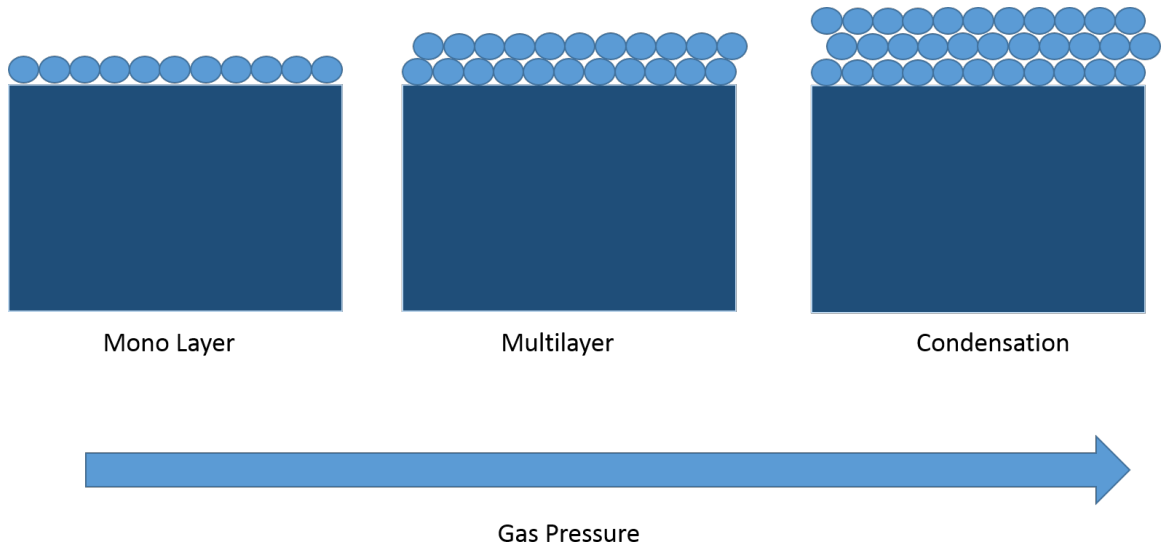
**Figure 2.10**: BET Concept [6]

## 2.5.2.2   Mercury Intrusion Porosimetry

In mercury intrusion porosimetry (MIP) a non-wetting fluid, mercury, is driven into the porous medium by adjusting pressure of the fluid (Figure 2.11). As pressure increases, pore penetration increases until a plateau is reached, at which point the porous space is completely saturated [57]. Using the Washburn equation (Equation 2.31) [58], pore diameters at varying pressures can be calculated, ultimately yielding a total pore volume, porosity, and pore size distribution.

$$D_{pore} = \frac{4\gamma_L cos\theta}{P_{Hg}} \qquad (2.31)$$

Mercury intrusion porosimetry has the advantage over the Archimedes method in that MIP can provide an estimate of pore size distribution in addition to an overall porosity. One major disadvantage is the fact that it cannot account for pores that are
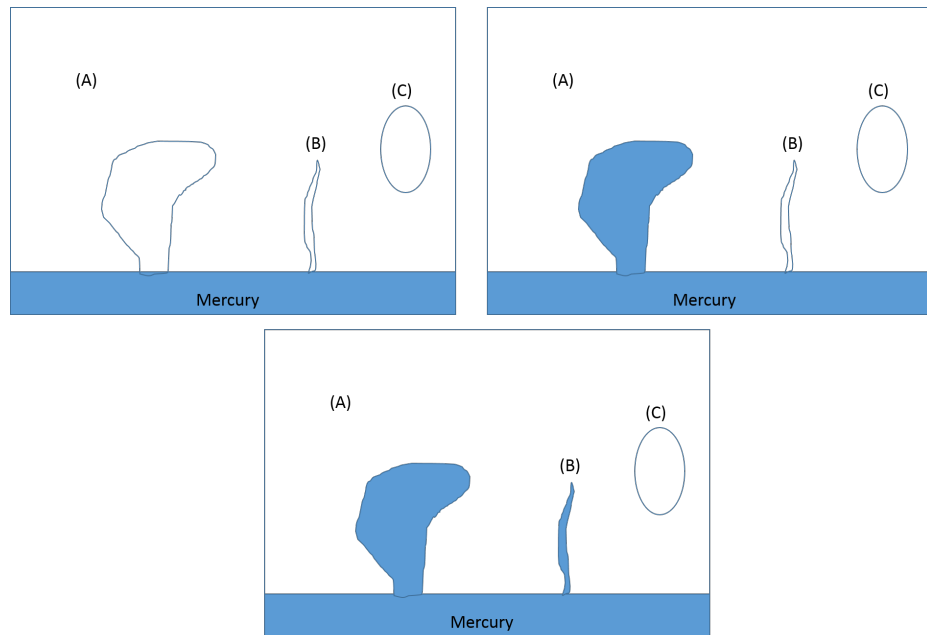
**Figure 2.11**: Mercury pore intrusion method. Differential Mercury pressure is gradually increased until large pores (A) and ultimately smaller pores (B) are saturated with liquid [57].Internal pores (C) are not accounted as no path of intrusion exists.

not connected to the surface through the network. In addition to this shortcoming, safety issues must be taken into consideration in order to limit human exposure to mercury. Finally, MIP is notorious for being susceptible to the "ink bottle effect" previously mentioned [51].

### 2.5.2.3   Bubble Point Test

Another common method for estimating pore size is the bubble point test [59] (Figure 2.12). A bubble point test involves a liquid saturated porous specimen attached to a pressurized gas supply on one end, and a liquid reservoir on the other end. The liquid within the pore space and the medium is the same. The pressure of the gas is adjusted until bubbles are observed in the liquid reservoir. The onset of

bubbles is referred to as the bubble point. At this point, the Young-Laplace equation can be used to calculate the maximum pore radius $r_{p,max}$ as a function of the bubble point pressure $\Delta p_{bubble}$, surface tension of the liquid $\gamma_L (Nm^{-1})$, and contact angle between the liquid and membrane surface $\theta(^0)(2.32)$.
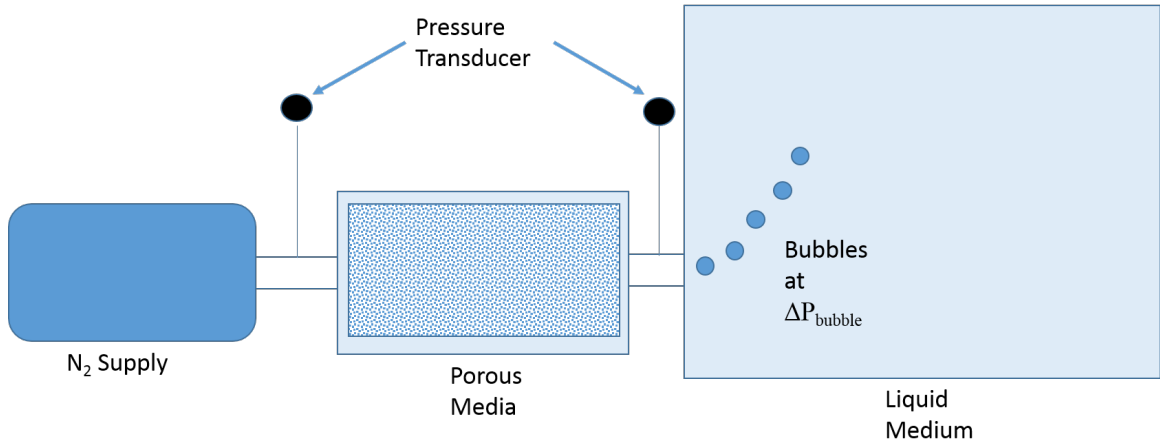


**Figure 2.12**: Bubble Point Test Setup

$$\Delta P_{bubble} = \frac{2\gamma_L cos\theta}{r_{p,max}} \qquad (2.32)$$

The main weaknesses behind this method are similar to those of mercury intrusion, most notably the "ink bottle effect". However, depending on the gas used for the test sample alteration or destruction may be avoided.

### 2.5.3 Imaging Techniques

The previous techniques involved indirectly measuring properties of interest through saturation of a porous medium with fluids and determining observable changes that are mathematically related to the properties of interest. In addition

to specific limitations noted above, these methods all provide property estimates for bulk samples and do not offer a means of finding localized property data. Imaging techniques offer an advantage over bulk property measurements because imaging methods can be used to directly measure the microstructural properties of interest and examine individual areas of interest.

### 2.5.3.1  Optical and Electron Microscopy

Microscopy is a method for directly determining pore geometries via direct visual observation. Depending on the resolution required, observation is done via optical microscope or electron microscope. Optical microscope is useful for larger features, while smaller features are usually analyzed via electron microscope.

Scanning electron microscopes (SEM) (Figure 2.13) have been used to observe rocket propellant structures in various applications, including ammonium perchlorate deflagration and the effect of medal additives on propellant combustion [60] [61]. SEM has additionally been used to study crack propogation in fatigued solid propellants Both work by exploiting the interactive properties of electrons. Generally speaking, electron microscopy can achieve magnifications significantly greater than that of optical counter parts (1-2 million times), and also achieve resolutions down to the subnanometric scale [7]. There exist two primary techniques for electron microscopy: transmission electron microscopy (TEM) and scanning electron microscopy (SEM).

In a TEM procedure, an electron gun projects a beam of electrons through an ultrathin sample, interacting with the sample during passage. The beam image is then magnified and focused onto an imaging device (film or CCD camera). The
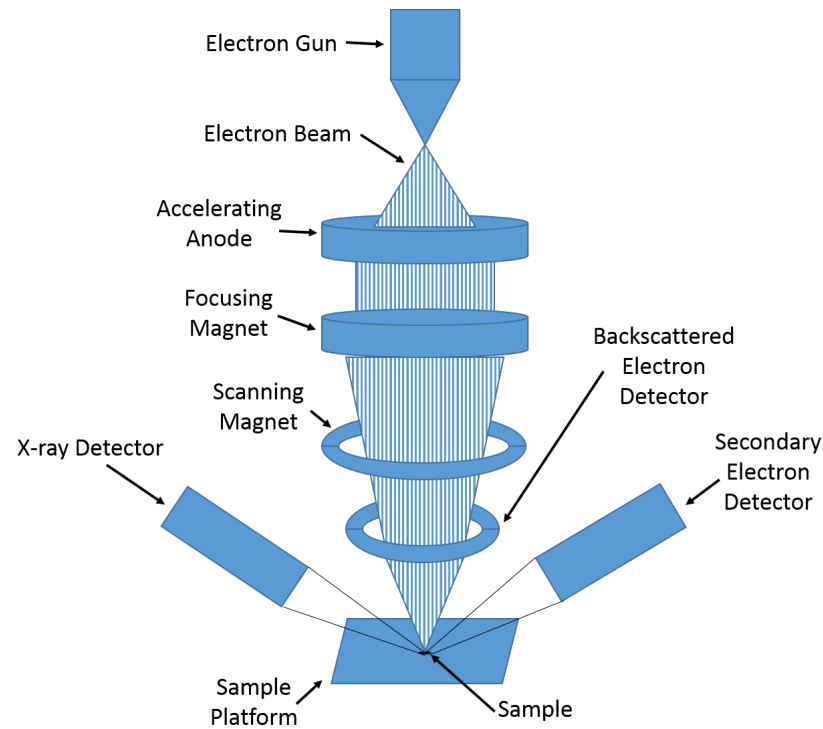
**Figure 2.13**: Typical SEM Setup [7]

specimen must be imaged under vacuum conditions and must be extremely thin (100-200 nm) [7]. This size limitation is the main drawback to TEM imaging. Transmission data provides some whole sample insight, but with such small size limitations this significantly constricts the useful area of study of these samples.

Scanning electron microscopy [62] works by exploiting the atomic interactions within materials with free electrons projected in the form of a beam. In an SEM process, a collection of electrons are accelerated to a high energy and focused onto a specimen via the use of electromagnetic fields. The manner in which the specimen reacts to the electron beam is indicative of material properties of instance. Most commonly, the electrons react with the material atoms through elastic and inelastic interactions. In the case of an inelastic interaction, an electron of lower energy is

ejected from the outer shell of the sample atom. This electron is known as a secondary electron (SE). In an elastic interaction, the electron changes trajectory and escapes the sample. This is known as a backscattered electron (BSE). Image construction in an SEM system involves using detectors to map the intensity of SE and/or BSE signals onto a detector screen, which then translates these intensities to grayscale values for pixels in an image.

In addition to the advantages of optical microscopy methods, the SEM has the desired attributes of high magnification and field of view depth when compared with the traditional microscope. This allows for a depth within the SEM images that is very atypical of other 2D methods. The SEM is reported to have a depth of field 300 times greater than that of a light microscope, and can even achieve sub-nanometer resolutions at low beam energies (1 kV) [62]. However, it is important to note that although SEM images can provide depth to the images, it is still ultimately a 2D imaging method. In most cases if one wants to acquire data of the whole sample structure, a 3D imaging method, for example a tomography-based method, is needed. In addition, SEM requires very tedious sample preparation for materials with volatile high vapor-pressure components.

### 2.5.3.2  X-ray Imaging

X-ray imaging is arguably the most prominent non-destructive method for acquiring image-based morphological data. It involves exploiting the concept of material absorption characteristics of x-ray radiation. This absorption is mathematically described by Beer's Law:

$$\frac{I}{I_0} = e^{-\mu\rho t_{mat}} \tag{2.33}$$

In a typical x-ray imaging system, an x-ray source emits x-rays through the object of interest. An x-ray detector on the opposite end captures the image projection and translates it into a grayscale image (Figure 2.14). This image is then post-processed for data analysis.
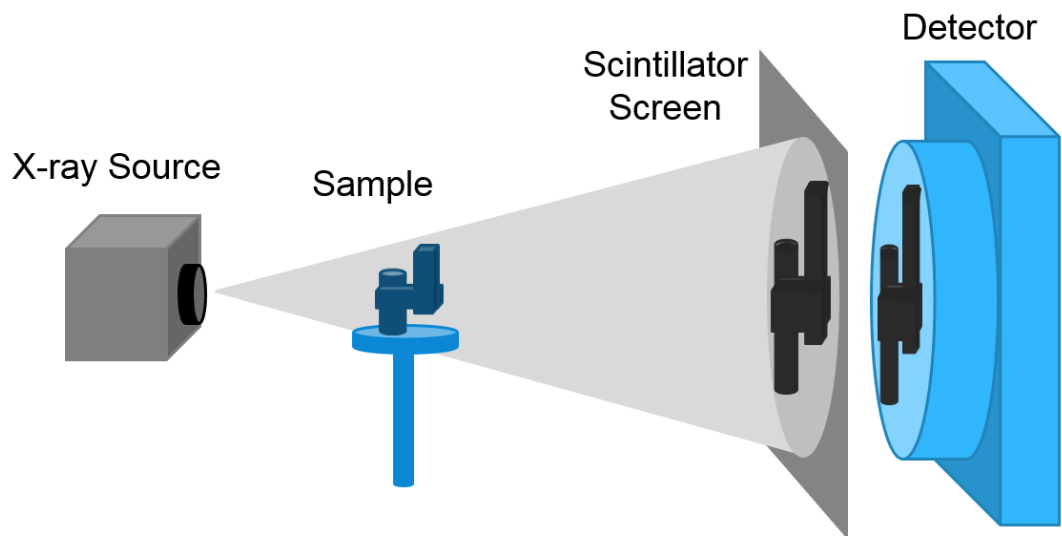


**Figure 2.14**: Typical x-ray imaging set-up [8]

X-ray imaging is accomplished via two primary methods: 2D radiography, and 3D x-ray computed tomography (XCT).

Radiography is often used to capture real-time dynamic events such as the burn rate and change of a solid rocket motor grain structure during motor combustion [63], the rapid discharge of an energy cell [64], and liquid spray processes [65] (i.e. liquid

rocket motor injectors [66]). Often this process involves the rapid capture of static images at a high time resolution. Once the event has been captured, the stack of images at each time stamp are assembled and post-processing steps such as grayscale thresholding are used to extract relevant data.

Unlike a real-time radiography, computed tomography is often used to observe specimens in a static environment, although with proper equipment real-time XCT data can be conducted [67]. It is commonly used to observe static properties, such as the structure of battery electrodes [68], fuel cells [69], and rocket propellants [70] [15] [9]. The trade-off in sacrificing real-time imaging is the ability to collect 3-D data. In a computed tomography, a set of x-ray transmission images are used to reconstruct cross-sectional slices of a specimen. The word tomography traces its roots back to tomos, the Greek word for "cut". In an x-ray computed tomography (XCT) process, a series of transmission images are taken of a sample in rotational increments until a full rotation has been completed. This is done in 360 degrees in the case of all XCT systems except for parallel beam systems, which only require 180 degrees of rotation. This set of images in then processed through an inverse radon transform in order to yield a set of cross-sectional slices of the specimen. Specifically, to reconstruct the interior of a sample two of the most common techniques are filtered back projection (FBP) and algebraic reconstruction technique (ART).

XCT can yield numerous properties of interest. Unlike 2D methods such as SEM, optical microscope, and radiography, XCT can yield 3D data providing valuable morphological data on all spatial dimensions. In the medical field, it provides non-destructive image data of bone structures, and can detect fractures and other

deformities. In the world of porous media characterization, it can provide porosity, average pore size, average solid particle size, and pore network connectivity. Sample preparation is very minimal, although some care may need to be taken if the x-ray energy absorbed is high enough to cause material deformity/destruction. The main disadvantage is the required safety measures to use the system without harm. X-ray energy can cause sample damage in some cases as well. Sample alignment can also be an issue, as slight tilt on the rotation axis can result in "stacked projections" resulting in noticeable blurs in the reconstruction image set.

### 2.5.3.3   Neutron Imaging

Neutron imaging is a non-destructive technique for observing the interior of many materials, enabling the generation of both 2-D and 3-D data [71]. It has been used in several aerospace propulsion applications, especially in hydrazine and monopropellant research [72] [73] [74]. In addition to this, it has seen use in imaging electrochemical cells [75]. It is analogous to x-ray imaging, except that the transmitting energy is a neutron beam. The great advantage this has over x-ray imaging is that neutron attenuation is dependent on nuclear atomic properties rather than material density, allowing it to image materials that would be difficult for x-rays. Hydrogen is the most prominent exception [76]. This makes it ideal for imaging internal structures of materials that would otherwise attenuate x-rays. Like x-rays, it can be used for radiography (2D) and tomography (3D).

### 2.5.3.4  Magnetic Resonance Imaging (MRI)

Magnetic resonance imaging (MRI) is another tomographic imaging technique that provides excellent non-destructive data. It is most commonly known for its use in the medical field as a noninvasive diagnostic tool. It has seen use in observing flows in catalyst beds [77] [78]. Within material characterization, it is used to image large and small diameter objects. When imaging objects <1 cm in diameter, it is referred to as nuclear magnetic resonance (NMR) imaging, otherwise it is magnetic resonance imaging [62]. It has similar applications to x-ray and ultrasound imaging techniques, with the added benefit of the magnetic sensitivity aspect enabling the observation fundamental properties within matter. Among the properties that MRI can observe are distances, diffusion coefficients, concentration, microscopic viscosity, partial pressure, and dielectric constants [62].

# CHAPTER 3

# METHODOLOGY

> *Yes, of course duct tape works in a near-vacuum. Duct tape works anywhere. Duct tape is magic and should be worshipped.*
>
> —Mark Watney- The Martian

## 3.1  Experimental Methods

In order to accomplish the goal of this endeavour, three pieces of data were required: 3D XCT data of the porous hybrid samples with which to generate an ATN network model from, additional morphological data to validate the XCT data, and experimental pressure drop data for comparison to ATN model predictions. All tests were conducted on the UAH campus. The XCT data was acquired at the PRC High Pressure Laboratory, the additional data was acquired at the Shelby Center Lab, Tech Hall, and various other locations. The pressure drop tests were conducted at the PRC Johnson Research Center (JRC) Spray Facility.

### 3.1.1  Sample Description

The porous hybrid samples were acquired from the same materials used in previous studies [15]. These materials consisted of large rods of porous material

created from extrusion processes. Nominal pore sizes (NPS) were determined by the manufacturer (Pore Technology, Marietta, TX) via bubble point tests for two sample sets, one with an NPS of 200 microns (Figure 3.1), and another with an NPS of 100 microns (Figure 3.2). The samples were cut to a length of 20 mm using a horizontal band saw. These samples were attached to nylon sleeves with JB Weld epoxy.
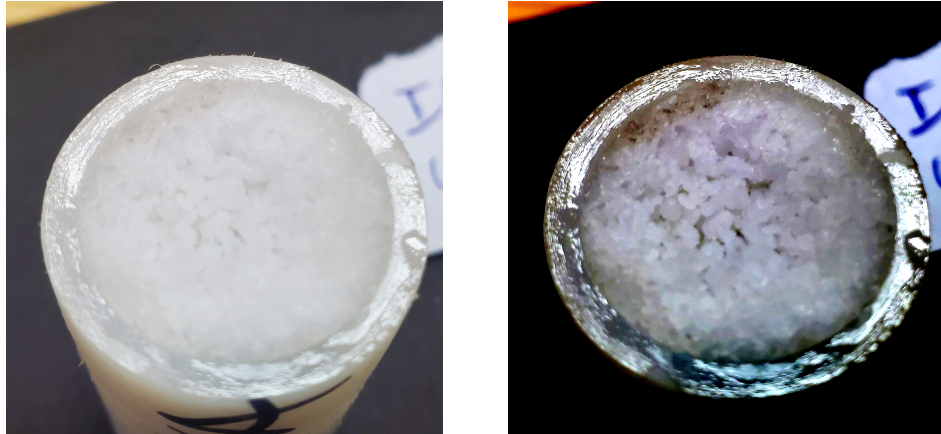


**Figure 3.1**: 200 micron NPS Specimen Original (left) and Enhanced Contrast to Emphasize Pore Visibility (right) Images



**Figure 3.2**: 100 micron NPS Specimen Original (left) and Enhanced Contrast to Emphasize Pore Visibility (right) Images

### 3.1.2    Microstructural Characterization

The main parameters determined from the microstructural characterization were porosity, average pore size, and average solid particle diameter from x-ray data. To validate the x-ray data, these results were compared with those of experimental archimedes method tests, image data acquired from scanning electron microscope (SEM), and external hi-resolution x-ray data from ZEISS.

### 3.1.2.1    Archimedes Method

Archimedes tests were conducted for each of the porous hybrid samples in order to verify porosity data from the XCT images.  These tests were conducted according to ASTM Standard C20-00 with minor deviations. The Archimedes method measurements were performed using an Adams Equipment PW254 analytical balance with ethanol as the working fluid. Sonication was performed using a Branson 2800 sonicator in a water bath.  The dry mass of each sample was measured first.  The porous hybrid samples were held in centrifuge tubes within ethanol during sonication. After sonication, the centrifuge tubes were removed from the water bath, and the samples were left within the ethanol-filled tubes for 48 to 72 hours.  At this point the samples were removed from the tube, and weighed suspended within ethanol contained by a beaker.  Finally, the samples were weighed suspended in air with ethanol-saturated pores.

### 3.1.2.2   X-ray Imaging

The UAH XCT System is located in the PRC High Pressure Laboratory in the Materials Science building on the UAH campus. The system hardware consists of an x-ray source, motorized stages, x-ray detector, and image processing computer (Figure 3.3). The x-ray source is a General Electric 200MF4 with a tungsten filament that has an operating tube voltage range from 0-200 kV, and an operating current range from 0.5-10 mA. The source emits a conical x-ray beamwith a focal spot size of 1 mm. Typical operating conditions for the specimens imaged in this work were source voltage of 45 kV, source current of 3 mA, and a detector exposure time of 30 ms. The motorized stages consist of 3 translational stages with one rotational stage mounted atop the 3 translational stages. The translational stages are Velmex Bi-slides capable of traversing 5 in. in either direction with a movement of 0.00025 in./step and minimum step size of 1.
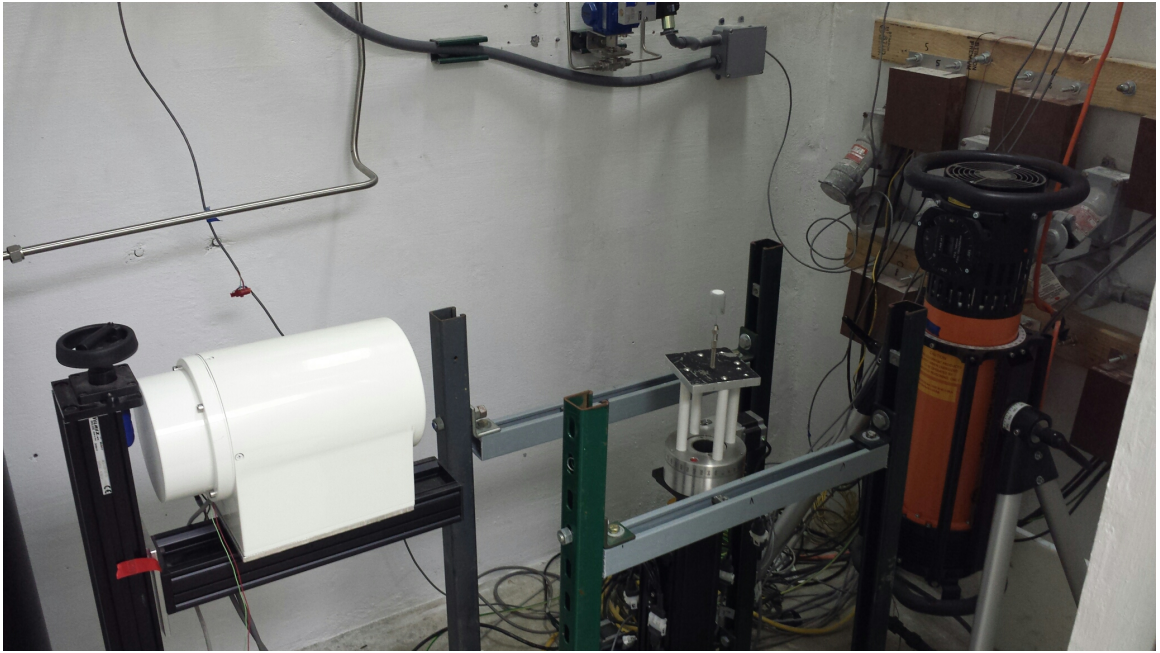
**Figure 3.3**: HPL XCT Setup

The Z-axis mounted rotational stage is powered by a Vextra type 23T2 double shaft stepper motor, the same as the rotational stage. The x-ray detector is assembled by North American Imaging, and consistes of a Toshiba E5877J-P1K image intensifier optically coupled via a C-mount to a Kappa HiRes3-XR camera. The camera was run in high-resolution mode in order to accurately resolve as many pores as possible. Unfortunately in this manner the most extreme upper and lower portions of the imaged grains extended outside the x-ray field of view in some instances. Image analysis of these image stacks have suggested that property variation is very minimal in the axial direction, therefore the properties estimated from the x-ray data can justifiably be assumed to represent the properties of the excluded regions as well.

The software used to operate the camera and acquire images consisted of an in house LabView code that controlled a C++ code developed to interface with the camera in a manner that allowed for an automated CT acquisition. Each image was the result of 16 images at the same angular location averaged together to reduce random noise within the images. Images were acquired in quarter-degree increments. Open beam (images without a specimen in the field of view) and dark field (images without the x-ray source operating) images were collected and used to normalize the CT transmission images as well.

The high resolution XCT data was acquired at ZEISS facilites using a ZEISS Versa 520 X-ray microscope. The resolution of the images acquired and reconstructed is approximately 18.4 microns [9].

### 3.1.2.3   SEM Imaging

The SEM measurements were performed using a Hitachi TM-100 Tabletop SEM Microscope available in the UAH Civil Engineering Department. Images were taken at magnifications of 40X, 50X, and 80X [9]. Average pore size from SEM data was determined in two ways. First, 10 lines were randomly drawn in each image between solid material points to represent pores. They were calibrated based on the provided length scale, and the average line length represented the average pore size (Figure 3.4). The SEM images were also thresholded, and the previously mentioned PSD algorithm was applied to the 2-D image.
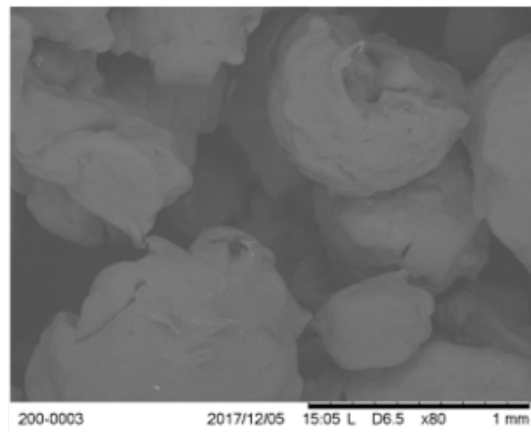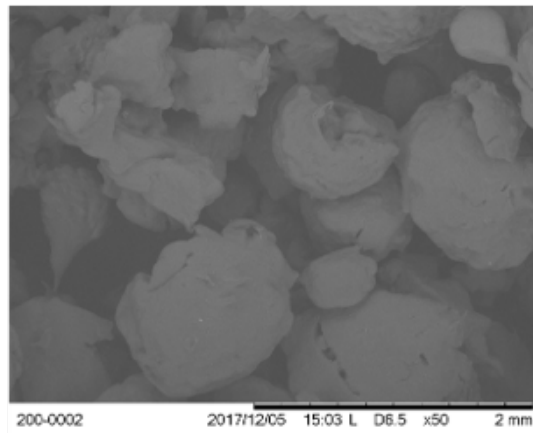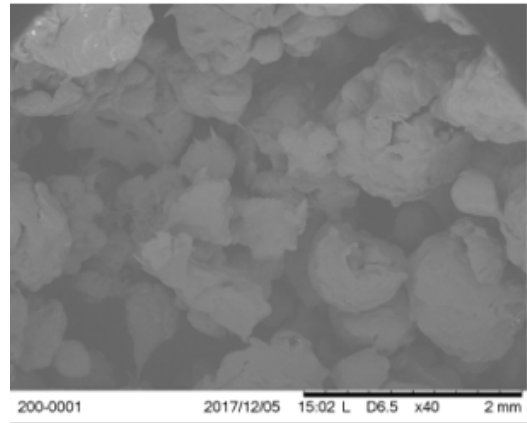
**Figure 3.4**: SEM 40X (Top), 50X (Middle), and 80X Mag (Bottom) of 200 micron NPS Grain

### 3.1.3 Pressure Drop Measurements

The overall goal of this part of the research endeavor is to experimentally examine the relationship of Reynolds number to pressure drop in the examined porous hybrid grains. Reynold's number is defined by the relationship Porous Media Reynolds number:

$$Re = \frac{\rho u D_p}{\mu (1 - \epsilon)} \tag{3.1}$$

Or in terms of the mass flux:

$$Re = \frac{G D_p}{\mu (1 - \epsilon)} \tag{3.2}$$

This implies that Reynolds number is controlled by the mass flux, as all other parameters in the equation are constant. Within this experiment, mass flow is best adjusted through modifying the supply line pressure. Therefore the Reynolds number is varied by the mass flow, making it imperative that the mass flow is a known quantity.

$$\dot{m} = \rho u A \tag{3.3}$$

This is achieved in a manner that is common in many rocket applications. By ensuring that the flow is choked, variations in downstream pressure do not affect the mass flow rate upstream of the choke point. In order to ensure choked flow, the downstream to upstream pressure must be in a range of 0.54-0.57 [1]. This implies that the area ratio of the choke point to smallest area in another location should be

approximately the same value.

$$\frac{A^*}{A_{crit}} < 0.54 \tag{3.4}$$

Another critical area for choked flow is the total flow area of the porous grain. This area is determined by the total area multiplied by the porosity:

$$A_{crit} = \epsilon A_{grain} \tag{3.5}$$

By current calculations, for a 0.18" venturi, this area ratio is 0.17. It is important to note that in previous combustion tests at the hot fire test stand, there were tests in which unchoked flow was encountered. One possible cause is the melting of grain material obstructing porous passages, thus lowering the effective flow area causing a critical area ratio to be greater than required for choked flow.

The Propulsion Research Center Spray Facility was selected as the test site for this reason (Figure 3.5). In the HPL, the supply line external diameter is 1/4". The internal diameter would be very close to the internal diameter of the desired venturi for use of 0.18". Therefore in order to achieve the desired mass flow rates while still choking at the point of measurement, a smaller venturi would be needed and a higher pressure would be required. The Spray Facility supply lines are 0.5", and the maximum supply pressure is 2200 psi. The 0.5" line allows the use of larger venturi tubes to achieve the desired mass flow rates at lower pressures.
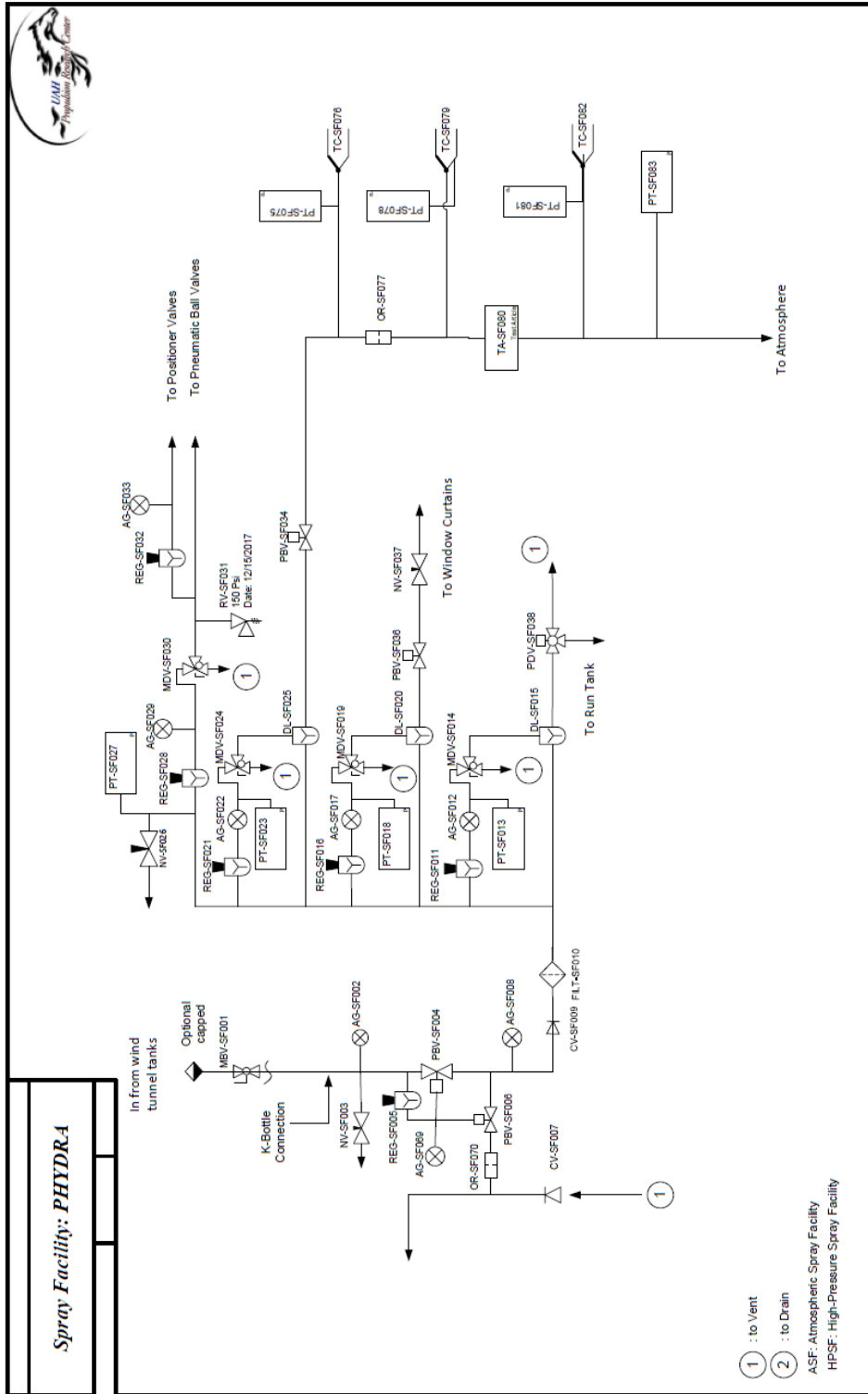
**Figure 3.5**: Johnson Research Center Spray Facility Diagram

Pressure and Temperature Data were taken directly upstream of the first flange, marking the injector/inlet conditions. The apparatus exits to atmosphere, therefore the exit pressure should remain as atmospheric in theory. To verify this, pressure and temperature are also taken in the pipe section aft of the grain. Omega type K thermocouples were used, and Honeywell 060-E067-12 pressure transducers were used with an uncertainty of +/- 3 psig for the venturi and upstream transducers, and +/- 1 psig for the downstream and exit measurements.

The porous hybrid grains have external nylon sleeves attached via epoxy, resulting in a total diameter of about 1". This was housed in an apparatus consisting of two pipes welded to two flanges, shown in the photograph in Figure 3.6 and the sketch in Figure 3.7. A detailed drawing is provided in Appendix B.
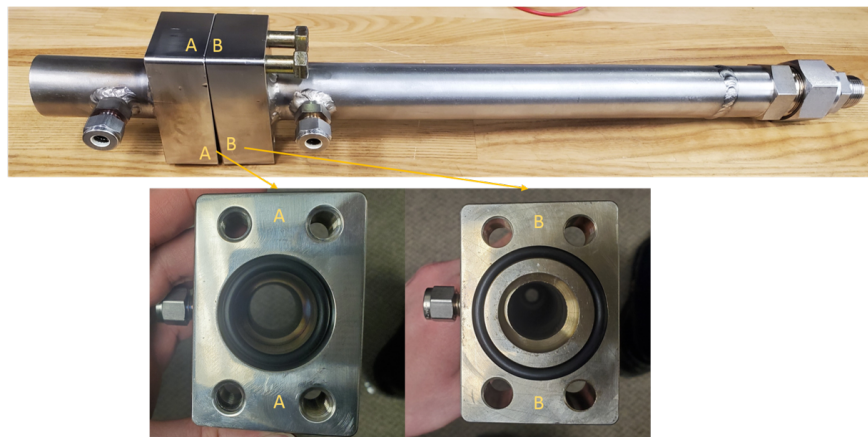


**Figure 3.6**: Pressure Drop Holder
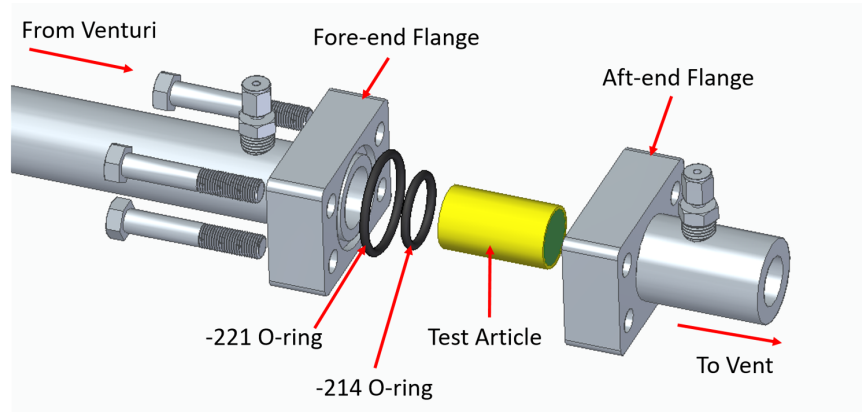
**Figure 3.7**: Pressure Drop Holder Diagram

All parts are designed to withstand a pressure of 3000 psi. One pipe is 6"
long, and is threaded on one end to allow the attachment of a swagelok adapter to
interface with the rest of the spray facility system. It has an internal diameter of
0.56", but a region before the flange that is machined to a 0.75" inner diameter. This
is done to ensure a steady flow enters the grain. The pipe is welded to a stainless steel
flange with an o-ring gland groove that houses a size 221 o-ring to seal flow between
the two flanges. This flange is bolted to another flange of the same type, with a
triangular 0-ring groove machined to house a size 214 o-ring. This ring will prevent
flow from bypassing the grain structure. On the other end of this flange is a 3" long
stainless steel pipe with a 1" inner diameter machined 1" deep to house the porous
grain with the epoxied sleeve. Beyond this pocket is a machined internal diameter of
0.75". This is designed to catch the epoxied sleeve of the grain, securing the grain in
the flow while not obstructing the flow passages within the porous grain. The porous
grain will extend from the flange hole into the other flange, and can be manually

inserted and removed between tests after unbolting the flanges. Both flanges initially had threaded holes, but the fore end flange hole threads were bored out to allow the bolts to be threaded in and tightened to produce a seal. Pressure transducer and thermocouple ports are machined into the fore end pipe just before the flange in order to measure injector temperature. The aft end pipe exits to atmosphere and therefore atmospheric exit pressure can be assumed.

The full experimental procedures for the pressure drop measurements have been documented in the PRC standard operating procedure PRC-SOP-JRC-059-A.0. This procedure is provided in Appendix A.

## 3.2   Microstructural Analysis

Once X-ray transmission image data is acquired, XCT is used to reconstruct the images into an image stack with data that can then be used to evaluate microstructural properties of interest within the porous hybrid motor grains. These properties then form the fundamental basis for the ATN resistance network model that is used to calculate the pressure drop within the grain.

### 3.2.1   Image Processing

After aqcuiring transmission images, the reconstruction was conducted using Octopus (InsideMatters Aalst, Belgium) tomographic reconstruction software. In a tomographic reconstruction, transmission images of the sample in angular increments through a full rotation are acquired. Next, these images are processed into a sinographic representation of the data, and finally processed into a vertical cross-sectional

image stack through an inverse radon transform (Figure 3.8). A pixel size of 32 microns was estimated from the transmission images. The source-object distance was approximately 640 mm and source-detector distance was approximately 1012 mm. Center of Rotation (COR) was found by first using the automated finder, and then manually iterating until the clearest images were observed. Ring filters were applied to reduce the occurence of ring artefacts within the transmission images to more clearly define the porous spaces. The center of rotation (COR) was initially determined from the software algorithm, and then refined to produce the greatest image quality.
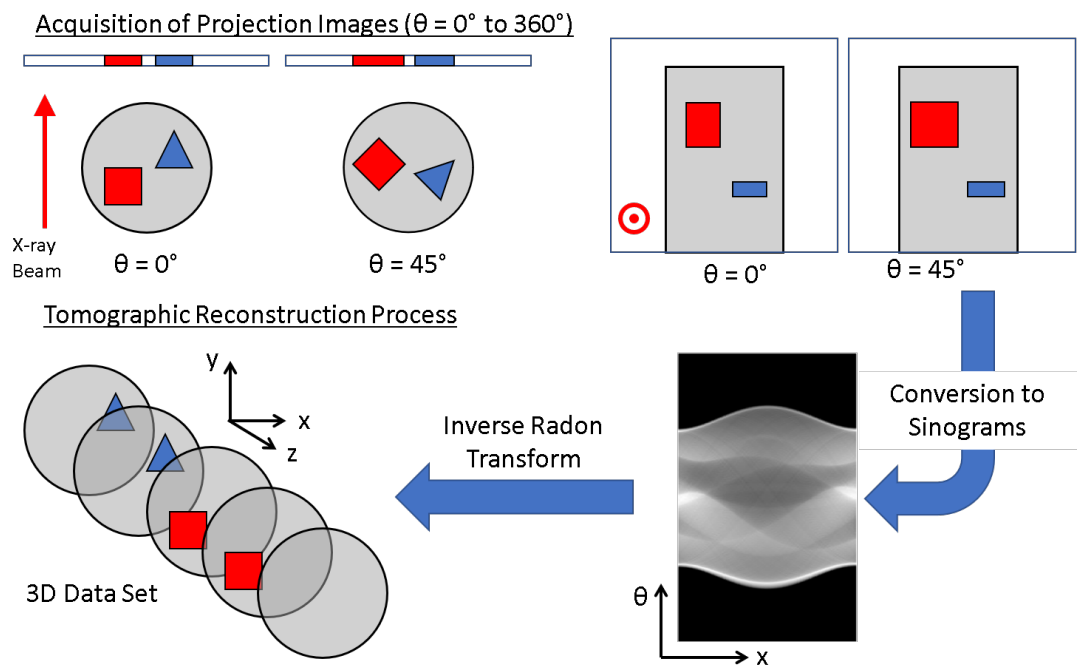


**Figure 3.8**: Tomographic Reconstruction Process from Acquisition to 3-D Data

X-ray-computed tomography was conducted in the HPL in accordance with the non-energetic x-ray imaging standard operating procedure (PRC-SOP-HPL-013). The source voltage was set to 50 kV, and the detector was set to high-resolution mode. In this setting, higher resolution is traded for less total material covered in the image data. This is believed to be an acceptable tradeoff due to the lack of variation axially in the key property of porosity demonstrated from previous tests [79]. Images were acquired in quarter degree increments through a full 360 degree rotation. At each increment, 16 images were acquired and averaged together into a single image for each increment. This procedure reduced noise within the images. In some cases, slight blur occured as a result of the sample being slightly tilted from the axis. To account for this, the center of rotation (COR) was adjusted to produce the highest quality image possible.

The data was first processed by applying a threshold method to the reconstructed image, which entails converting the grayscale pixels into a collection of black and white pixels denoting void and solid space respectively (Figure 3.10). The threshold is defined as the grayscale value at which values above are defined as solid space, and values below are defined as void space. It is important to note that this is a two-phase application, there exist other scenarios in which three-phase thresholds can be used. The threshold value was determined by visually inspecting the reconstructed sample, and choosing several regions of interest encompassing void spaces. The mean and standard deviation were found, and the threshold was selected as the "right tail" (mean +2 standard deviations) to encompass the 95 percent confidence interval.

To validate this approach, a solid plexiglass cylinder with a 0.25" central drilled bore was imaged with bore grayscale values compared to those of porous regions within the grain (Figure 3.9). Specifically, the grayscale value of background regions outside of the samples and void regions within the samples were computed and compared (Table 3.1). The ratio of background grayscale value of the calibration sample to that of the 200 micron NPS sample was determined, and then the average internal void grayscale of the calibration sample was divided by this value and compared to that of the 200 micron sample. The resulting grayscale value of 14547 was within $2\sigma$ of the average grayscale of the void space within the 200 micron NPS sample, confirming the grayscale match of void space (Table 3.2).
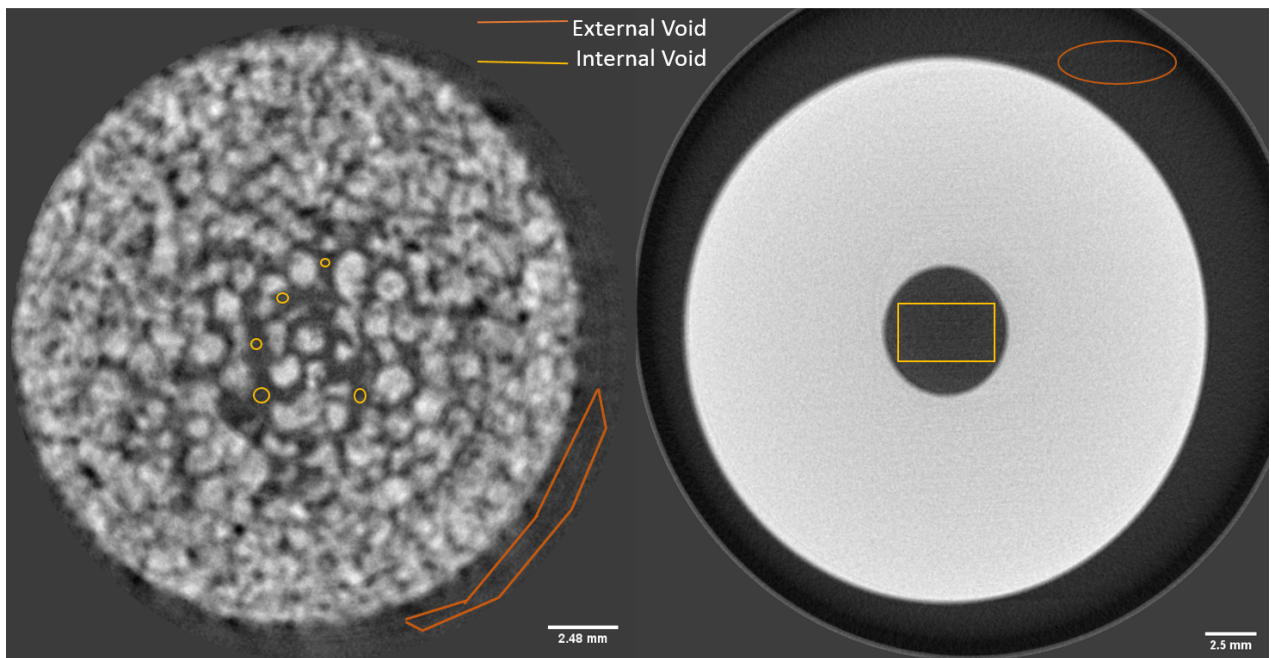


**Figure 3.9**: Plexiglass Calibration Sample

**Table 3.1**: Calibration vs. XCT Sample Grayscale Comparison

|  | GS200NPS | $\sigma_{200NPS}$ | GScal | $\sigma_{Cal}$ |
|---|---|---|---|---|
| External Void | 14026 | 1762 | 27913 | 418 |
| Internal Void | 16640 | 1695.8 | 28950 | 577 |

**Table 3.2**: Calibration Results

| GScal/GS200micronNPS | lower bound | upper bound | Result |
|---|---|---|---|
| 1.99 | 13248 | 20031 | 14547 |
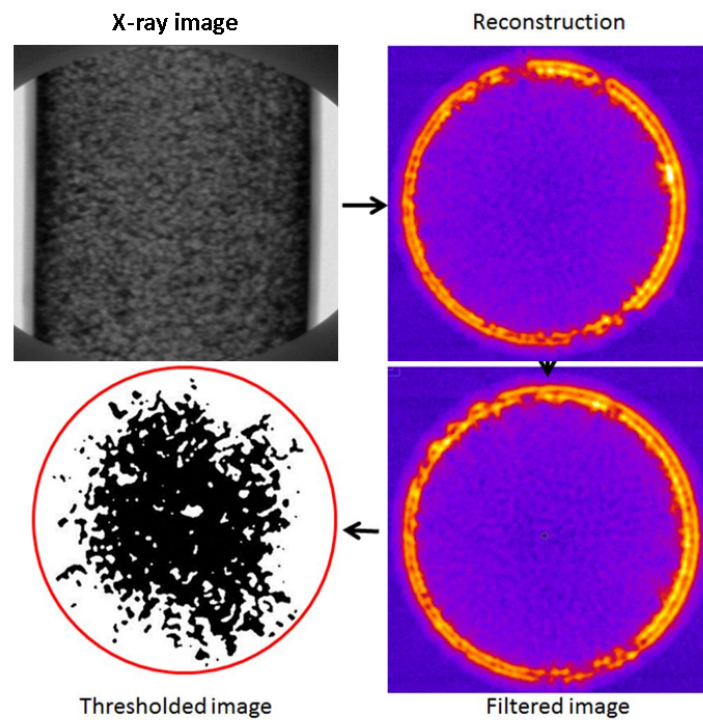


**Figure 3.10**: Data Collection Procedure

Data used in previous works was imaged in a low-resolution mode, and median filters were applied to reduce noise. However, the data in this set did not have filters applied. The histograms were adjusted to make void spaces more visible however.

### 3.2.2   Microstructural Characterization

Once the thresholds were determined, porosity was determined by a straight-forward voxel counting method. A voxel is defined as a pixel with depth (i.e. a 3-D pixel). The number of porous (black) voxels were counted along with the total number of voxels, and these two values were computed as a ratio of porous space to total space.

Average Pore size was determined according to a method outlined by Munch and Holzer [51]. Paraphrasing this process, the thresholded images are further analyzed with a distance transform, a re-mapping of the porous space grayscale values to distances from the nearest solid pixel. By finding the local maximum in a pore space, a representative location of the pore center is determined. Once the local pore centers are found, spheres are fixed to these central locations and successively dilated until they touch the solid space. This procedure is completed axially and radially (i.e. in 3 dimensions). At each point of dilation, the cumulative volume of the spheres is taken. Once this process is complete, a cumulative size distribution is obtained (Figure 3.11). This process can be repeated with the pore and solid thresholed pixels inverted, yielding a distribution of solid particle sizes known as the cumulative solid distribution (CSD).
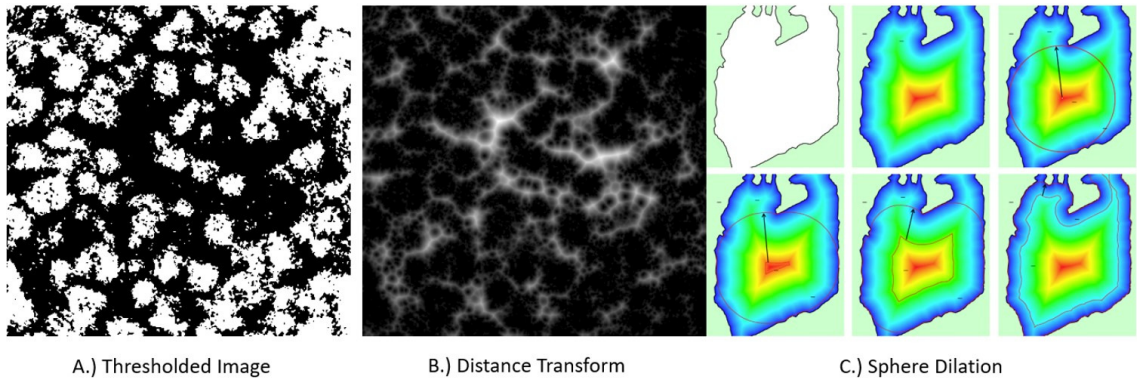
**Figure 3.11**: PSD/CSD Determination Process. The thresholded image (A) is processed via a distance transform (B) to determine the pore centers at which spheres are fixed and dilated to determine the distribution (C) [51]

The overall pore size distribution (PSD) and cumulative size distribution (CSD) were calculated for the sample set. PSD corresponds to the distribution of porous space, and CSD to that of solid particle space. From these results average pore size and average solid particle size were computed and compared to other data. The average pore size was not directly used in the ATN model pressure drop data, but by comparing to experimental methods serves the purpose of XCT data validation. By contrast, the average particle size determined by CSD was used as the characteristic length in the correlation predictions.

### 3.2.3 ATN Analysis

ATN Network Theory is an adaption of the previously mentioned heuristic model from an electrochemical application to a mechanical flow application. In essence, it functions the same way as a resistor-circuit model. In these circumstances,

modes of energy loss to the flow are treated as "resistors" in the flow circuit model. In this case, the flow losses are believed to primarily result from the flow contractions, expansions, and directional vector changes resulting from travel through the porous medium.

In the ATN model, each channel is broken down into a set of node points and edges (Figure 3.12). Each of these vertices have key parameters of tortuosity and varicosity that are equated to path resistances, or local pressure drops. Once the individual channels are assembled, a global network model can be assembled.
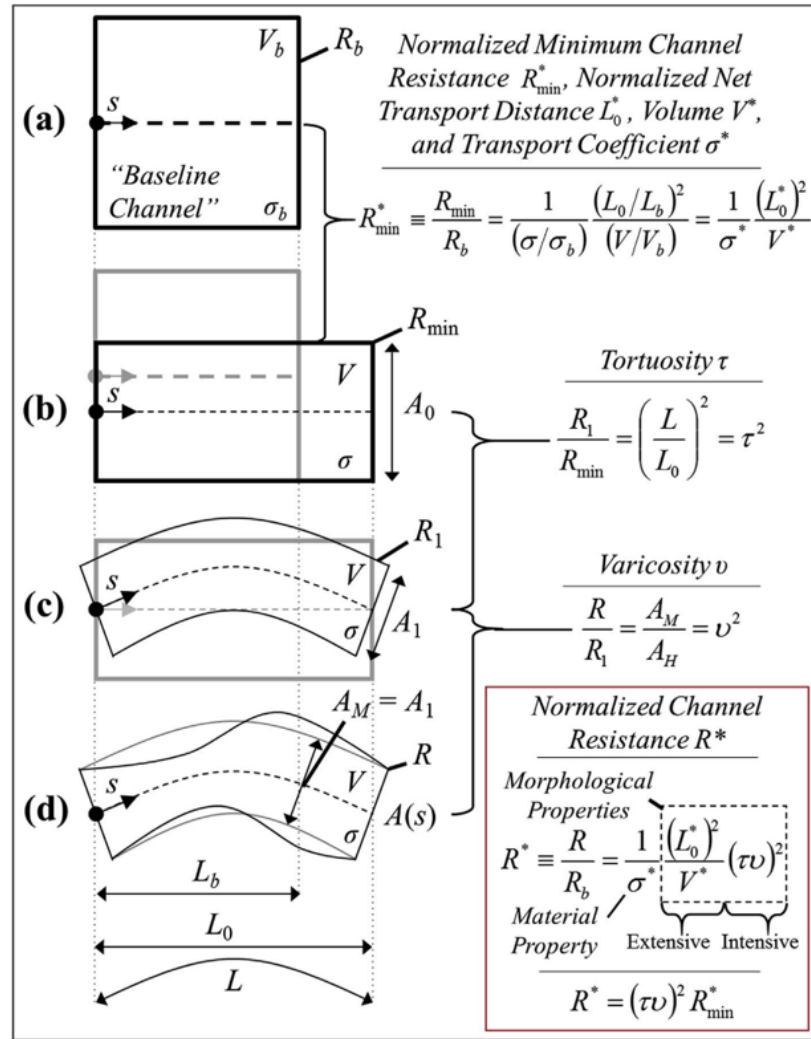
**Figure 3.12**: ATN channel creation. A "baseline" channel is defined, then stretched, then bent, then dilated and contracted. Throughout each step in the process, mathematical relationships are mapped to relate the final channel to the initial channel via a ratio, and an individual channel resistance as a function of tortuosity and varicosity is determined. [5]

Morphologically, the pressure drop ATN model is identical. The main difference is the definition of the transport coefficient $\sigma$. In mechanical transport, it is defined as $\mu$, and has the same units as viscosity. While it has the same units, it

shouldn't be assumed that viscous effects are significantly present as flows occur well outside the laminar region.

In electrical transport, the resistance is defined as the amount of potential, or voltage, required to drive an electrical current through a path. In mechanical transport, this can be defined as the ratio of a driving force difference to mass flow through a specific path:

$$R_{elec} = \frac{V}{I} \tag{3.6}$$

$$R_{mech} = \frac{\Delta F}{\dot{m}} \tag{3.7}$$

When this equation is divided by the cross sectional area, it becomes a ratio of the pressure drop to the mass flux:

$$R = \frac{\Delta P}{\dot{m}"} \tag{3.8}$$

In this model, the minimum case is defined as the baseline case, namely a straight constant diameter channel. This minimum resistance case channel is then bent with a constant curvature, with tortuosity defined as ratio of the length of the curved channel to the length of the straight channel

$$\frac{R_2}{R_1} = \frac{L}{L_o}^2 = \tau^2 \tag{3.9}$$

Finally, the curved channel is expanded and contracted. The ratio of the original cross-sectional area to the harmonic mean of the area is defined as the varicosity.

$$\frac{R_c}{R_2} = \frac{A_M}{A_H} = \nu^2 \tag{3.10}$$

The above equations are combined into a relationship between the minimum resistance case and contorted channel

$$R^* = \frac{R_c{}^2}{R_1} = \mu \frac{L^*_o{}^2}{V^*}(\tau \nu^2) \tag{3.11}$$

This can also be expressed as:

$$R^* = R_1(\tau \nu^2) \tag{3.12}$$

The XCT data can be used to dissect a porous network into a collection of channels with the above relations. While each individual channel must have constant tortuosity and varicosity, the network can consist of channels with different tortuosities and varicosities compared to each other.

At the network scale, a similar approach is taken to find the overall network resistance (Figure 3.13). An overall minimal material resistance is defined, in the ATN case this is an open channel with the same overall volume as the material. However, in the case of pressure drop through a porous media, the analogy of flow through an open pipe results in too low of a pressure drop. In this case, the Ergun equation was applied to a case of a highly porous material with a porosity of 0.99 and an average

solid particle radius of 32 microns, the resolution of the XCT system. This theoretical minimum pressure drop, coupled with the equivalent mass flux was used to solve for a minimum resistance. Combined with the transport coefficient ratio solved for from the network analysis, an effective network resistance is solved for and used to predict a pressure drop.

$$R_{mat,min} = \frac{\Delta P_{min}}{\dot{m}"} \tag{3.13}$$

$$\mu_{mat,min} = R_{mat,min} \frac{0.99 A_{grain}}{L_{grain}} \tag{3.14}$$

$$\mu_{eff} = \frac{\mu_{mat,min}}{\frac{\mu_{mat,min}}{\mu_{eff}}} \tag{3.15}$$

$$R_N = \frac{\mu_{eff} L_{grain}}{A_{grain} \epsilon} \tag{3.16}$$

$$\Delta P = R_N \dot{m}" \tag{3.17}$$
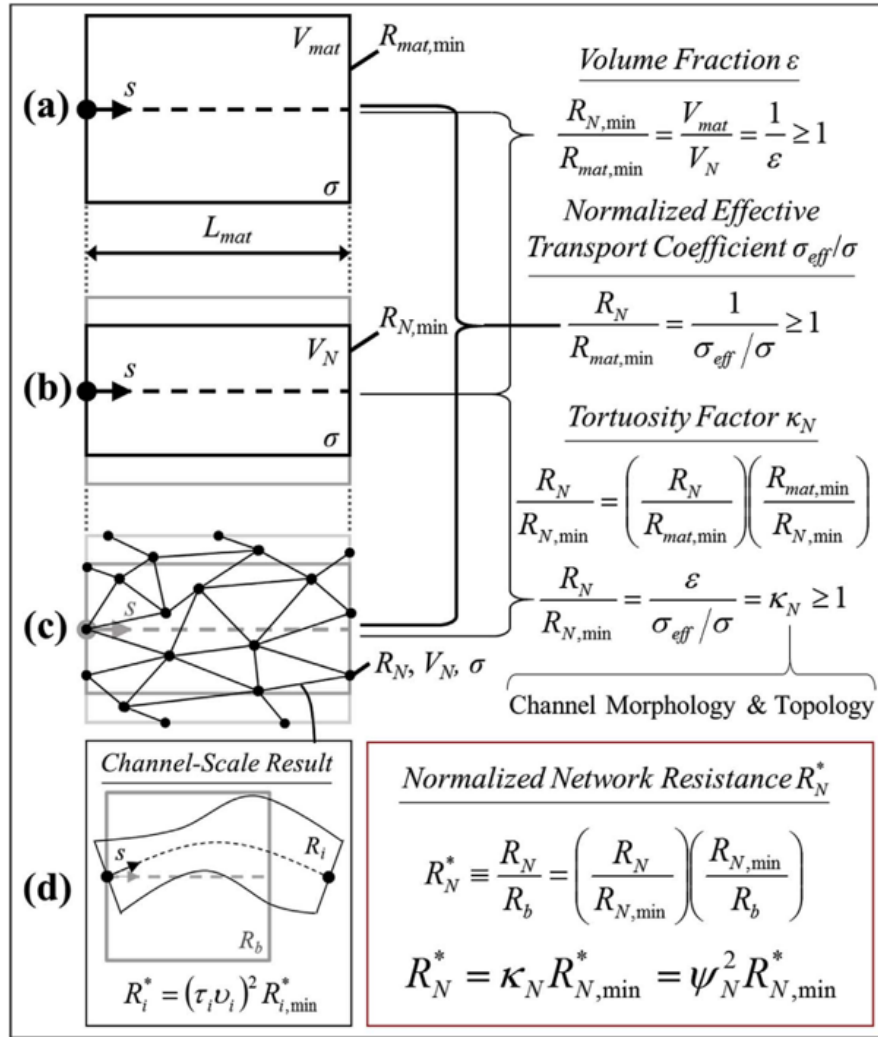
**Figure 3.13**: Generation of an ATN Network. An individual "baseline" network is defined. The nodes and vertices for individual channel calculations are implemented into the overall network model, and finally a resistance ratio is defined. [5]

The ATN algorithm previously used for electrochemical network modeling was applied to the porous hybrid CT data. The collected XCT porous hybrid data was shared with Dr. Alex Cocco (Advanced Technology Research Corporation, Beltsville, MD), who performed the ATN code analysis for this data set. The porous network was broken into a collection of edges and nodes, and based on tortuosity and vari-

cosity, effective network resistance ratios were calculated. A "baseline" pressure drop case was defined by applying the Ergun equation to a highly porous medium. A minimum resistance transport coefficient was computed from this result, and the transport coefficient ratio output from the ATN code was used to ultimately determine a pressure drop prediction. By modifying the grain length in the baseline pressure drop and transport coefficient equations, this model can be scaled assuming the grain structural properties remain constant.

# CHAPTER 4

## MICROSTRUCTURAL CHARACTERIZATION

*You don't concentrate on risks. You concentrate on results. No risk is too great to prevent the necessary job from getting done.*

—Chuck Yeager

This section details the microstructural x-ray data that serves as the foundation for the ATN model. First, XCT data from the UAH system is compared to data acquired from a high-resolution source in order to ascertain that resolution is not a critical limiting factor. The porosity determined from the XCT data is compared to the archimedes method results to verify similarities in this x-ray derivitive measure. Average pore size is compared to results found from SEM data and high resolution x-ray data.

Finally, results of the ATN characterization are detailed. The ATN characterization routine involves breaking up the porous network into a collection of individual channel segments. At this point, arbitrary straight channel shapes and then bended and cross sectional area is varied until the tortuosity and varicosity mimic those of the individual channel segments. In each step of this process, a resistance ratio is calculated which is ultimately used to relate the baseline shape to the final shape.

Once this process is completed, the channels are assembled into a porous channel network. The combination of resistance ratios is used to determine an overall network resistance ratio. A "baseline" minimum resistance network case is computed from applying the Ergun equation to a maximum porosity channel of similar dimensions to the grain. The resistance from this case can be used to find a representative minimum resistance transport coefficient, and the network-determined transport coefficient ratio $\frac{\mu}{\mu_{eff}}$ can be used to find the effective network transport coefficient. From this value, a representative pressure drop is calculated.

## 4.1  X-ray Data Characterization

A set of 10 samples each from a 200 micron NPS and 100 NPS stack were analyzed. In both stacks, the hi-res mode was used. Unfortunately, while this resulted in a higher pixel resolution, it also made it impossible to capture the whole grain surface in the field of view. Fortunately, previous studies provided evidence that axially properties remain fairly consistent. The total length covered is detailed and was calculated by multiplying the stack slice count by the resolution, or estimated vertical distance per slice.

In the 200 micron case, the calculated porosity was fairly consistent with the exception of the first two samples (Table 4.1). In the 100 micron NPS cases, the porosity was fairly consistent among all samples (Table 4.2). The total grain length covered in the 200 and micron samples remained consistent within the sets, but varied quite a bit in comparison. It is important to note that in the 200 micron samples, there were alignment issues in which the samples were tilted during ct acquisition.

As such, center of rotation alignment was not as good as the 100 micron sample resulting in more blur regions further away from the sample center. These regions were cropped.

**Table 4.1**: 200 Micron NPS Grain Specimen Porosities and XCT Length Covered

| Grain Specimen | XCT Length Covered (mm) | $\epsilon$ |
|:---:|:---:|:---:|
| 200-1 | 5.92 | 0.44 |
| 200-2 | 5.97 | 0.41 |
| 200-3 | 6.09 | 0.44 |
| 200-4 | 5.86 | 0.49 |
| 200-5 | 5.96 | 0.48 |
| 200-6 | 5.86 | 0.48 |
| 200-7 | 5.89 | 0.48 |
| 200-8 | 5.89 | 0.48 |
| 200-9 | 5.98 | 0.49 |
| 200-10 | 5.96 | 0.49 |

With validated data, it is worthwhile to look at representative subvolumes (RSVs) of the porous media in order to account for variations in porous behaviour. First, radial porosities with circular cross sections were observed (Figure 4.1). Second, vertical (axial) porosity RSVs were investigated (Figure 4.2):

**Table 4.2**: 100 Micron NPS Grain Specimen Porosities and XCT Length Covered

| Grain Specimen | XCT Length Covered (mm) | $\epsilon$ |
|:---:|:---:|:---:|
| 100-1 | 12.59 | 0.49 |
| 100-2 | 17.5 | 0.48 |
| 100-3 | 21.53 | 0.49 |
| 100-4 | 21.97 | 0.51 |
| 100-5 | 19.43 | 0.47 |
| 100-6 | 21.62 | 0.47 |
| 100-7 | 21.24 | 0.48 |
| 100-8 | 21.02 | 0.49 |
| 100-9 | 16.57 | 0.50 |
| 100-10 | 18.29 | 0.47 |
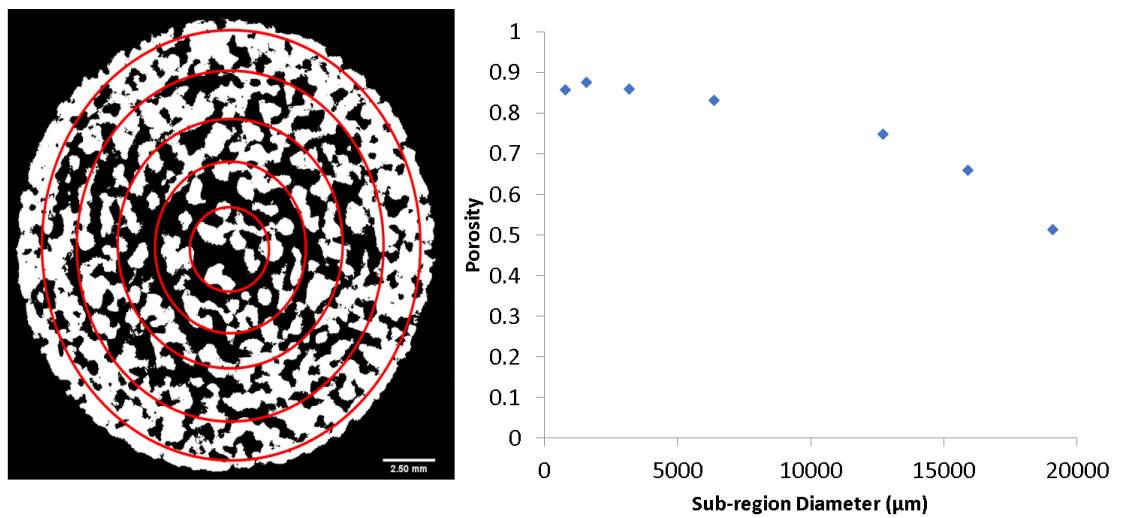


**Figure 4.1**: 200 micron circular cross section RSV regions (left) and porosity results (right)
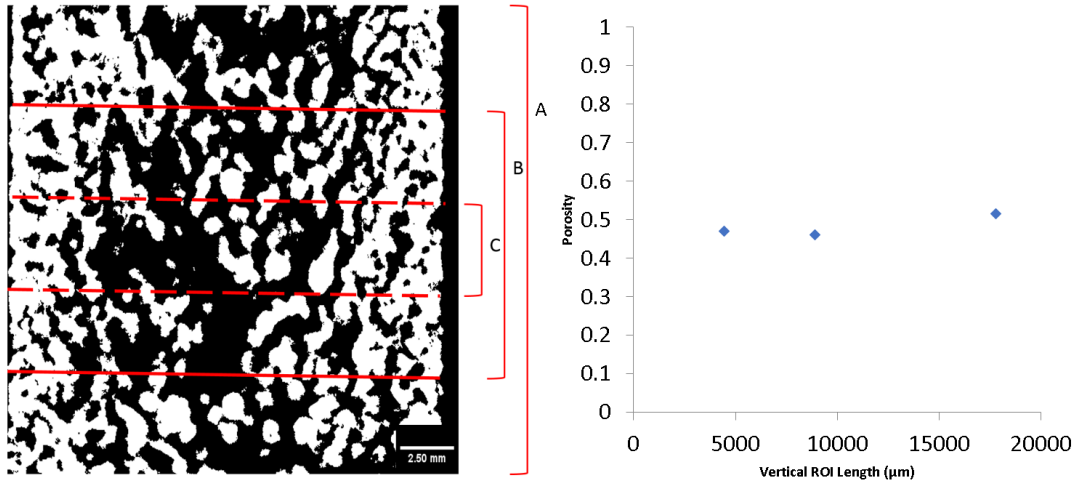
**Figure 4.2**: 200 micron vertical RSVs (left) and corresponding vertical porosities (right)

Upon examining the data, it is clear that axially (from the forward to aft end) of the grain, porosity tends to vary little. However, examining the grains radially, the porosity appears to be much greater in the center and smaller toward the peripheral regions. This trend was encountered consistently for every sample in the set. While the overall porosity remains around 0.48-0.49, the local porosity in the central region tends to be closer to 0.8-0.9. Data from a second grain from a higher quality CT scan reveals a porosity around 0.6.

In addition to varying RSV size, RSV shape was modified. Several square RSV cross-sections were taken (Figure 4.3). The architecture of the ImageJ algorithm for PSD estimation only accepts rectangular image inputs, so additionally this RSV study is useful for analyzing direct inputs to the PSD and CSD algorithm calculations.
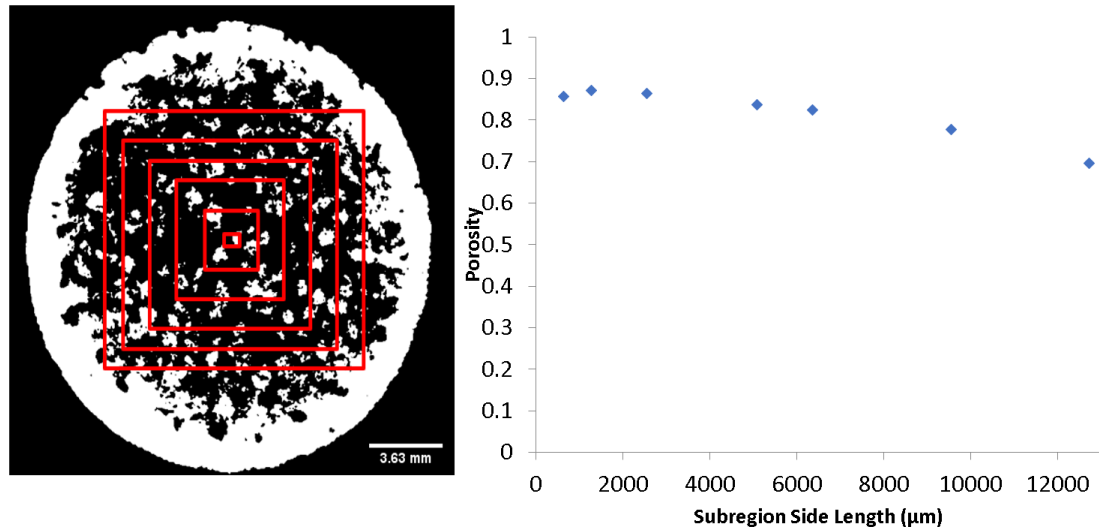
**Figure 4.3**: 200 micron square cross section RSV regions (left) and porosity results (right)

The data behaved in a similar manner to the previous circular cross sections. Porosity initially was at a very high level, and gradually decreased to about 70 percent. Ultimately, it did not approach the overall sample average porosity. This is likely due to the fact that the square RSV cross-sections were unable to capture a significant amount of the highly solid peripheral regions of the grain without occupying external space.

#### 4.1.0.1 Validating Archimedes, SEM, and high resolution x-ray data

Archimedes tests conducted according to the modified ASTM standard produced very consistent results with porosities varying from 0.48 to 0.5. This was true for both the 200 micron NPS (Table 4.3) and 100 micron NPS cases (Table 4.4).

**Table 4.3**: 200 micron series Archimedes Tests

| Grain Specimen | $W_d$ | $W_{sus}$ | $W_{sat}$ | $V_{ext}$ | $V_p$ | $V_{sol}$ | $\epsilon$ |
|:---:|:---:|:---:|:---:|:---:|:---:|:---:|:---:|
| 200-1 | 6.09 | 0.93 | 10.79 | 12.49 | 5.96 | 6.54 | 0.48 |
| 200-2 | 5.98 | 0.93 | 10.92 | 12.67 | 6.26 | 6.40 | 0.49 |
| 200-3 | 5.86 | 0.94 | 10.40 | 11.99 | 5.75 | 6.24 | 0.48 |
| 200-4 | 5.96 | 0.96 | 10.68 | 12.32 | 5.98 | 6.34 | 0.49 |
| 200-5 | 5.97 | 0.96 | 10.53 | 12.13 | 5.78 | 6.35 | 0.48 |
| 200-6 | 5.92 | 0.95 | 10.44 | 12.03 | 5.73 | 6.29 | 0.48 |
| 200-7 | 5.88 | 0.93 | 10.48 | 12.10 | 5.82 | 6.28 | 0.48 |
| 200-8 | 5.89 | 0.90 | 10.47 | 12.13 | 5.80 | 6.33 | 0.48 |
| 200-9 | 5.96 | 0.90 | 10.58 | 12.27 | 5.86 | 6.42 | 0.48 |
| 200-10 | 5.86 | 0.94 | 10.52 | 12.14 | 5.91 | 6.23 | 0.49 |

**Table 4.4**: 100 micron Series Archimedes Tests

| Grain Specimen | $W_d$ | $W_{sus}$ | $W_{sat}$ | $V_{ext}$ | $V_p$ | $V_{sol}$ | $\epsilon$ |
|:---:|:---:|:---:|:---:|:---:|:---:|:---:|:---:|
| 100-1 | 5.84 | 0.99 | 10.46 | 12.00 | 5.85 | 6.15 | 0.49 |
| 100-2 | 5.57 | 0.82 | 10.07 | 11.72 | 5.70 | 6.02 | 0.49 |
| 100-3 | 5.76 | 0.91 | 10.30 | 11.90 | 5.75 | 6.15 | 0.48 |
| 100-4 | 5.66 | 0.83 | 10.20 | 11.88 | 5.75 | 6.13 | 0.48 |
| 100-5 | 5.75 | 0.87 | 10.09 | 11.69 | 5.50 | 6.18 | 0.47 |
| 100-6 | 5.78 | 0.93 | 9.93 | 11.40 | 5.26 | 6.14 | 0.46 |
| 100-7 | 5.47 | 0.82 | 9.83 | 11.42 | 5.53 | 5.89 | 0.48 |
| 100-8 | 5.85 | 0.93 | 10.39 | 11.99 | 5.75 | 6.24 | 0.48 |
| 100-9 | 5.75 | 0.91 | 10.50 | 12.16 | 6.02 | 6.14 | 0.50 |
| 100-10 | 5.63 | 0.94 | 9.86 | 11.30 | 5.37 | 5.94 | 0.48 |

The external hi-res data from ZEISS was analyzed, and predicted a slightly higher porosity (Table 4.5). This is likely due to the fact that the ZEISS higher quality data resulted in the detection of internal void spaces that were not detected

by the UAH system and had no path of penetration for the Archimedes method, and

therefore biased the results toward a higher porosity (Figure 4.4).

**Table 4.5**: Comparison of archimedes and XCT porosity results for 200 micron NPS series [9]

| $\epsilon_{Archimedes}$ | $\epsilon_{UAH}$ | $\epsilon_{ZEISS}$ | $\xi_{ArchimedesUAH}$ | $\xi_{ArchimedesZEISS}$ |
|:---:|:---:|:---:|:---:|:---:|
| 0.481 | 0.474 | 0.55 | 1.390 | 15.892 |
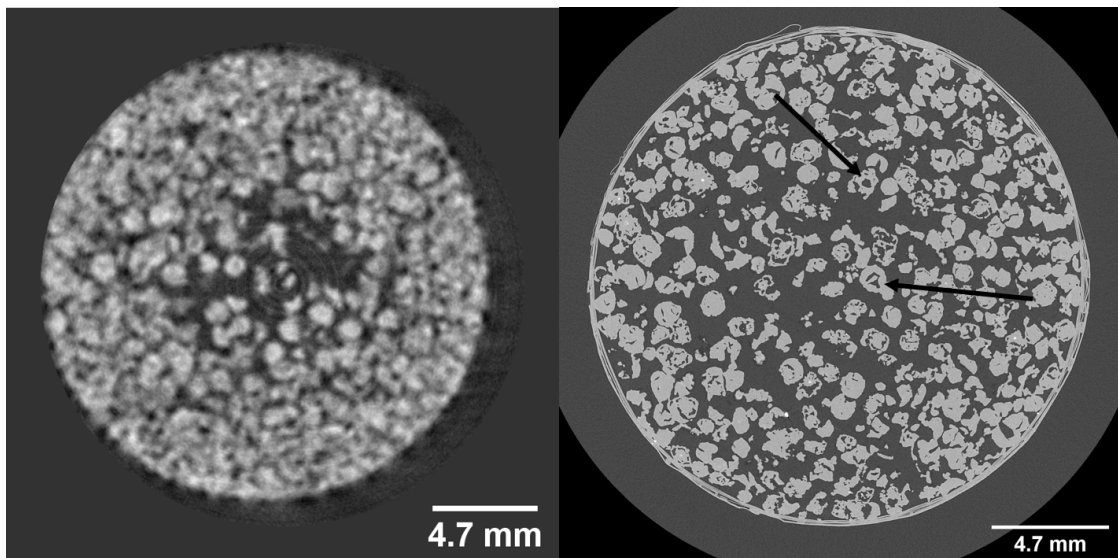


**Figure 4.4**: 200 micron NPS Grain data from UAH XCT system (left) and ZEISS XCT system (right). The arrows denote internal porous areas within solid parts of the grain detected by the ZEISS XCT system that could explain a higher observed porosity.

### 4.1.1   Pore Size Distribution (PSD)

Comparing the cumulative PSD results of the UAH system, ZIESS system, and SEM data, a fair amount of variation is observed (Figure 4.5). The SEM data

tends to have a leftward distribution, especially at higher magnifications. This could be due to the fact that at higher magnifications smaller pores are resolved, and larger pores potentially exceed the dimensions of the field of view, resulting in these pores being only partially present in the image. The SEM distributions tend to have rougher curvatures as well, this is possibly the result of the 2D nature of the SEM data. The 3D ZEISS and UAH distributions follow similar trends, although the ZEISS data is skewed slightly leftward likely due to the detection of smaller pores and internal void spaces within the solid.
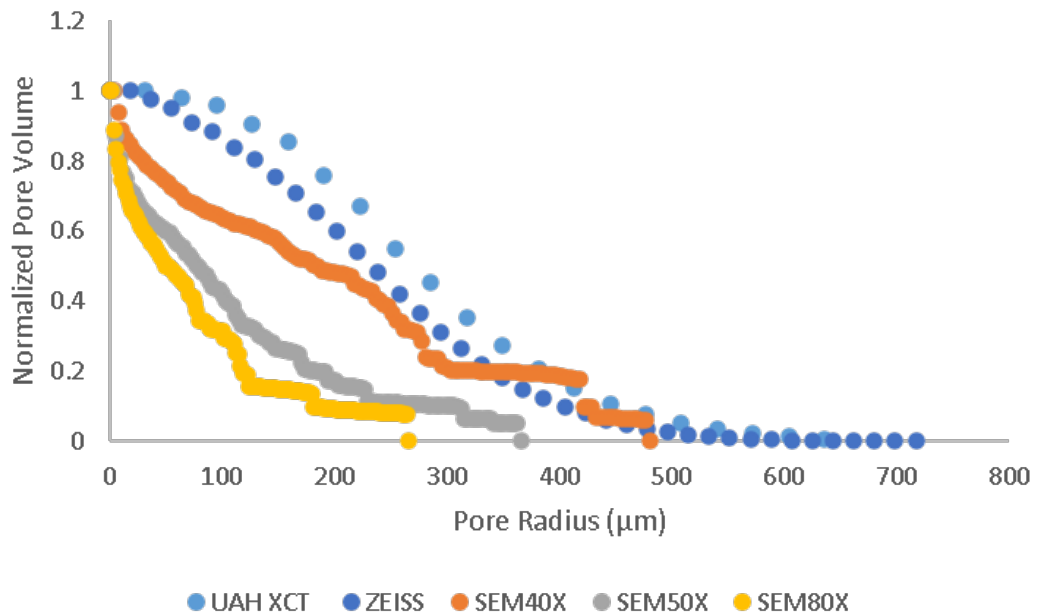


**Figure 4.5**: 200 micron XCT, ZEISS, and SEM PSD

Examining PSD of the RSVs of various size, it is observed that the overall distribution appears to initially skew to a higher pore size and then contracts to a smaller pore distribution (Figure 4.6). This suggests that the more porous areas are

comprised directly of larger pores as opposed to having a larger quantity of smaller pores, while the more solid external region is comprised of smaller pores.
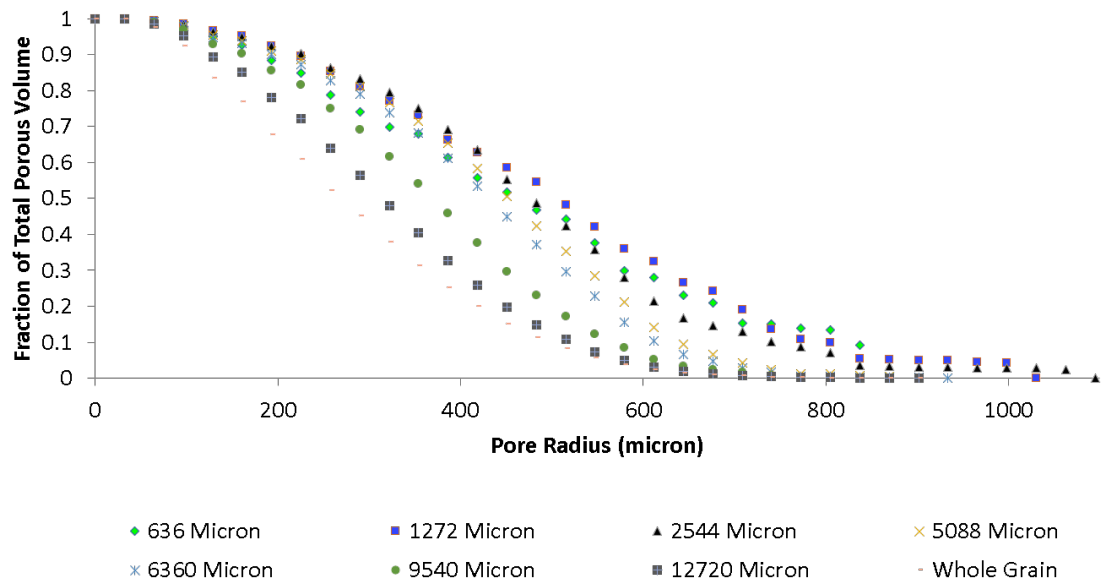


**Figure 4.6**: 200 micron RSV Square PSD Distribution

### 4.1.2 Validating SEM, and external x-ray data

Once the SEM data was collected (Figure 4.7), average pore size was estimated using two methods. First, the images were calibrated and subsequently distances between two solid particles were estimated at ten random locations (Figure 4.8). Second, the PSD algorithm previously used was applied to the thresholded SEM images and ZEISS data (Figure 4.9).
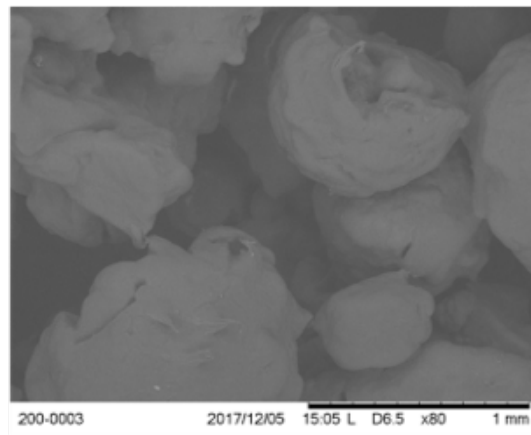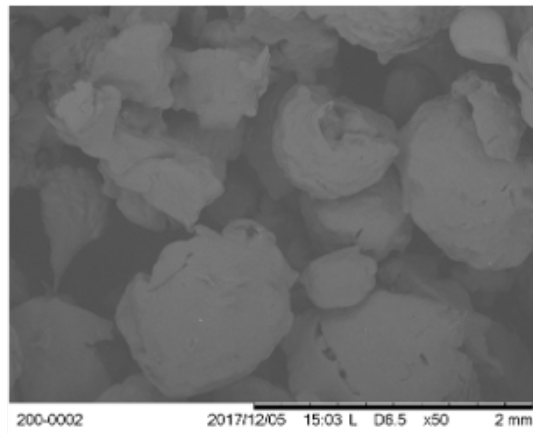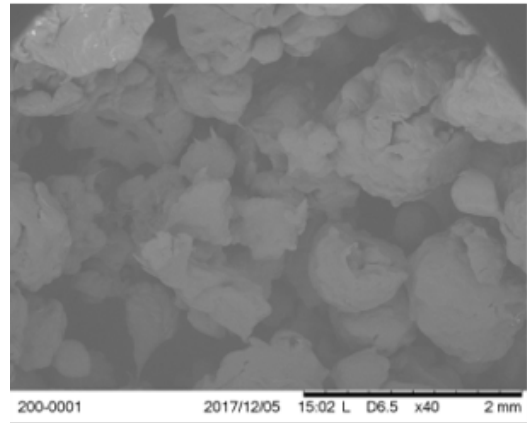
**Figure 4.7**: SEM 40X (Top), 50X (Middle), and 80X Mag (Bottom) of 200 micron NPS Grain
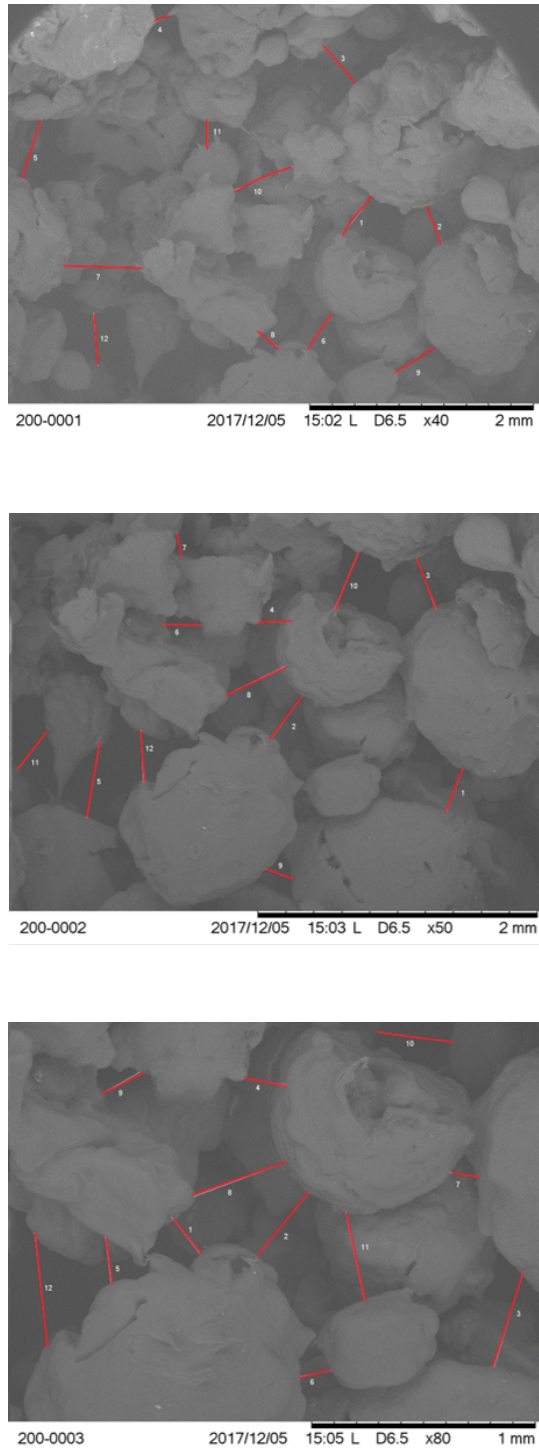
**Figure 4.8**: SEM 40X (Top), 50X (Middle), and 80X Mag (Bottom) of 200 micron NPS Grain with Lines Denoting Measured Pore Diameters
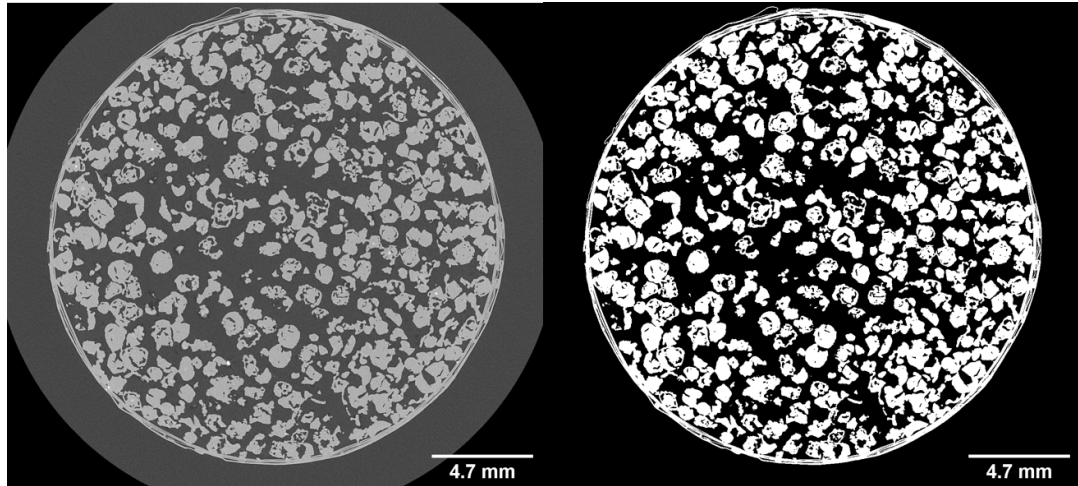
**Figure 4.9**: ZEISS Data Thresholding

The comparison of thresholded images gives a bit more detail to the PSD process applied to the SEM images (Figure 4.10). One challenge of these images is the fact that 3-D effects are "baked" into a 2-D depiction of data. The grayscale intensity variation of some of the solid particles is a result of "depth". As a result it is difficult to account for variations in the "depth" plane.
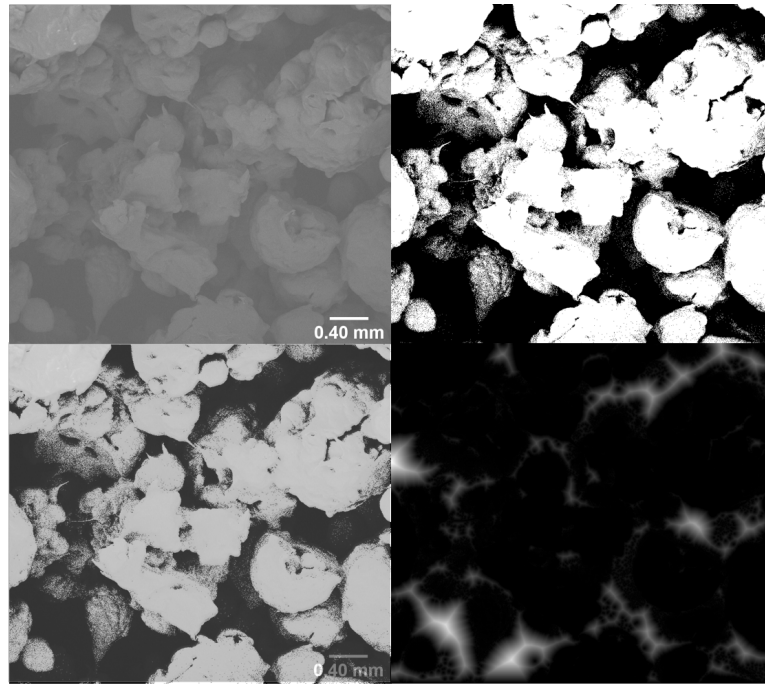
**Figure 4.10**: SEM Raw Image (Top Left), Filtered Image (Lower Left), Thresholded Image (Top Right), and Distance Map (Lower Right)

Both the PSD and CSD distributions were normalized as fractions of the maximum pore and solid particle sizes respectively. The distributions for both the 200 and 100 micron series CSDs were surprisingly similar (Figure 4.11 and Figure 4.13). This trend was observed in the PSD data as well (Figure 4.12, Figure 4.14, and Table 4.6).

It is important to note that the CSD calculated from the SEM data is slightly less than that of the XCT data. This could be due to the fact that the SEM data was centered in the central region of the grain, a region known for high porosity, while the XCT data encompassed a greater cross section of the grain. The high porosity possibly inversely contributed to a lower average solid particle size.
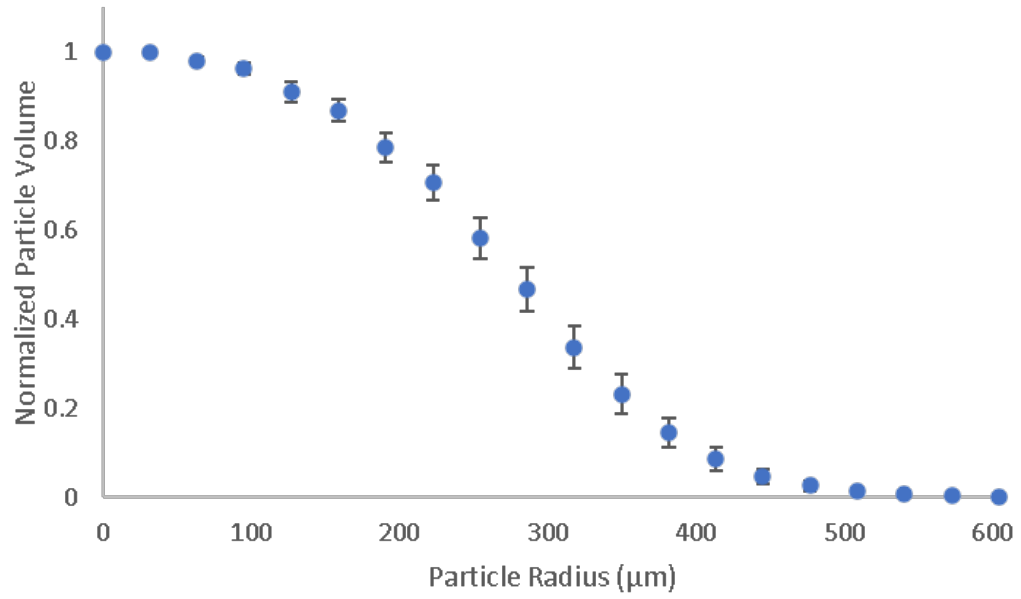
**Figure 4.11**: 200 micron NPS Series Overall Cumulative CSD
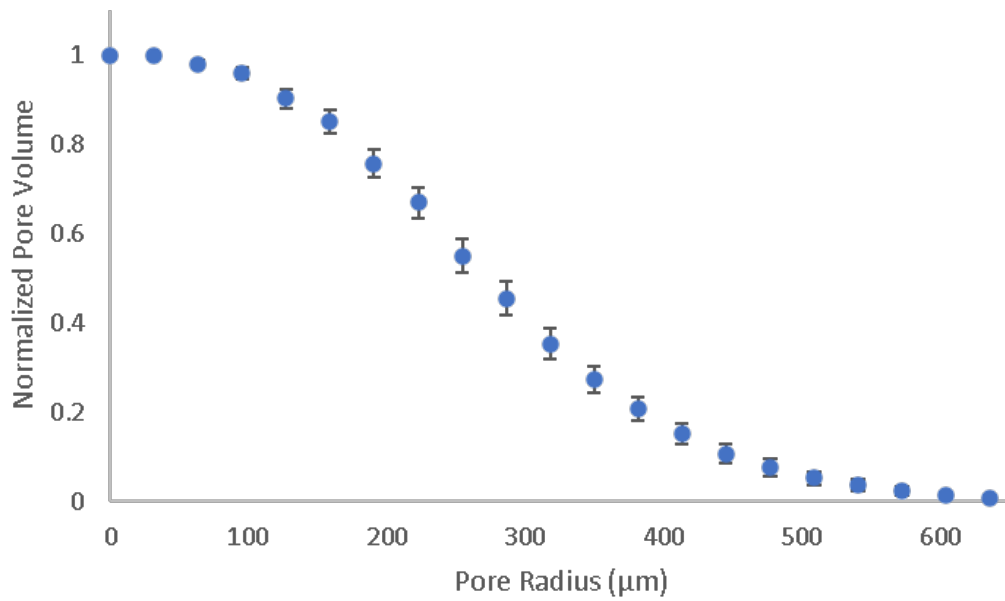


**Figure 4.12**: 200 micron NPS series Overall Cumulative PSD
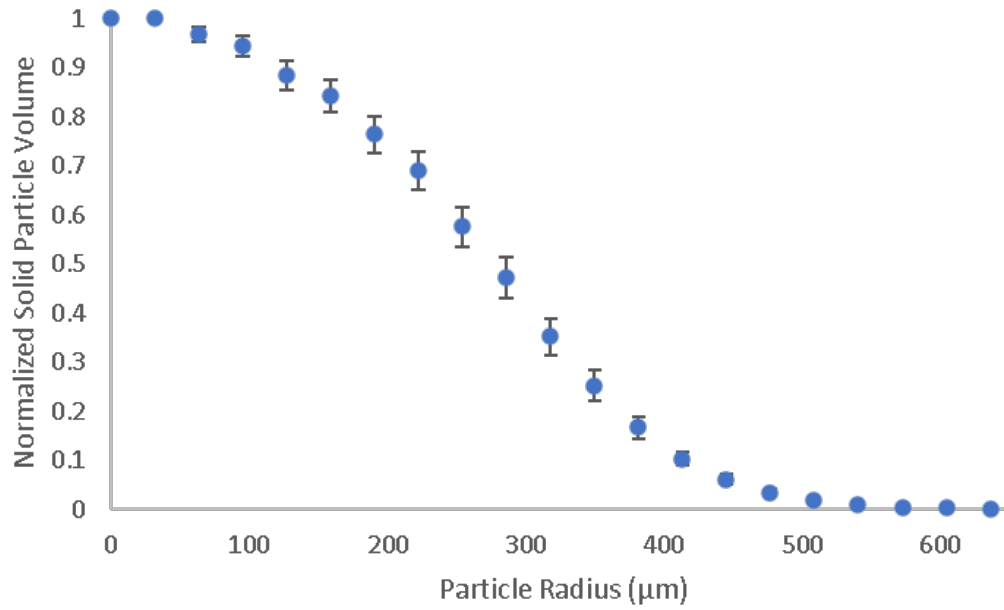
**Figure 4.13**: 100 micron NPS series overall cumulative CSD
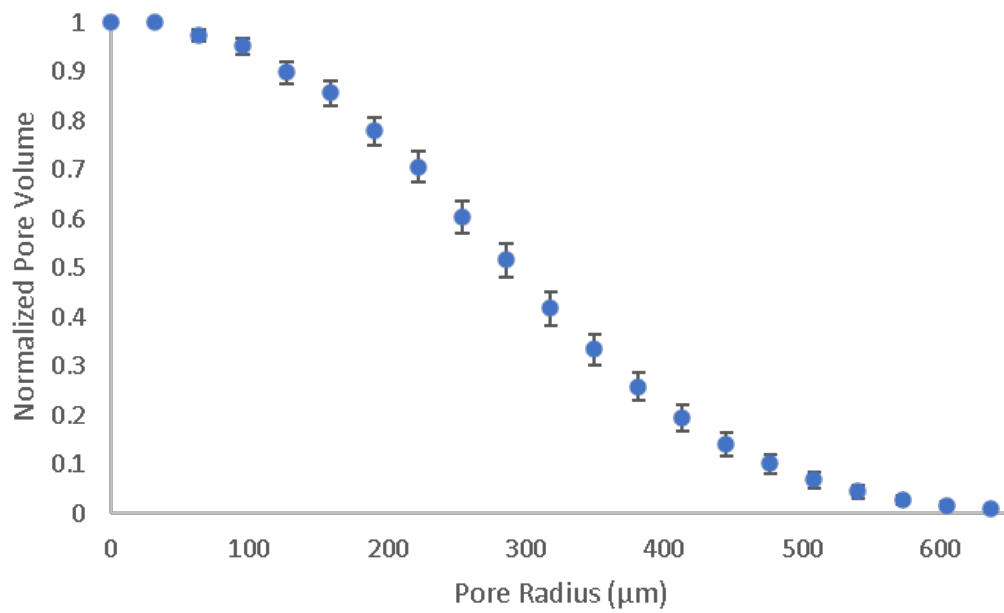


**Figure 4.14**: 100 micron NPS series overall cumulative PSD

**Table 4.6**: Average pore and solid particle sizes for 200 micron and 100 micron NPS series grains

| NPS Series (micron) | Average pore D (micron) | Average solid particle D (micron) |
|:---:|:---:|:---:|
| 200 | 338.8 | 313.0 |
| 100 | 355.78 | 319.45 |

There are slight differences, but overall there is reasonable agreement between the 200 micron NPS UAH XCT data, high resolution ZEISS data, and SEM data (Table 4.7).

**Table 4.7**: Comparison of average pore sizes for 200 micron NPS series

| Method | $\bar{r}$ | $\sigma(micron)$ | resolution (micron) | $r_{50}$ |
|:---:|:---:|:---:|:---:|:---:|
| Bubble Point | 100 | – | – | 100 |
| UAH XCT PSD | 169 | 6.5 | 31.9 | 112 |
| ZEISS XCT | 156 | – | 18.4 | 100 |
| 40X SEM Line Lengths | 200 | 78.1 | 3.7 | – |
| 50X SEM Line Lengths | 169 | 56.5 | 3.0 | – |
| 80X SEM Line Lengths | 143 | 67.2 | 1.8 | – |
| 40X SEM PSD | 127 | – | 3.7 | 96 |
| 50X SEM PSD | 106 | – | 3.0 | 60 |
| 80X SEM PSD | 74 | – | 1.8 | 40 |

## 4.2 ATN Characterization Results

The ATN network theory algorithm that was developed for use in previous electrochemical applications was applied to the porous hybrid samples to generate networks and yield the transport coefficient ratios for the 200 micron NPS (Table 4.8)

and 100 micron NPS series (Table 4.9) grains (Figure 4.15). It is interesting to note that within the 200 micron samples the results remain fairly consistent, however in the 100 micron cases there are definitely a few outlier points. The overall coefficient ratio in the 100 micron cases tend to be surprisingly similar to those of the 200 micron cases. The porosities an average solid particle sizes in both sets are fairly similar as well, although the average pore diameter tended to be slightly higher in the 100 micron cases. These similar parameters could be due to the inability of the XCT system to resolve the smaller pores in the 100 micron cases.

**Table 4.8**: Transport coefficient ratio and porosity for 200 micron NPS series grains

| Grain Specimen | $\frac{\mu}{\mu_{eff}}$ | $\epsilon$ |
|:---:|:---:|:---:|
| 200-1 | 5.97 | 0.44 |
| 200-2 | 6.96 | 0.41 |
| 200-3 | 7.76 | 0.44 |
| 200-4 | 7.19 | 0.49 |
| 200-5 | 8.53 | 0.48 |
| 200-6 | 6.70 | 0.48 |
| 200-7 | 7.91 | 0.48 |
| 200-8 | 6.62 | 0.48 |
| 200-9 | 8.11 | 0.49 |
| 200-10 | 6.97 | 0.49 |

A sample vertex plot and ATN network rendering are displayed below (Figure 4.16). The vertex strength plots suggest the theory of dominant flow prevailing in the central region of the pores (Figure 4.17) and (Figure 4.18). These strengths are based on the number of branching connections that congregate at the vertex point.

**Table 4.9**: Transport coefficient ratio and porosity for 100 micron NPS series grains

| Grain Specimen | $\frac{\mu}{\mu_{eff}}$ | $\epsilon$ |
|:---:|:---:|:---:|
| 100-1 | 6.41 | 0.49 |
| 100-2 | 6.93 | 0.48 |
| 100-3 | 7.17 | 0.49 |
| 100-4 | 6.76 | 0.51 |
| 100-5 | 7.43 | 0.47 |
| 100-6 | 7.6 | 0.47 |
| 100-7 | 7.03 | 0.48 |
| 100-8 | 6.12 | 0.49 |
| 100-9 | 6.58 | 0.50 |
| 100-10 | 7.10 | 0.47 |

It would appear that in most cases as flow travels from the inlet inward that all paths converge to a few key junctions.
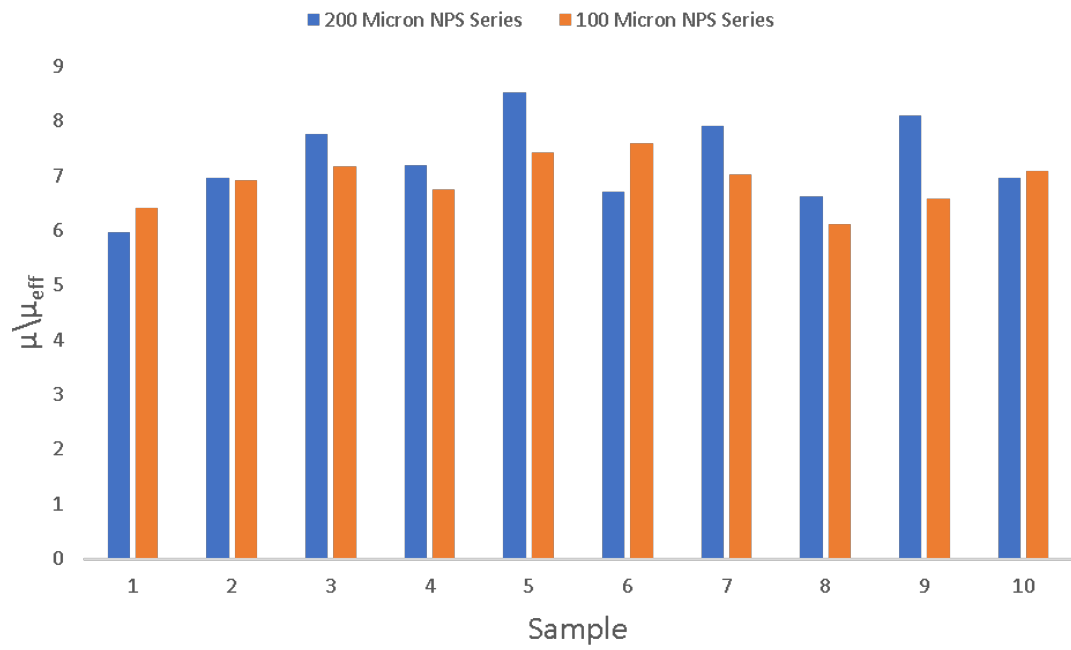
**Figure 4.15**: 200 micron NPS and 100 micron NPS Transport Coefficient Ratios
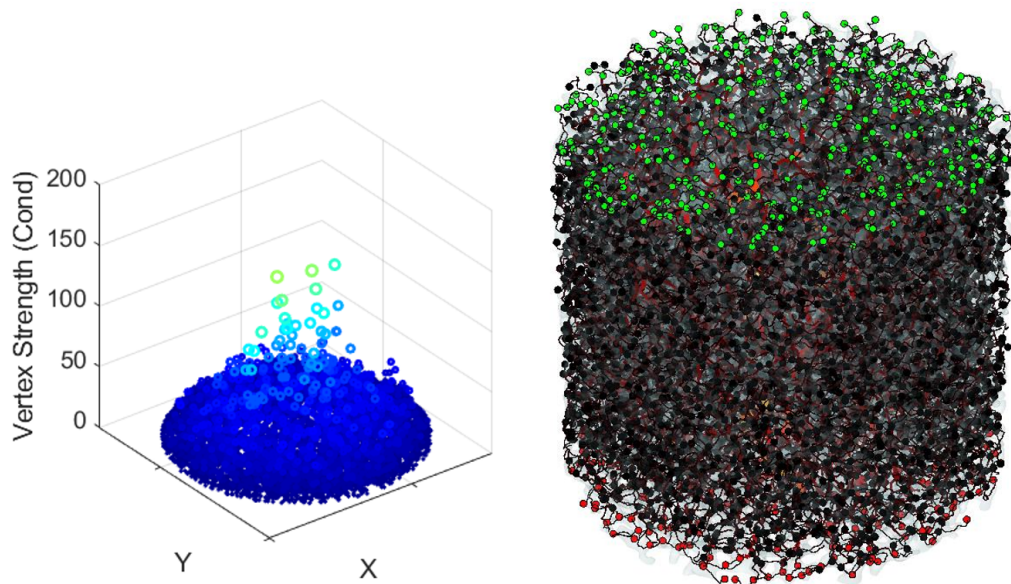


**Figure 4.16**: ATN Vertices and Network Plot
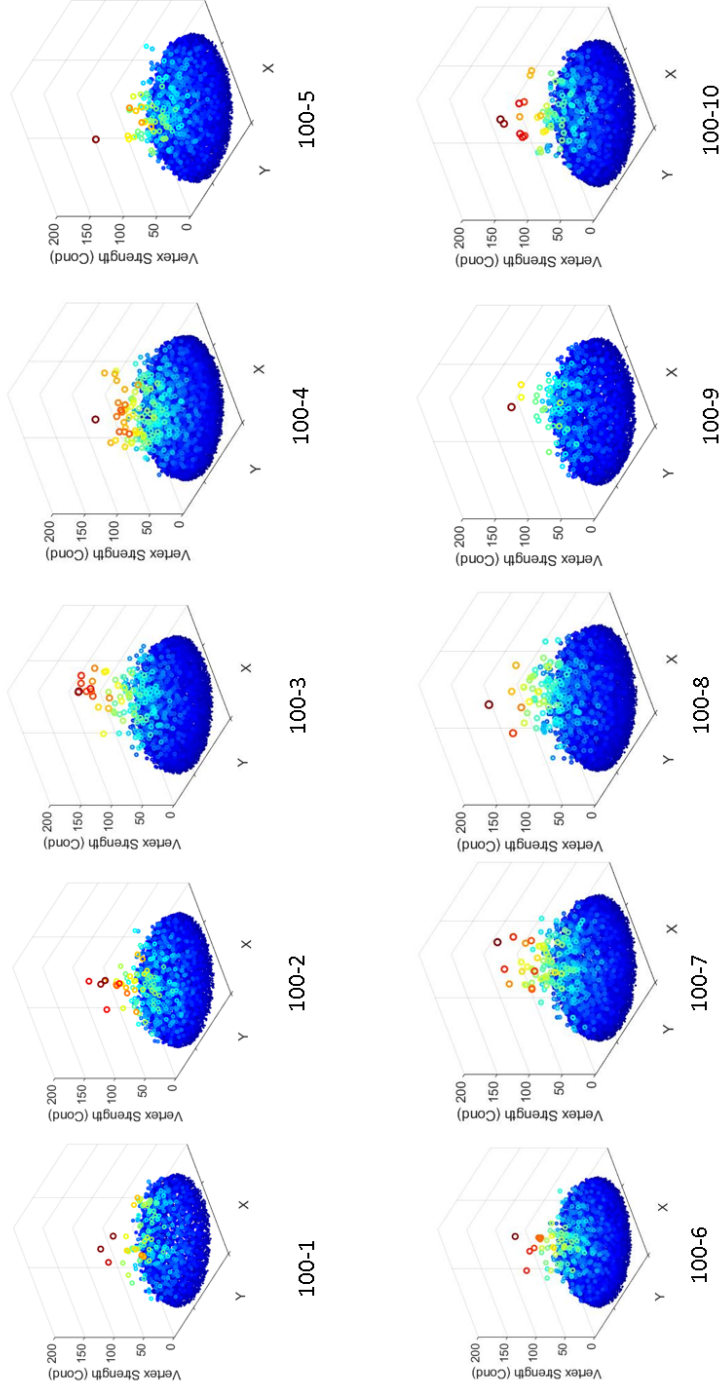
**Figure 4.17**: 100 micron NPS vertex strength
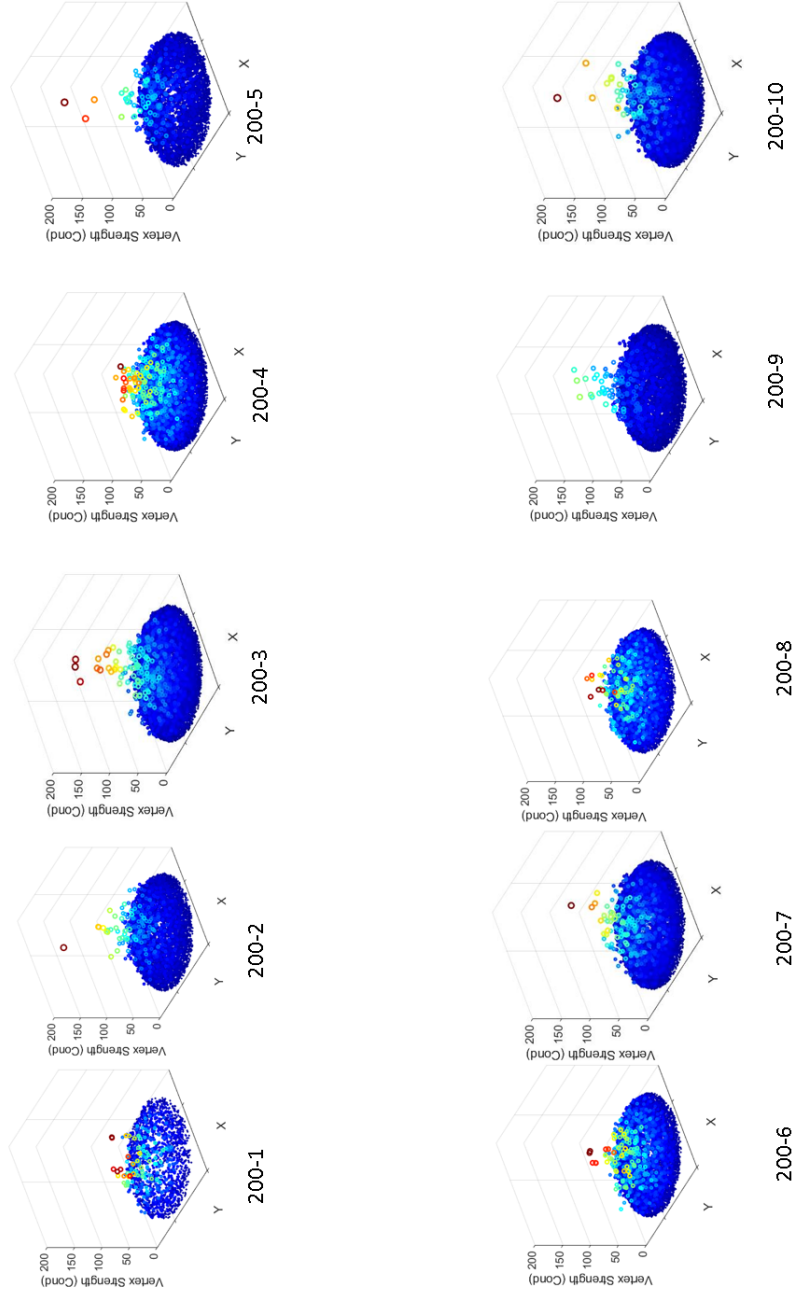
**Figure 4.18**: 200 micron NPS vertex strength

The probability distributions suggest that most vertices have a degree of 3 (Figure 4.19), while the vertex strength probability is around 0.25 for a strength less than 10 (Figure 4.20). This suggests that there is a large distribution of smaller junctions, but the high degree junctions toward the aft end of the grain tend to have significantly higher strengths.
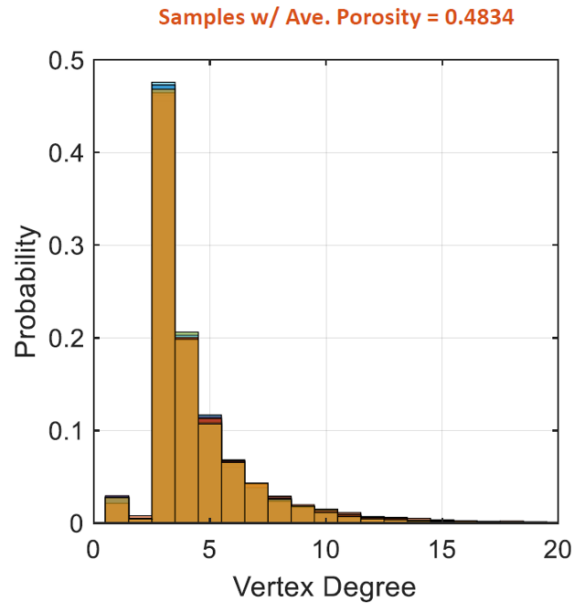


**Figure 4.19**: ATN Vertex Probability
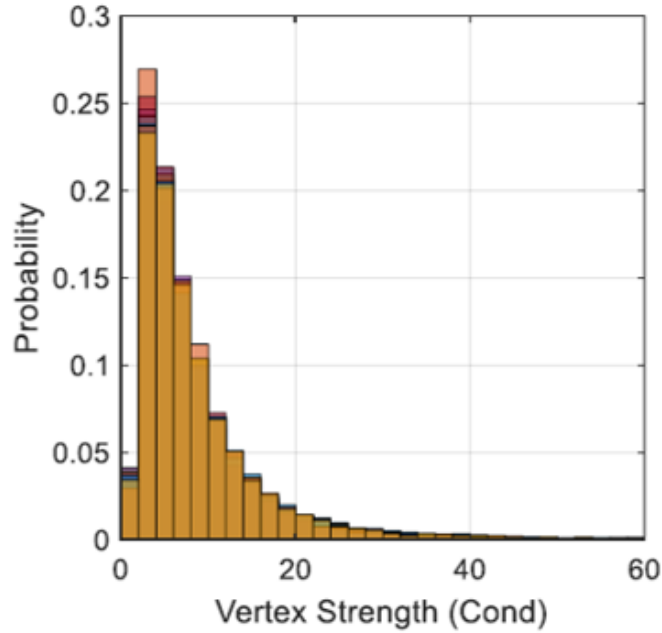
**Figure 4.20**: ATN Vertex Strength Probability Avg porosity=0.48

It appears that the trend of rapid computation times and relatively low memory usage from previous studies [5] were repeated in this case as well (Figure 4.21), (Figure 4.22), and (Figure 4.23). In all cases computation times were less than 20 minutes and memory usage was below 25 GB. It is interesting to note that the 100 micron NPS set appeared to be more resource intensive than the 200 micron set. The computational cost of electrochemical fin models has been noted to scale with the complexity (i.e. number of branches and nodes) of the given network [44]. It is possible more complex networks for the 100 micron grains result in increased computational burden.
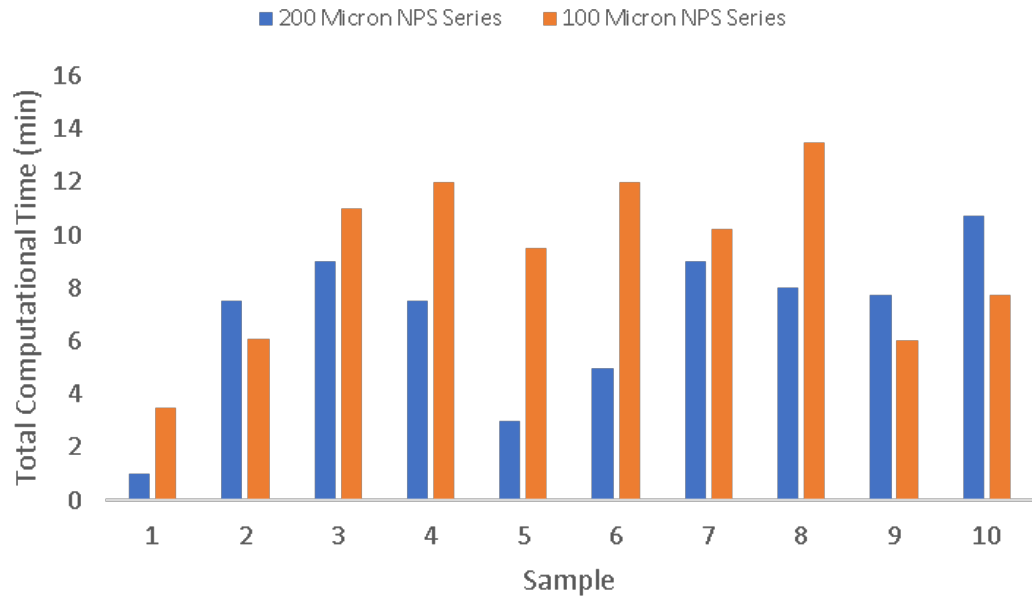
**Figure 4.21**: ATN Computation Times
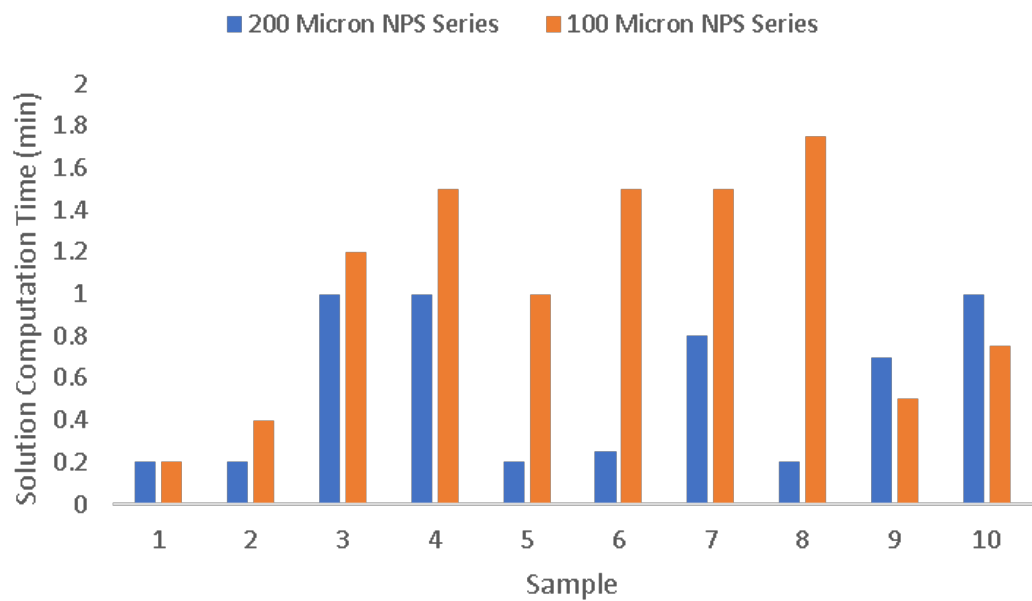


**Figure 4.22**: ATN Solution Computation Times
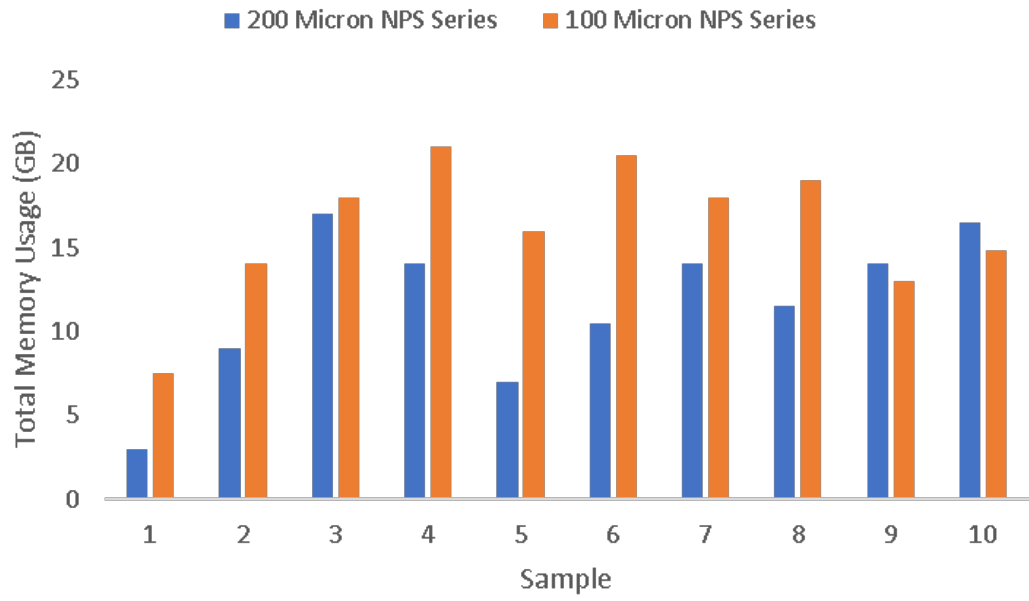
**Figure 4.23**: ATN Sample Memory Usage

# CHAPTER 5

# PRESSURE DROP MEASUREMENT AND ANALYSIS

*Great discoveries are made accidentally less often than the populace likes to think.*

—Wilhelm C. Roentgen

## 5.1 Overview

The pressure test conditions are used as inputs for the ATN network theory model previously described at the fore end of the grain. From the model, the predictions of transport ratio are used to convert a minimum resistance to an effective network resistance. This resistance is then used to determine an estimated pressure drop. The result is compared to experimental tests. The predictions of this model are compared to experimental results for validation. The effects of increasing Re number regarding pressure drop are examined.

## 5.2 Experimental Pressure Drop Results

Ten grains from the 200 micron set were tested. Three of these samples were used to find baseline test conditions, and seven were run at identical conditions with Re spanning from roughly 2000 to 20000. The 100 micron grains were run in the

same range, but all 10 samples were used at each set point. All 10 samples of both series were repeated with target venturi pressures between 10 and 650 psi resulting in a lower Re range of about 300-3000 (Figure 5.1).

Statistical analysis of the standard deviation in addition to the uncertainty of the pressure transducers was used to determine the range of potential error. This range encompasses a variation of $2\sigma$ for the measured values, or a 95 percent confidence interval. This interval would include the variations related to the pressure transducer uncertainty. The error bars denote the error/uncertainty defined by the equation below:

$$\xi = \frac{2\sqrt{\sigma^2 + u_{p1}^2 + u_{p2}^2}}{\sqrt{N}} \tag{5.1}$$

In this case, the value of N used is seven since the first 3 cases were used to better pinpoint target conditions. The relatively high error could be the result of an outlier point.

The experimental pressure drop results (Figure 5.1) are displayed and compared to the corresponding empirical correlation predictions (Figure 5.2). Once again, the empirical correlations severely overpredict the pressure drop. Modifying the porosity improves the agreement somewhat, but there is still a sizeable difference.

The first point is a zero point, hence the negative pressure drop is likely due to random uncertainty within the pressure measuring equipment in ambient conditions. Overall, excellent agreement between model predictions and actual experimental results is observed, with several points only differing by a few psi (Table 5.1) (Fig-

ure 5.3). It is interesting to note that a "critical point" is observed around an Re of 3000. Before this point, the model slightly over-predicts the pressure drop, and after starts to increasingly under-predict until re-converging at an Re near 20,000. An Re of 10 or less is generally accepted as the laminar flow region (Darcy's Law applies here), 10 to 2000 is accepted as transitional flow, and above 2000 is turbulent flow. It is possible that this crossover is a result of flow changing from transitional to fully turbulent, although this is difficult to say as a difference of 1-2 psi is within the margin of error for the measurement equipment as well as the overall sample error region.

**Table 5.1**: Individual Sample Pressure Drop Results for the 200 micron NPS series

| Re | $\dot{m}"$ | $\Delta P_{exp}$ | $\Delta P_{model}$ |
|---|---|---|---|
| 414.57 | 13.31 | -0.32 | 1.90 |
| 1798.47 | 57.71 | 15.37 | 17.32 |
| 2416.26 | 77.56 | 23.42 | 24.66 |
| 3050.80 | 97.97 | 31.84 | 32.15 |
| 5752.49 | 184.60 | 67.84 | 63.01 |
| 9628.54 | 309.01 | 117.74 | 107.27 |
| 13601.03 | 436.52 | 166.91 | 153.38 |
| 16209.67 | 520.21 | 199.43 | 183.93 |
| 18561.90 | 596.07 | 228.28 | 213.04 |
| 19992.85 | 651.19 | 244.20 | 245.22 |
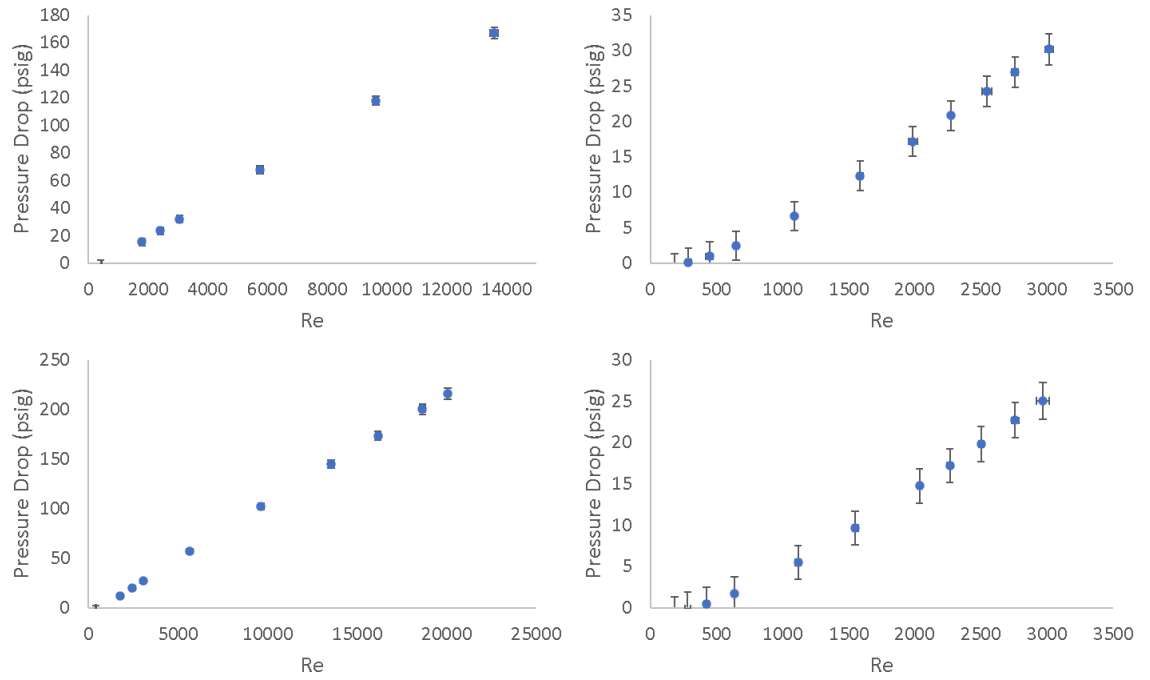
**Figure 5.1**: Pressure Drop Results of 200 micron NPS 2000<Re <16000 (Top Left), 200 micron NPS 200<Re<3500 (Top Right), 100 micron NPS 2000<Re<16000 (Bottom Left), and 100 micron NPS 200<Re<3500 (Bottom Right)
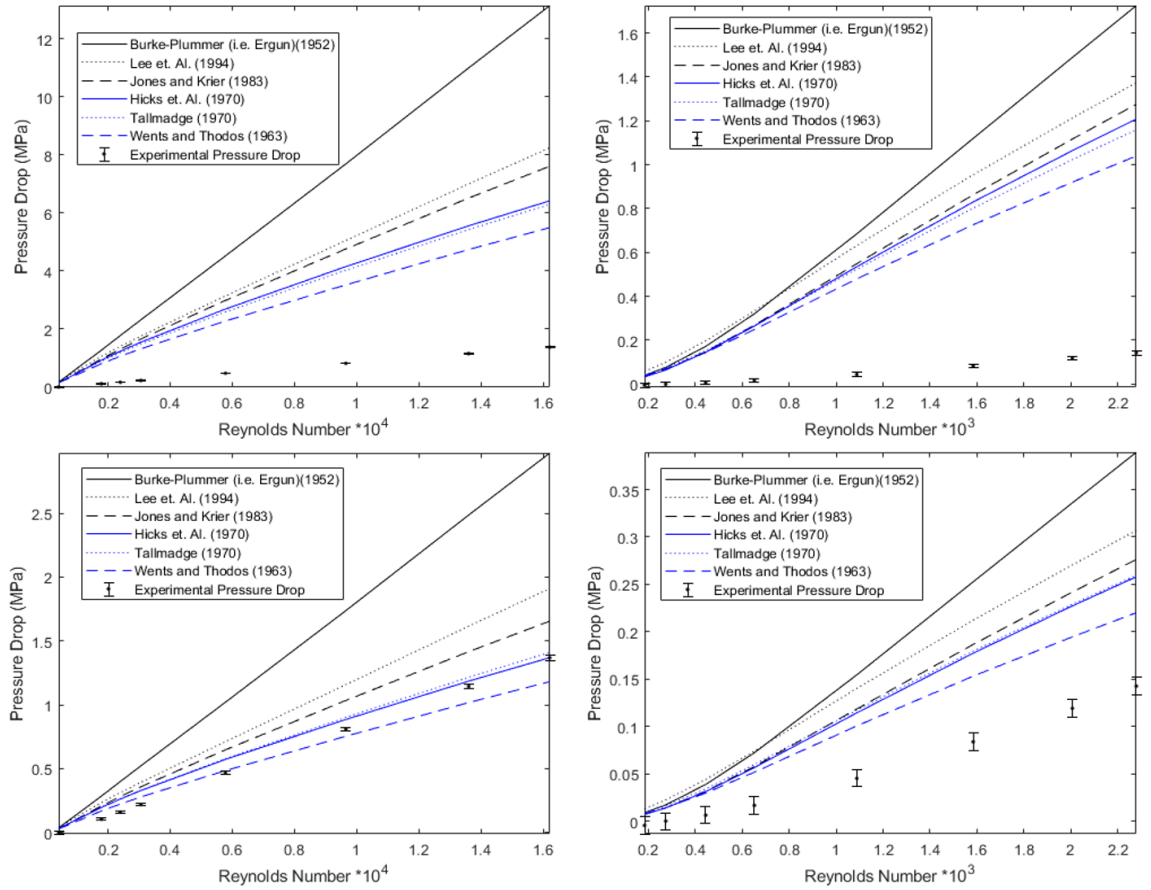
**Figure 5.2**: Pressure Drop Results compared to established correlations for 200 micron NPS 2000<Re <16000 (Top Left), 200 micron NPS 200<Re<3500 (Top Right), 200 micron NPS 2000<Re<16000 with correlation $\epsilon$=0.61 (Bottom Left), and 200 micron NPS 200<Re<3500 $\epsilon$=0.61 (Bottom Right)
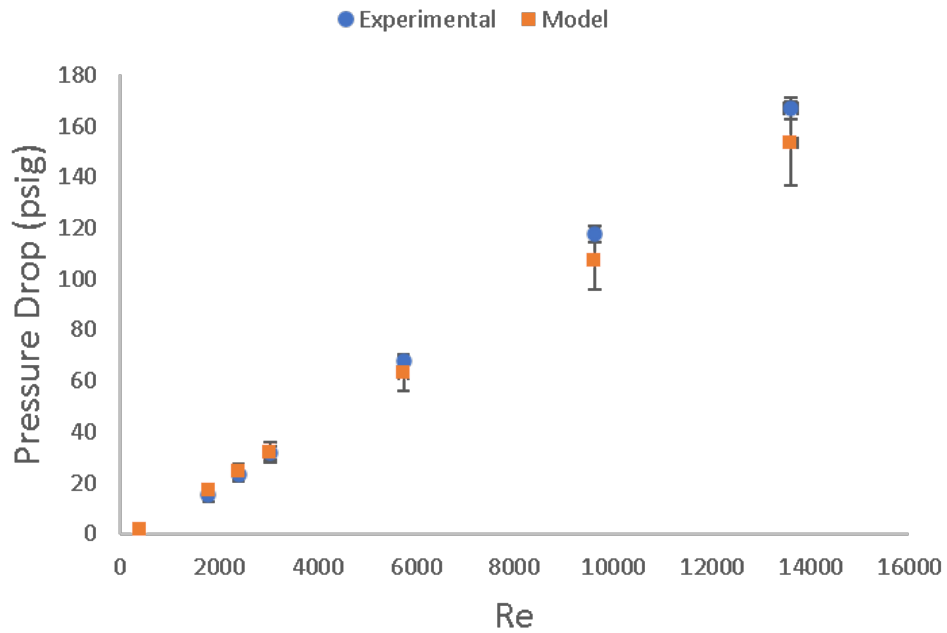
**Figure 5.3**: Average sample pressure drop test results compared to ATN model for the 200 micron NPS grains

In the 200 micron tests at lower Re, very good agreement is encountered again (Table 5.2) (Figure 5.4). In fact, it appears to be slightly better than the predictions at high Re. However, it is important to note that the measured pressure drops below Re=1000 lie within the $\pm$ 4 psig measurement uncertainty range of the pressure transducers (the upstream transducer with an uncertainty of 3 psig, and the downstream with that of 1 psig for a worse case scenario of 4 psig) combined with the random uncertainty, and therefore may be affected by random instrumentation factors. Once again, the first data point is at ambient conditions resulting in a negative experimental pressure drop that is likely due to pressure transducer measurement uncertainty. It is interesting to note that the "critical point" behavior of the sample is encountered

again in these tests, in which the model switches from over- to under-predicting the experimental pressure drop. The degree to which the model over-predicts in the less than Re of 3000 region seems to be fairly consistent, by only 2 psi or less. The overall error range for $\delta P$ in the model case appears to grow as Re increases. This could be due to the fact that at higher Re, the sample size decreased, and the effect of outlier points had a more substantial effect on the overall uncertainty.

Table 5.2: Individual Sample Pressure Drop Results for the 200 micron NPS series (Low Re)

| Re | $\dot{m}$" | $\Delta P_{exp}$ | $\Delta P_{model}$ |
|---|---|---|---|
| 183.33 | 5.85 | -0.65 | 0.35 |
| 288.89 | 9.22 | 0.07 | 0.84 |
| 448.25 | 14.32 | 0.95 | 1.93 |
| 649.28 | 20.72 | 2.41 | 3.67 |
| 1088.45 | 34.72 | 6.62 | 8.27 |
| 1587.10 | 50.62 | 12.30 | 13.87 |
| 1984.20 | 63.30 | 17.16 | 18.36 |
| 2274.57 | 72.56 | 20.80 | 21.59 |
| 2544.42 | 81.20 | 24.23 | 24.64 |
| 2759.21 | 88.02 | 26.95 | 26.91 |
| 3014.14 | 96.20 | 30.18 | 29.73 |
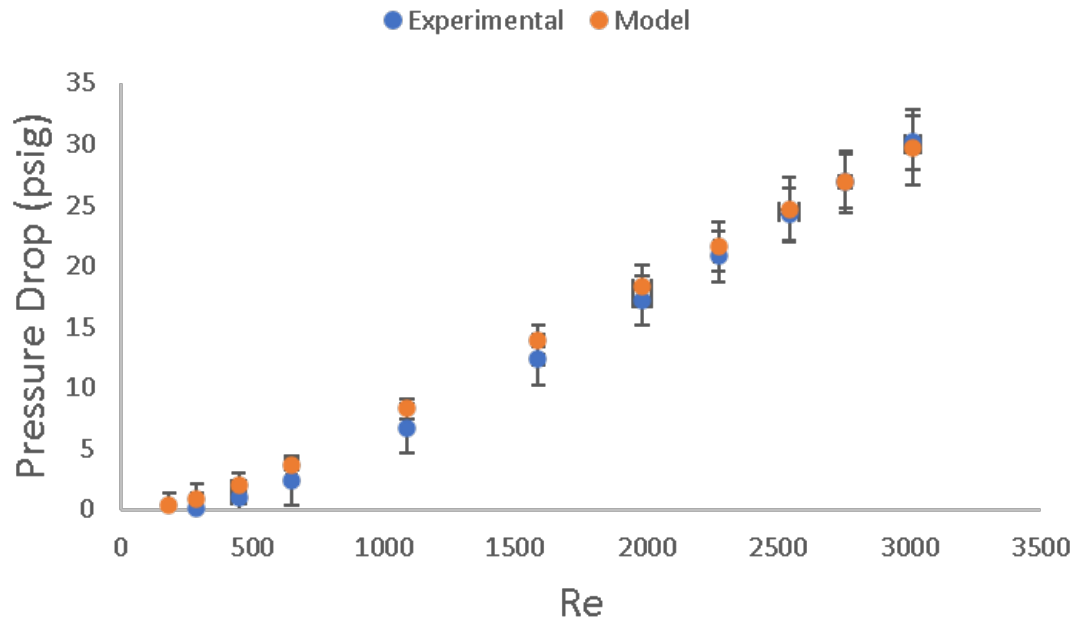
**Figure 5.4**: Average sample pressure drop test results compared to ATN model for the 200 micron NPS grains at low Reynolds number

The tests were repeated for the same conditions for the 100 micron grains as well (Table 5.3) and (Figure 5.5). Each data point is the average result of all ten samples. The same trends in agreement between the ATN model and experimental results are encountered. The same "critical point" phenomena is observed, and the same uncertainty growth is noted. Although the same Re values resulted, the pressure drops encountered were slightly lower. However, the difference is still within the margin of error. If there truly is an explanation outside of random uncertainty for the decreased pressure drop it seems counter-intuitive, as one would expect smaller pores to result in greater overall pressure drop due to increased friction from greater constriction. One possible explanation for this is that although the overall pore size

average is smaller, the local pore size in the central region remains constant or even slightly increases. If central flow is dominant and has a greater overall effect on the pressure drop, the smaller pore characteristics in the peripheral region may have little impact.

**Table 5.3**: Individual Sample Pressure Drop Results for the 100 micron NPS series

| Re | $\dot{m}"$ | $\Delta P_{exp}$ | $\Delta P_{model}$ |
|---|---|---|---|
| 412.11 | 12.09 | -0.09 | 1.38 |
| 1753.51 | 50.90 | 12.12 | 13.70 |
| 2453.32 | 71.15 | 19.93 | 20.72 |
| 3054.18 | 90.20 | 26.85 | 26.68 |
| 5653.63 | 166.92 | 57.12 | 52.07 |
| 9644.21 | 283.15 | 102.25 | 90.30 |
| 13551.44 | 399.10 | 144.80 | 127.82 |
| 16174.20 | 474.98 | 173.28 | 153.32 |
| 18655.61 | 549.88 | 200.45 | 177.98 |
| 20066.07 | 589.27 | 215.98 | 192.18 |
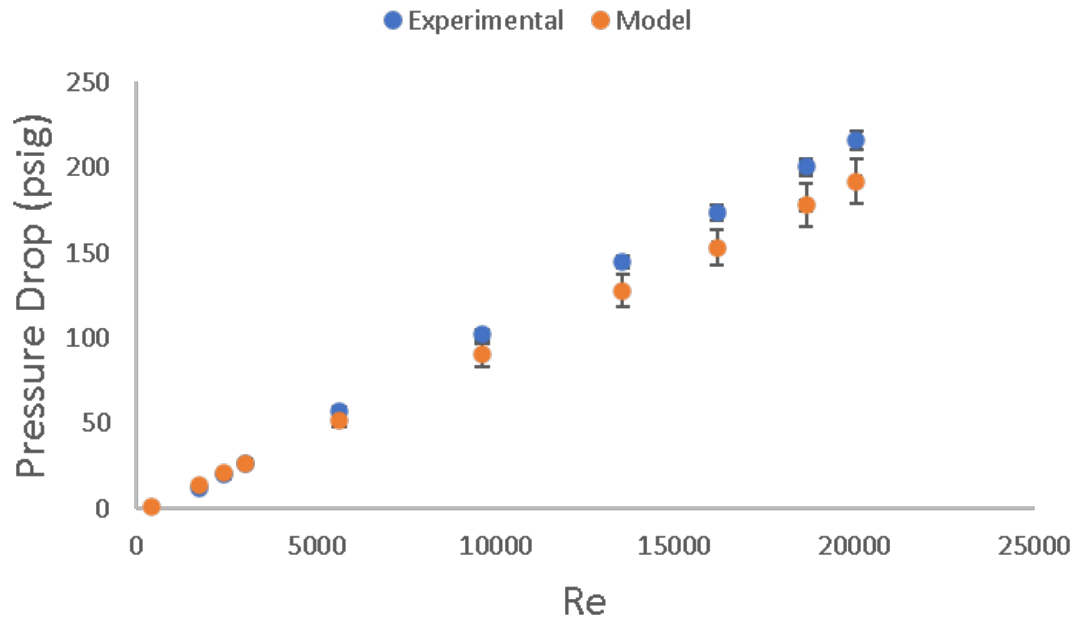
**Figure 5.5**: Average sample pressure drop test results compared to ATN model for the 100 micron NPS grains

These results were again repeated for the low Re cases for the 100 micron NPS grains (Table 5.4) and (Figure 5.6). In this case, behavior was fairly similar to the 200 micron low Re case, with the exception of the overall pressure drop being slightly less. Once again, pressure drop measurements below Re=1000 within regions in which uncertainty can be significant, and therefore may be influenced by random instrumentation fluctuation. The model over-prediction also tends to slightly expand from the first few points, and then contract until converging at the Re of 3000.

**Table 5.4**: Individual Sample Pressure Drop Results for the 100 micron NPS series (low Re)

| Re | $\dot{m}$" | $\Delta P_{exp}$ | $\Delta P_{model}$ |
|---|---|---|---|
| 183.37 | 5.39 | -0.67 | 0.28 |
| 282.89 | 8.60 | -0.12 | 0.65 |
| 424.44 | 12.47 | 0.47 | 1.40 |
| 637.34 | 18.83 | 1.69 | 2.92 |
| 1117.29 | 32.78 | 5.49 | 7.31 |
| 1549.15 | 45.68 | 9.63 | 11.69 |
| 2035.19 | 59.88 | 14.73 | 16.64 |
| 2264.98 | 66.50 | 17.21 | 18.96 |
| 2501.57 | 73.44 | 19.82 | 21.35 |
| 2758.23 | 81.60 | 22.67 | 23.92 |
| 2967.73 | 86.44 | 25.02 | 25.96 |
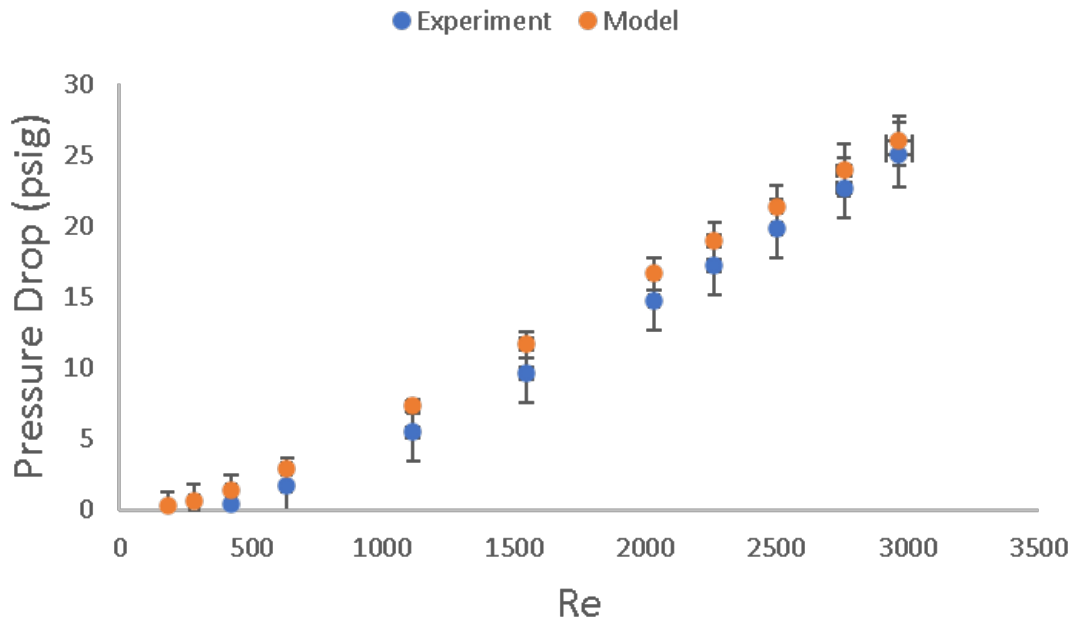


**Figure 5.6**: Average sample pressure drop test results compared to ATN model for the 100 micron NPS grains at low Reynolds number

Finally, the ATN model results are compared to the experimental test results alongside the empirical correlation predictions (Figure 5.7). In this figure it is very obvious that the model provides a significant improvement in capturing realistic pressure drops in these scenarios. In addition of a tendency of the correlations to significantly over-predict the pressure drops, there is also a wide spread of predictions among the individual correlations themselves. These results suggest that the ATN model has done a significantly better job of predicting the actual pressure drop, likely due to its ability to better account for non-homogeneous structures within the porous hybrid grains.
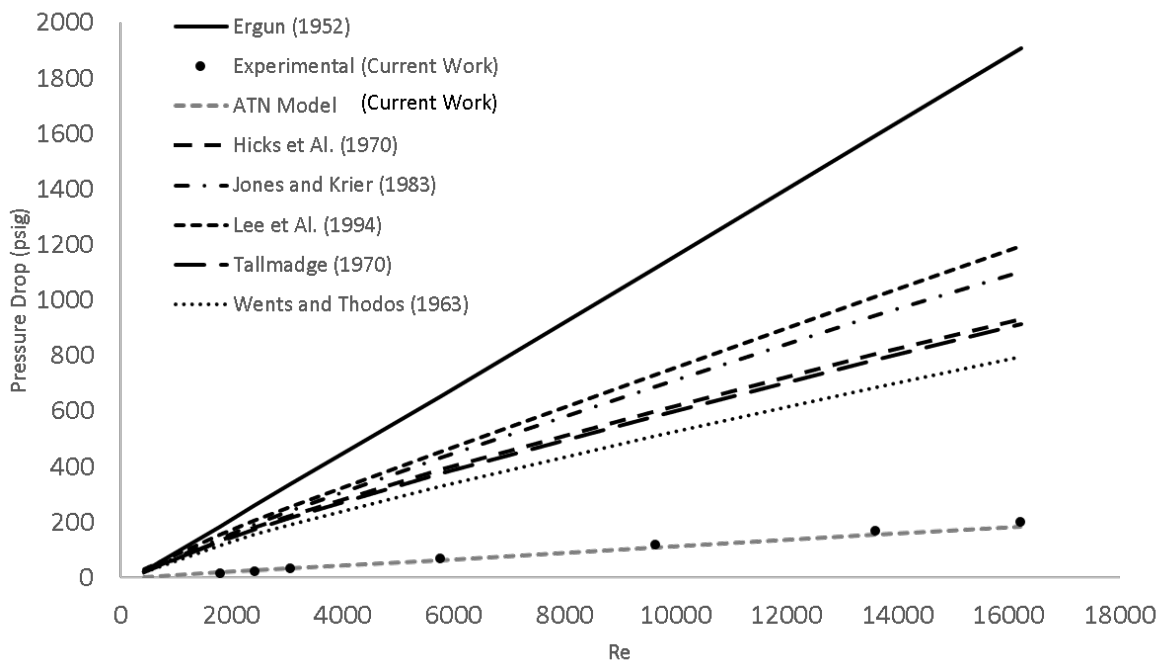


**Figure 5.7**: ATN model prediction of pressure drop compared to experimental results and correlation predictions

# CHAPTER 6

# CONCLUSIONS AND RECOMMENDATIONS

*No amount of experimentation can ever prove me right; a single experiment can prove me wrong.*

—Albert Einstein

## 6.1 Result Summary

A very substantial discrepancy between empirical correlation predictions of pressure drops in porous hybrid motor grains and actual measured pressure drops was observed in initial burn tests conducted [15]. In testing with nitrogen gas flow absent combustion, this phenomena was once again present.

XCT data of the porous hybrid grains was collected. This data was validated by comparison of determined porosity and average pore size values to measurements from Archimedes method tests, SEM image data, bubble point tests, and high-resolution XCT data using a separate tomographic imaging system. This data reveals that the porous hybrid motor grains have a non-homogeneous structure. While axially the grains have fairly consistent morphological properties, radially they are far more porous in the central region and more solid in the peripheral regions.

Observation of this functionally graded structure led to the theory that the more porous central region resulted in the flow properties within this region having a more pronounced effect on the overall pressure drop across the grains. To test this theory a parametric study was conducted in which the correlation porosities were adjusted to the value in these central regions. Improvement in pressure drop prediction was noted, although there still existed a fair degree of discrepancy both between experimental and correlation results, as well as predictions between the individual correlations. This persistent discrepancy suggests that the non-homogeneous geometry of the porous hybrid motor grains results in the inability of the correlations to accurately predict the pressure drop behavior for gaseous flow within the grains.

Computational models are often used in situations in which simplifying assumptions such as homogeneous structure are not applicable, but these models can be expensive both in terms of physical memory and computational time required to run the simulations. Analytical transport network, or ATN, theory, a heuristic model previously applied to electrochemical transport applications, was modified to apply to this physical gas transport scenario to provide a method of accounting for the non-homogeneous morphology of the grains to improve the prediction of pressure drops in a timely manner. The resulting model is based on XCT data, but may be applied to other 3-D datasets acquired by imaging methods or generated by computer aided engineering methods. The ATN approach breaks the porous region into a network of individual passages and nodes with effective resistances based on the tortuosity and varicosity of the passages. The overall network model is non-dimensionalized, and provides ratio-based properties that can be used from baseline cases to calculate a

representative pressure drop. The specific property of interest from this model is the gas transport coefficient ratio, $\frac{\mu}{\mu_o}$. By calculating a gas transport coefficient from the baseline case, the theoretically minimal resistance possible for this type of network, this ratio can be used to find a coefficient for the actual porous geometry in specific flow conditions to predict a pressure drop. In electrochemical theory, the baseline case is often an empty channel. In the case of fluid flow, this would correspond to empty pipe flow. A representative pipe flow case that resulted in accurate predictions was not observed. Instead, the Ergun equation was applied to a representative baseline homogeneous porous geometry in which the porosity was adjusted to 99% and the solid particle size was set to the x-ray camera pixel size, which reflects the scale of the minimum particle detectable by the x-ray system. In this case, very good predictions from the resulting ATN model were observed.

Results demonstrate that the ATN network theory model resulted in significant improvement in predicting pressure drops in the heterogeneous porous hybrid rocket motors compared to the empirical correlation counterparts. In many cases, model and experimental predictions differed by only 1 or 2 psi. At higher Re, this disagreement increased however. The uncertainty and error also increased noticeably, although these values still remained within acceptable ranges. At the Re of 3000, the model transitioned from over-predicting to under-predicting the pressure drop. This could be a result of the flow transitioning to fully turbulent. The over-prediction remained a fairly consistent value, but the under-prediction appeared to grow as Re increased.

## 6.2   Significance and Application

This model of pressure drop in porous media provides a mechanism to predict the pressure drop of fluid flows with reasonable accuracy in a computationally efficient manner. This has very significant benefit in applications involving more complex porous geometries that require rapid results.

In hybrid propulsion, this model now provides the means for not only better predicting the previously alluded to "optimal" porosity that would maximize total fuel in a given volume without incurring problematic pressure drops, it provides a way of evaluating individual porous passageway structure in terms of tortuosity and varicosity to determine optimal structure for evaluation. Specific grain geometries cannot be analyzed in a distinct or accurate manner using the current suite of experimental correlations, which assume homogenized structures. This application of course assumes that the motor is operated in true end-burning conditions.

There have been recent cases in which the flame has traveled into the porous network from the original outer burn surface. In this case, a reacting flow within the media would need to be accounted for. In companion works to their analysis of non-reacting flows, Cocco et al. have developed ATN models for reacting flow scenarios [23]. The favorable comparison of ATN predictions to experimental pressure drop results provided above suggests that extension to reacting flows is feasible.

In addition to porous hybrids, this method provides a way to estimate the pressure drop of porous flashback arrestors. In these devices it may be necessary to have locally highly constricted pores in order to quench flames in combustors. This

model could be used to predict the pressure drop of the injected fluid and once again optimize for minimal pressure drop while safely protecting the injector. It could also be used in filters and packed coolant beds to optimize pressure drop and cooling characteristics. In the latter case, extension of the ATN pressure drop approach to reacting flows may be needed.

With further development the approach above could be used in catalyst beds for monopropellant decomposition. It is important to note that this application is different from the others, as it involves chemical reactions occuring within the porous media, and would need to be modified accordingly. In these scenarios more tortuosity and varicosity could be used to increase the available surface area for reaction. However, these parameters would also increase the pressure drop of the flows within, which could be problematic if the pressure drop is too high.

## 6.3   Future Work Suggestions

In the future, it would be wise to further examine the baseline cases used for the ATN theory model. When a hollow pipe flow is used for the predicting case, the pressure drop appears to be too low resulting in an incorrect model prediction. However, when the Ergun equation is used with a very high porosity and solid particle size as small as the x-ray system can detect, an accurate base case is made. It would be interesting to create an ATN network from higher resolution data such as that from ZEISS in which a smaller particle size could be used in the baseline model. Additional post-processing would be required to ensure that only the connected pore

space is accounted for, as the ZEISS data was able to detect hollow spaces within the solid particles that would need to be filtered out.

The variation in accuracy in comparing the transition region data to turbulent Re data suggests that there are transitional effects that if incorporated into the model could result in improved predictions. Developing a method to modify the resistance term to account for varied flow conditions could be helpful. Widening the base of Re values to include the laminar flow region (Re less than 10) could be useful, and results could be compared to Darcy's Law.

The heterogeneous nature of the porous hybrid motor grains is the suspected cause of the empirical correlation inaccuracies. If this effort was repeated for homogeneous porous hybrid motor grains under similar conditions it is expected that the model and experimental results would more closely match the predictions from empirical correlations. Conducting this study would provide further validation of the ATN model and confirmation of this hypothesis.

In the inspiration for this work, Cocco [5] has a companion paper in which the electrochemical ATN model is applied to reacting flows [23]. In the same way, it is possible that the ATN model for pressure drop in these porous hybrid motor grains could be modified to account for internal reactions as well. This could be useful in addressing the previous applications of internally burning porous hybrid motor grains, dissolving coolant beds, and catalyst beds for decomposing monopropellants.

**APPENDICES**

# APPENDIX A

## PRESSURE DROP TEST SOP

*If I have seen further, it is by standing on the shoulders of giants.*

—Isaac Newton

UAH Propulsion Research Center

STANDARD OPERATING PROCEDURE FOR:

*Discharge Coefficient through Porous Media*

SOP #:           PRC – SOP – JRC-059

Rev.Ver.:        A.0

Operation:       Cold Flow Testing

Test Location:   PRC Spray Facility

Test Date:       _____

Test Time Start: _____     Finish: _____

**Test Team**

| NAME | ROLE |
|------|------|
|      |      |
|      |      |
|      |      |
|      |      |
|      |      |

## This Procedure Contains the following Hazards

|   |   |   |   |
|---|---|---|---|
|   | Human Subjects |   | Animal Subjects |
|   | Highly Toxic Chemicals |   | Toxins or toxin products |
| X | Pressurized gases |   | Explosives/Propellants |
|   | Microbial agents/products |   | Cell or tissue culture |
|   | Lasers |   | Selected Agents |
|   | Radioisotopes or x-ray generating equipment |   | Carcinogenic/mutagenic/teratogenic chemicals |
|   | Human blood, body fluid, tissue |   | Recombinant DNA/RNA molecules |
| X | COVID 19-Protocol |   |   |

## REVISION BLOCK

| VERSION # | DESCRIPTION OF CHANGES | DEVELOPMENT HOURS |
|---|---|---|
| **A.0** | **NEW SOP Based on SOP-SOP-JRC-032.A3** | **20** |
| | | |
| | | |

## ACTIVE WAIVERS

The following waivers have been reviewed by the procedure approval team and are accepted based on assessment of additional mitigations put into effect for conducting the test.

| # | DESCRIPTION | MITIGATION | EXPIRES | RESPONSIBILITY |
|---|---|---|---|---|
| 1. | In-Person CPR/AED training is currently inaccessible | Those with expired certifications are granted extensions for these provisional tests.  Those already certified will recertify online before the next revision of the SOP is approved | 1/1/2021 | David Lineberry |
| | | | | |

## PROCEDURE APPROVAL:

I have personally reviewed each of the operational steps of the SOP and have no questions that the operation can be performed safely and efficiently. I approve all red team personnel assigned in this document and verify that they have proper training to act in the prescribed test roles outlined in this procedure.

**Joseph Buckley:** _____  **Date:** 07/14/2020
**Author**

**George Nelson:** _____  **Date:** 07/14/2020
**PI**

**Mr. Tony Hall:** _____  **Date:** 07/15/2020
**Facility Engineer**

**Dr. David Lineberry:** _____  **Date:** 07/15/2020
**Laboratory Operations**

**Dr. Robert Frederick:** _____  **Date:** 07/15/2020
**PRC Director**

**Reviewed By:**
**UAH OEHS** _____  **Date:** _____

## AUTHORIZED RED TEAM MEMBERS

Individuals identified below are authorized to participate in test operations as *Red Team Members* through the SOP approval signatures.  By signing the document below, the individuals acknowledge that they have reviewed the procedure and understand the general and specific safety requirements, personnel limits, and work descriptions necessary to accomplish their part of the operation.

Additional Red Team Members may be added to this document without a procedure revision pending approval of the PRC Director prior to participating in the experiment.  Additional members require signatures of both the individual to be added and the approver.

Authorized test individuals agree to abide by and follow the procedure outlined in this document for conducting the described experiment.  Any individual not following procedure during testing in a manner which jeopardizes other test members will be immediately removed from the red team and reported to the PRC director.

| RED TEAM MEMBERS | AFFILIATION | REQUIRED TRAINING DATES | | | SIGNATURE |
| --- | --- | --- | --- | --- | --- |
| | | FIRST AID/ CPR-AED | PRC SAFETY TRAINING | UAH COVID 19 TRAINING | |
| Joe Buckley | GRA | 09/13/2018 | | 7/14/2020 | *Joseph Buckley* |
| Evan Unruh | GRA | 6/22/2018 | | | |
| James Venters | UGA | 09/13/2018 | | | *James Venters* |
| David Lineberry | PRC Staff | 05/26/2020 | | | *D. Lineberry* |
| Tony Hall | PRC Staff | 06/07/2019 | | | *Tony Hall* |
| | | | | | |

# SECTION II.  DECLARATIONS

### 7.  Objective

This SOP establishes procedures and defines safety precautions that are to be followed during a cold flow testing to establish the pressure drop resulting from gaseous flow through porous media.  The gas flow will be provided from either the Wind Tunnel High pressure air tanks or from gas cylinders connected to the supply inlet line of the Spray Facility feed system.  Pressure ratings for the system components are provided in Appendix E. Test conditions will not exceed the maximum allowable pressure for any system component without relief devices to protect the system.

### 8.  Test Location

Testing will be conducted in the PRC Spray Facility in High Bay 1 of the Johnson Research Center. A floor plan for the designated testing area for this facility is identified in Appendix D. Occupational limits of the area are limited to 4 individuals as identified in the *Code Yellow Shared Workspace Resumption Approval Form for On-Campus Research* form for the PRC Spray Facility.

### 9.  Roles and Responsibilities

This procedure requires 2 operators with the following responsibilities.

- Under COVID 19 Code Yellow Protocols, operator 1 will be assigned to operate the DAQ computer and verify completion of SOP steps.
- Operator 2 will be responsible for setting hardware in the system, adjusting regulator pressures, and assembling and disassembling hardware.

Additionally one of the two operators will be responsible for reading the Procedure during testing and ensuring all steps are followed.  If additional operators are participating in the testing, roles may be assigned as long as they are consistent with PRC COVID 19 Code Yellow Protocols.

### 10. Observer Policy

Observers may be allowed under this test procedure pending approval of the PRC Staff. Any observer must be briefed on the PRC COVID 19 protocols as well as experiment hazards, emergency procedures prior to test operations, and listed on the title page of the procedure. Observers from External Organizations must be included on the Spray Facility *Code Yellow Shared Workspace Resumption Approval Form for On-Campus Research* form

### 11. Safety Policy

All PRC test operations require a minimum of two operators with First Aid, CPR, and AED training.  Test operations are carried out according to the PRC Facility Usage Policy outlined in PRC-SOP-001-R01 and supplied in Appendix C.  All personnel involved with this operation are empowered to stop any portion of this operation at any time if they feel it is not proceeding in a

safe manner.  If a test is stopped for a safety matter, the project PI, The PRC Director, or PRC Research Staff will be notified of the concern and a decision on whether to continue the operation will be made at that time.  No safety interlock will be modified, bypassed, or defeated unless the test team has concurred and are aware of the inherent risks associated with the change. Otherwise, the offender may be permanently expelled from the PRC and all of its facilities.

## 12. Personal Protective Equipment (PPE)

Test personnel must wear safety glasses at all times during test operations.  Close toed shoes are required for testing.

PPE is augmented Under UAH Code Yellow Covid 19 Protocols, face masks are required at all times during testing as well as in all common areas of the JRC.  (*See Reference documentation*)

## 13. Procedure Deviations

During the execution of the SOP any deviation to the procedures outlined in this document should be noted on the procedure and it should be identified on the cover page that deviations were conducted. Revisions to the procedure may be required prior to the next test operation. Prior to each test, verify that the procedures do not require modification due to specific test plan requirements. In the event that redlines are required during execution, ensure that the redlines present no safety, efficiency, or environmental concerns.

## SECTION III. TEST PROCEDURES

### PRETEST PREPARATION

☐ 1     Confirm a JRC Staff Member is in the area to support Testing

☐ 2     Ensure all PPE, cleaners, and other supplies are available and room personnel limits are discussed

☐ 3     Sanitize applicable surfaces to include:

> (a) Control Cabinet work surface
>
> (b) Control Computer Keyboard and Mouse
>
> (c) Control Cabinet Switch panel

☐ 4     Verify the top part of the High-Pressure Spray Facility Chamber is secured or removed

☐ 5     Designate isolated safety glasses, gloves, walkie talkies, iPads, and other items normally shared to each individual accordingly to prevent cross-contamination.

☐ 6     Designate common touch items like keyboards and switch panels to one person.

☐ 7     If guests are present, provide a safety briefing to include

- Hazards specific to this operation: High Pressure, High Velocity Debris
- Emergency procedures
- Red Team only areas, see Appendix D
- PRC COVID 19 Protocols: Density Management, PPE, Sanitization Protocols

☐ 8     Ensure all personnel are wearing personal protective equipment (PPE).

☐ 9     Position belt barriers as portrayed on facility footprint (Appendix D)

☐ 10    Turn semaphore lights at facility entrance doors to red

### INSTRUMENTATION PREPARATION

☐ 11    Connect Instrumentation required for testing and record connections in Table 1

☐ 12    Turn on DAQ

☐ 13    Open LabView.

☐ 14    Start Test Specific vi and document vi file name

*.vi File Name:* _____ *.vi*

**Table 1  SYSTEM DAQ CONNECTIONS.**

| Name | Plug Ch | DAQ Ch | DAQ Card |
|------|---------|--------|----------|
| *System Press* | | | SCXI Slot 1 |
| *Venturi Press* | | | SCXI Slot 1 |
| *Inlet Press* | | | SCXI Slot 1 |
| *Gas Sim Dome press* | | | SCXI Slot 1 |
| *PhYDra Exit Press* | | | SCXI Slot 1 |
| *Exit Press* | | | SCXI Slot 1 |
| *Venturi Temp* | | | SCXI Slot 1 |
| *Inlet Temp* | | | SCXI Slot 1 |
| *PhYDra Exit Temp* | | | SCXI Slot 1 |

☐ 15    Verify nominal pressure readings of zero

☐ 16    Verify nominal thermocouple readings

## TEST ARTICLE SETUP

☐ 17    Install supply line to Porous Hybrid Pressure Drop Apparatus (PHyDrA)
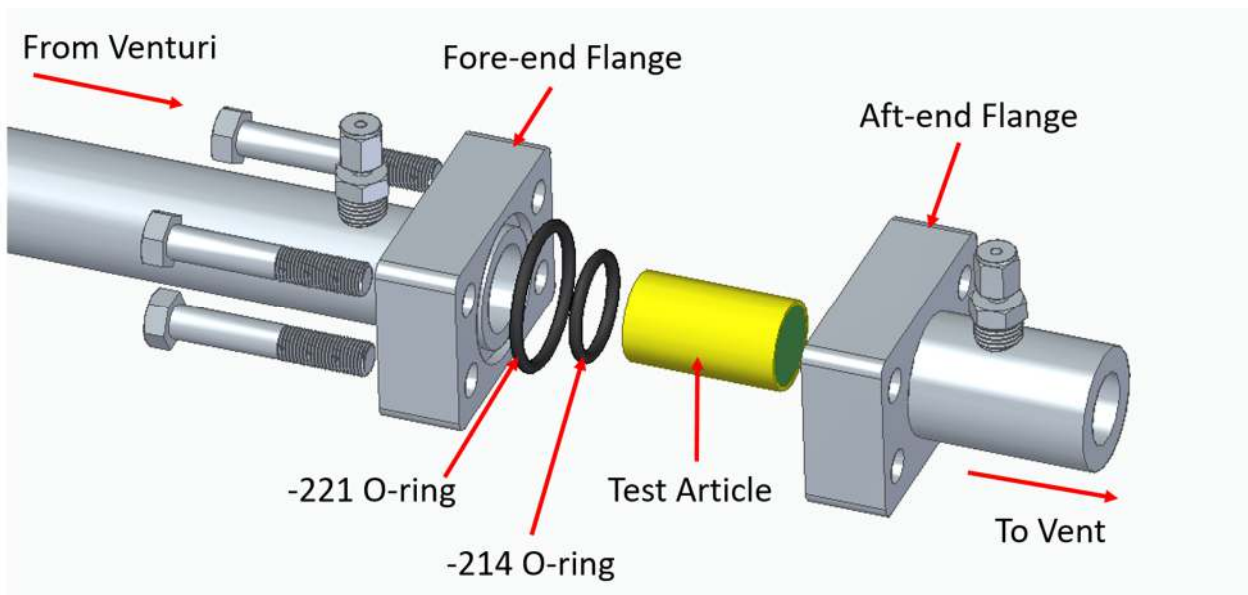


**Figure 1: PhyDra Assembly Exploded View**

☐ 18    Install Venturi Insert Upstream of PhyDra

☐ 19    Record Venturi Throat Diameter_____"

☐ 20    Attach Fore-end component of PHyDrA to venturi assembly

☐ 21    Apply a generous amount of high vacuum grease to a 214 O-ring

☐ 22    Place the 214 O-ring on the test article

☐ 23    Place test article in aft-end enclosure of PHyDra, pressing O-ring down until it fits within the triangular seal groove

☐ 24    Apply a generous amount of high vacuum grease to a 221 O-ring

☐ 25    Place 221 O-ring in face seal of fore-end flange of PHyDra fore-end component

☐ 26    Slide aft-end PHyDra enclosure flange with bolt holes aligned into contact with PHyDra fore-end enclosure, with test article sliding into central pocket of flange.

☐ 27    Attach Aft-end enclosure of PHyDra to Fore-end enclosure using threaded bolts with torque setting of 31 ft.-lbs. applied to wrench.

☐ 28    Connect additional run tube to aft end of PHyDra

☐ 29    Open Outside Access Garage Door

☐ 30    Attach exit line tube to run tube downstream of PHyDra Assembly

☐ 31    Install clamp block at end of vent line

☐ 32    Close outside access garage door to a height that does not interfere with vent line

☐ 33    Verify that all test components downstream of Gas Sim Run Valve are pressure-rated higher than Maximum Operating Pressure

☐ 34    Verify that all test hardware is secured to test stand apparatus

## PRESSURE SOURCE STARTUP

┌─────────────────────────────────────────────────────────────────┐
│                                                                   │
│                         **!!WARNING!!**                           │
│                                                                   │
│        **PRESSURIZED LINE HAZARDS ARE PRESENT IN SYSTEM.**        │
│                                                                   │
└─────────────────────────────────────────────────────────────────┘

☐ 35  Verify all dome hand ball valves (MDV-SF014, MDV-SF019, MDV-SF024, MDV-SF030) set to VENT (handle horizontal)

☐ 36  Verify all dome hand regulators at regulator panel are fully backed out (REG-SF011, REG-SF016, REG-SF021, REG-SF028) (CCW)

☐ 37  Verify PLC is powered on

☐ 38  Insert "Enable Key" and arm the Control Panel

☐ 39  Disengage "Emergency Stop"

☐ 40  Verify nominal Control Panel switch positions as per Table 2:

**Table 2: Nominal Control Panel Switch Positions**

| Switch | Valve Function | Switch Position |
|---|---|---|
| *Main System Pressurization* | Closed | Down |
| *Window/Curtain Run* | Closed | Down |
| *Liquid Sim Run* | Closed | Down |
| *Gas Sim Run* | Closed | Down |
| *Run Tank Pressure/Vent* | Vent | Down |
| *Main Vent* | Closed | Down |
| *Chamber Liquid Vent* | Closed | Down |
| *Chamber Gas Vent* | Closed | Down |

☐ 41  Engage "Emergency Stop"

☐ 42  Verify gas supply panel vent valve (NV-SF026) is closed

☐ 43  Set semaphore light at rear door to red

☐ 44  Open gas source by following the appropriate Steps Below

*Gas Cylinder Supply Source*

(a) Open Isolation Valves between Bottle valve and system

   (b) Crack open one bottle to let pressure slowly bleed into system

   (c) Once Pressure has equalized, Open all other k-bottles in supply manifold

  *Wind Tunnel Air Tanks*

   (a) Close Wind Tunnel Tank Vent Valve (NV-SF003)

   (b) Verify pressure of Wind Tunnel Air Tanks with gauge

   (c) Open Wind Tunnel Tank Isolation Manual Ball Valve (MBV-SF001)

☐ 45 Disengage the emergency stop.

☐ 46 Verify Operation of Main Vent Valve (PBV-SF006) by switching the valve to open, then closed (switch)

☐ 47 Verify Main Vent Valve (PBV-SF006) is closed (switch)

☐ 48 Open Main System Pressurization Valve (PBV-SF004) (switch)

☐ 49 Verify the pressure via the pressure transducer (PT-SF027) and the analog gauge (AG-SF008)

## VALVE ACTUATION CHECKOUT

☐ 50 Turn Valve actuation dome hand valve (MDV-SF030) to pressurize

☐ 51 Set Valve Actuation Supply hand regulator (REG-SF028) to 100 psig

☐ 52 Verify valve actuation from control panel by completing the following steps

   (a) Open "Chamber Liquid Vent" (PBV-SF058) (switch)

   (b) Close "Chamber Liquid Vent" (PBV-SF058) (switch)

   (c) Open "Chamber Gas Vent" (PBV-SF056) (switch)

   (d) Close "Chamber Gas Vent" (PBV-SF056) (switch)

   (e) Open Liquid Sim Run (PBV-SF052) (switch)

   (f) Close Liquid Sim Run (PBV-SF052) (switch)

   (g) Verify Run Tank Pressure/Vent (PDV-SF039) is vented (switch)

   (h) Verify Gas Sim Valve is closed (PBV-SF036)

## TEST ARTICLE LEAK CHECK PROCEDURE

☐ 53 Verify Gas Sim Dome (REG-SF021) is backed out

☐ 54 Connect a needle valve downstream of the test article

☐ 55    Verify that the needle valve downstream of test article is closed

☐ 56    Open Gas Sim run valve (PBV-SF034)

☐ 57    Set Gas Sim Dome hand regulator (REG-SF021) to pressurize test article

☐ 58    Close Gas Sim Run Valve (PBV-SF034)

☐ 59    Monitor test article pressure transducers to assess for leaks

☐ 60    Apply leak check agent as necessary to identify leak locations.

☐ 61    Open Gas Sim Run Valve (PBV-SF034)

☐ 62    Back out Gas Sim Dome hand regulator (REG-SF021)

☐ 63    Open manual valve downstream of test article to vent pressure

☐ 64    Close Gas Sim Run Valve (PBV-SF034)

☐ 65    Fix any present leaks

☐ 66    Return to Step ☐ 55 and repeat process as necessary to seal all leaks

☐ 67    Remove manual valve downstream of test article

## PRESSURE DROP TEST

☐ 68    Close Run-Tank isolation hand ball valve (MBV-SF039)

☐ 69    Fully back out Gas Sim Dome hand regulator (REG-SF021)

☐ 70    Open Gas Sim Run Valve (PBV-SF034)

☐ 71    Set desired pressure with Gas Sim Dome hand regulator (REG-SF021)

☐ 72    Collect data as appropriate

☐ 73    Repeat steps ☐ 71 to ☐ 72 until data at all desired pressure data points have been collected

☐ 74    Fully back out Gas Sim Dome hand regulator (REG-SF021)

☐ 75    When flow has ceased, Close Gas Sim run valve (PBV-SF034)

☐ 76    Replace test article with new test article if desired (see "TEST ARTICLE SETUP" section for assembly instructions"), store test article in appropriate location, and repeat steps 70 - ☐ 75 until all test articles for current series have been tested

## FACILITY DEPRESSURIZATION

☐ 77   Close Main System Pressurization Valve (PBV-SF004) (switch)

☐ 78   Inform personnel in the vicinity of venting, hearing protection optional

☐ 79   Open Main Vent (PBV-SF006)

☐ 80   Toggle the run tank Pressure/Vent Switch (PDV-SF039) between vent and pressurize to ensure the line is fully vented

☐ 81   Open the $N_2$ panel vent valve to depressurize the panel(NV-SF026)

☐ 82   Verify "System Pressure" is zero via LabView ( PT-SF027) and AG-SF008

☐ 83   Close Supply Isolation Valves

### *Gas Supply Source*

(a) Close all gas cylinder Valves

(b) Open Supply Line Manual Vent (NV-SF003)

(c) Once all pressure is vented Close Supply Line Manual Vent (NV-SF003)

(d) Close Bottle Pack Isolation Valves

### *Wind Tunnel Air Tanks*

(a) Close Wind Tunnel Tank Isolation Manual Ball Valve and lock the Valve (MBV-SF001)

(b) Open Supply Line Manual Vent (NV-SF003)

(c) Once all pressure is vented Close Supply Line Manual Vent (NV-SF003)

☐ 84   Turn off semaphore light at rear door

## **FACILITY SHUT DOWN**

- ☐ 85 Reengage "Emergency Stop"

- ☐ 86 Disarm Control Panel and remove "Enable Key"

- ☐ 87 Return all Control Panel switches to nominal positions as per Table 2

- ☐ 88 Return all dome hand valves (MDV-SF014, MDV-SF019, MDV-SF024, MDV-SF030) set to VENT (horizontal)

- ☐ 89 Fully Back out all hand regulators (REG-SF011, REG-SF016, REG-SF021, REG-SF028) (CCW)

- ☐ 90 Remove exit line tube and store

- ☐ 91 Close outside access garage door

- ☐ 92 Turn off semaphore lights at entrance doors

- ☐ 93 Back up Method: __Save all data to external drive_____

- ☐ 94 Upon completion, the SOP needs to be signed by the participating Red Team Members and placed in secure location.

- ☐ 95 Document relevant information requested in the Shared Google Test Calendar

- ☐ 96 Sanitize worksurfaces and common touch items

APPENDIX A.     Cross Referenced Procedures


The following procedures are referenced in this SOP and are required for verification purposes.


| # | SOP Doc # | Description |
|---|---|---|
| 1 | | UAH PRC Safety Program, 22-Feb-2013. |
| 2 | PRC-SOP-001 | UAH Propulsion Research Center – Facility Usage Policy, 1-Apr-2012. |
| 3 | PRC-SOP-002 | PRC 2017 Safety Plan |
| 4 | | *Operational Protocols at the University of Alabama in Huntsville (UAH) for Modified Limited Research Operations During COVID-19 Pandemic*, May 18, 2020 and Subsequent Revisions |
| 5 | | *Code Yellow – Shared Workspace Resumption Approval Form for On-Campus Research – JRC 165 Spray Facility*, Rev01 and subsequent Revisions |
| 6 | | |

## APPENDIX B. RISK ASSESSMENT

| Frequency of Occurrence | Hazard Categories | | | |
|---|---|---|---|---|
| | 1 Catastrophic | 2 Critical | 3 Serious | 4 Minor |
| (A) Frequent | 1A | 2A | 3A | 4A |
| (B) Probable | 1B | 2B | 3B | 4B |
| (C) Occasional | 1C | 2C | 3C | 4C |
| (D) Remote | 1D | 2D | 3D | 4D |
| (E) Improbable | 1E | 2E | 3E | 4E |

XX Unacceptable    XX Acceptable for Remote Operations    XX Acceptable for Remote/Attended Operations    XX Acceptable for Attended Operations with Approval

| Implementation Criteria | | |
|---|---|---|
| Hazard Categories | Remote | Attended |
| 1A, 1B, 1C, 2A, 2B, 3A | Implement immediately | Implement immediately |
| 1D, 2C, 2D, 3B, 3C | Implementation should be seriously considered | Implement as soon as possible |
| 1E, 2E, 3D, 3E, 4A, 4B | Implementation should be seriously considered | Implementation should be seriously considered |
| 4C, 4D, 4E | Consideration should be given | Consideration should be given |

| Frequency Definitions | | |
|---|---|---|
| Description | Category | Mishap Definition |
| Frequent | A | Likely to occcur frequently |
| Probable | B | Will occur several times in life of an item |
| Occasional | C | Likely to occur sometime in life of an item |
| Remote | D | Unlikely but possible to occur in life of an item |
| Improbable | E | So unlikely, it can be assumed occurrence may not be experienced |

| Category Definitions | | |
|---|---|---|
| Description | Category | Mishap Definition |
| Catastrophic | 1 | Death or system loss |
| Critical | 2 | Severe injury, severe occupational illness, or major system damage |
| Serious | 3 | Injury requrieing medical attention, illness, or system damage |
| Minor | 4 | Possible minor injury, or minor system damage |

**Item** #: (number and letter) the number indicates the failure mode and the letter indicates a unique Cause for that failure mode. Each failure mode is a unique number and each cause is a unique letter

**Failure Mode**: Specific action that is a hazard (Inadvertent Ignition, Spill, over pressurization, etc.)

**Failure Cause:** Causes of the failure modes (plugged nozzle, electrostatic discharge, etc.)

**Potential Effects:** Effect on personnel safety or equipment. Potential harm to personnel or damage to equipment.

**Haz Cat:** Initial hazard ranking of the hazard without any safeguards in place (From Table above)

**Safeguards:** Equipment, specifications, safety by design. Controls, Design, Procedures in place to prevent the Failure cause.

**HazCat:** Hazard ranking after Safeguards are in place (should be lower)

**Verifications:** Mitigating Solution

| ITEM # | FAILURE MODE | FAILURE CAUSE | POTENTIAL EFFECTS | HAZ CAT | SAFEGUARDS | HAZ CAT | VERIFICATION |
|---|---|---|---|---|---|---|---|
| 1a | Over Pressurization | Sytem Component Failure | Failure of pressurized lines<br>Delay of testing<br>Personel injury<br>Test article failure resulting in projectile debris | 2C | • Pressure lines are secured<br>• Secured area<br>• Max system pressure is 2500 psi, with all components rated to withstand at least this pressure<br>• Burst disks and relief valves on run tank and test facility<br>• Buddy system | 2D | |
| 2a | Slick Floors/Falling Slipping Hazard | Water spilled during filling tank or article | Personnel Injury Slipping | 4C | • Overfill Container used to prevent spillage from tank fill | 4D | Clean up spill immediately |
| 2b | | Leaky System Components | | | • System is Leak Checked prior to Testing | | |
| 3 | Projectile Debris | Test Article Failure | Personel injury<br>System Damage<br>Delay of testing | 2C | • Atmospheric Vent line<br>• Secured area<br>• Non-linear exit path (dissipate projectile energy) | 3C | |
| | | | | | | | |

| 4 | High Amplitude Acoustic | Direct Exposure to Acoustic Source | Hearing Damage | 3C | Hearing Protection | 3D | Shut down experiment<br><br>Seek Medical Attention<br><br>Report Injuries |
|---|---|---|---|---|---|---|---|
| 5 | Electrical Shock | High Voltage Lines in contact with water | Burns<br><br>Electrocution<br><br>Equipment Damage | 3C | Ensure all Electrical cords, plugs, and receptacles are clear of floor and wetted surfaces<br><br>Cover electrical components at risk of becoming wet<br><br>Use of proper PPE<br><br>CPR/AED Training for Red Team | 3D | Shut down experiment<br><br>Seek Medical Attention<br><br>Report Injuries |

*Additional COVID 19 Job Hazard Analysis provided in Reference Document (Appendix A)*

## APPENDIX C. UAH PRC FACILITY USAGE POLICY

# UAH
## The University of Alabama in Huntsville

*Propulsion Research Center*

S225 Technology Hall
Huntsville, Alabama 35899
Phone: (256) 824-7200
Fax: (256) 824-7205

**UAH Propulsion Research Center - Facility Usage Policy – April 1, 2012**

The Propulsion Research Center (PRC) conducts research, produces publications, and mentors students in advanced propulsion technologies and their applications. The PRC connects the academic research community and propulsion community through interdisciplinary collaboration. Use of the facility requires prior written approval of the PRC Director.

The Propulsion Research Center laboratories were established to provide UAHuntsville faculty, staff, and students, state-of-the-art facilities for conducting basic and applied research on propulsion systems and related sciences. The PRC was established to provide students a "hands-on" education in propulsion. The facilities may be used for sponsored research projects, PRC staff and Graduate Student research projects, and approved UAHuntsville undergraduate research projects. The Propulsion Research Center acknowledges that hazards are inherent to the nature of the research conducted in the facilities that require strict adherence to facility rules and protocols for anyone engaged in research in the PRC laboratories. PRC facility protocol is as follows:

1. All PRC Test operations are under the authority of the PRC Director and UAH campus safety practices.
2. All personnel involved in testing are UAH employees, UAH students under PRC supervision, customers with an active contract with UAH, or those with other formal arrangements agreed to in writing by the University.
3. All tests involving pressures over 100 psi, high voltage, combustion, or other sources of possibly injury require a Standard Operating Procedure (SOP), reviewed and signed by the test Red Team (see below), and approved by the PRC Director.
4. The tests are conducted by a designated Red Team who has at least one UAH staff member and has at least two members who are Red Cross Safety and CPR/AED Certified.
5. After any major test anomaly, all PRC test operations are automatically suspended until a determination of the basic cause of the incident is determined and all active SOPs are reviewed in light of the findings of the incident before resuming testing. A verbal report of the incident will be given to the V.P. of Research and a representative of Campus Safety within 24 hours of the incident.

*Robert A Frederick*
_____     4/1/2012

Robert Frederick
Interim Director PRC

APPENDIX D.    Spray Facility Floor Plan
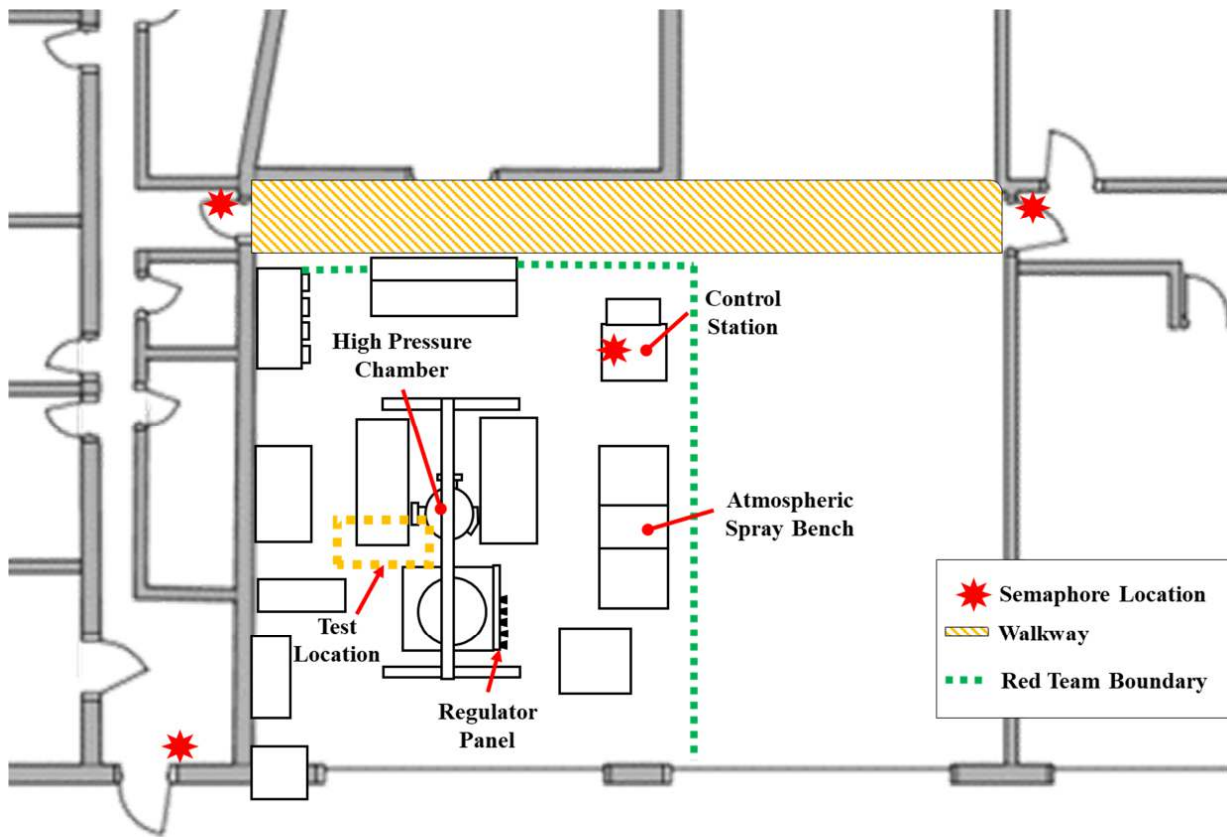
## APPENDIX E.     UAH Spray Facility Component Pressure Ratings

| Labels | No. | Component | Description | Manufacturer | Model |
|---|---|---|---|---|---|
| AG-SF002 | | Analog Gauge | 1/4" NPT; 0-3000 Psi | Ashcroft | 4066K622 |
| MBV-SF001 | | Manual Ball Valve – Wind Tunnel Isolation | 1"; 4653 Psi | Swagelok | SS-AFSS16 |
| NV-SF003 | | Needle Valve - Vent | 1/2"; 5000 Psi | HAM-LET | H3000SSLR1/2M |
| A0-Tank-1 | 16.01 | Tank 1 - Bottom | 306.9 cu. Ft.; 2826 Psi | A.O. Smith Corp. | MV-50405-A33 |
| A0-Tank-2 | 16.02 | Tank 2 - Top | 306.9 cu. Ft.; 2826 Psi | A.O. Smith Corp. | MV-50405-A33 |
| PBV-SF004 | | Pneumatic Ball Valve - Main System Pressurization | 1"; 0-2500 Psi | Swagelok | |
| REG-SF005 | | Manual Pressure Regulator - Pneumatic Ball Valves | 1/4"; 0-250 Psi | Tescom | |
| AG-SF069 | | Analog Gauge | 1/4" NPT; 0-400 Psi | Marshall | 91173 |
| PBV-SF006 | | Pneumatic Ball Valve - Main Vent | 1/4"; 6000 Psi | Parker | 4F-B6LJ2-SSP |
| CV-SF007 | | Check Valve | 1"; 1/10 Psi | Swagelok | SS-16C-1 |
| AG-SF008 | | Analog Gauge - Feed Line | 0-4000 Psi | Helicold | |
| CV-SF009 | | Check Valve | Stainless Steel Poppet 4700 psig (323 bar) Check Valve, 1 in. Swagelok Tube Fitting, 1/3 psig (0.03 bar) | Swagelok | SS-CHS16-1/3 |
| CV-SF009 | | Check Valve | Stainless Steel Poppet 4700 psig (323 bar) Check Valve, 1 in. Swagelok Tube Fitting, 1/3 psig (0.03 bar) | Swagelok | SS-CHS16-1/3 |
| FILT-SF010 | | Filter | 1" NPT,1200 SCFM, 6000 Psi | Chase Filters | 51S-2416P-25SEV |
| REG-SF011 | | Manual Pressure Regulator - Run Tank Dome Loader | 0-2500 Psi | Tescom | 26-1064-24 |
| AG-SF012 | | Analog Gauge - Run Tank Dome Loader | 0-3000 Psi | Omega | |
| PT-SF013 | | Pressure Transducer - Run Tank Pressure/Vent Dome Loader | 0-3000 Psi | Honeywell | FPG1DN |
| MDV-SF014 | | 3-Way Manual Diverter Valve - Run tank dome hand valve | 1/4"; 4800 Psi | Hylok | H1B3S-H4TPC |
| DL-SF015 | | Dome Loader - Run Tank/Vent | 3/4"; 6000 Psi | Tescom | 26-1221-2121 |
| REG-SF016 | | Manual Pressure Regulator - Window/Curtain | 0-2500 Psi | Tescom | 26-1064-24 |
| AG-SF017 | | Analog Gauge - Window/Curtain | 0-3000 Psi | Omega | |
| PT-SF018 | | Pressure Transducer - Window/Curtain Dome Loader | 0-3000 Psi | Honeywell | FPG1DN |
| MDV-SF019 | | 3-Way Manual Diverter Valve - Window curtain dome hand valve | 1/4"; 4800 Psi | Hylok | H1B3S-H4TPC |
| DL-SF020 | | Dome Loader - Window/Curtain | 3/4"; 6000 Psi | Tescom | 26-1221-2121 |

| Labels | No. | Component | Description | Manufacturer | Model |
|---|---|---|---|---|---|
| REG-SF021 | | Manual Pressure Regulator - Gaseous Sim | 0-2500 Psi | Tescom | 26-1064-24 |
| AG-SF022 | | Analog Gauge - Gaseous | 0-3000 Psi | Omega | |
| PT-SF023 | | Pressure Transducer - Gaseous Sim Dome Loader | 0-3000 Psi | Honeywell | FPG1DN |
| MDV-SF024 | | 3-Way Manual Diverter Valve - Gas sim dome hand valve | 1/4"; 4800 Psi | Hylok | H1B3S-H4TPC |
| DL-SF025 | | Dome Loader - Gaseous Sim | 1/2"; 6000 Psi | Tescom | 26-1111-282 |
| NV-SF026 | | Needle Valve-$N_2$ pannel vent valve | ¼" Needle Valve, 0.37 Cv, 5000 Psi | Swagelok | SS-1RS4 |
| PT-SF027 | | Pressure Transducer - Feed Line Incoming | 0-3000 Psi | Dywer Instruments | 628-18-GH-P2-E1-S4 |
| REG-SF028 | | Manual Pressure Regulator - Valve Actuation | 0-500 Psi | Tescom | 26-1064-24 |
| AG-SF029 | | Analog Gauge - Valve Actuation | 0-600 Psi | Omega | |
| MDV-SF030 | | 3-Way Manual Diverter Valve - Valve actuation dome hand valve | 1/4"; 4800 Psi | Hylok | H1B3S-H4TPC |
| RV-SF031 | | Relief Valve - Valve Actuation | 1/4" NPT; 150 Psi; 12/15/2017 | Hylok | RV1MF-4N-S316 |
| REG-SF032 | | Manual pressure Regulator - Positioner Valves | 1/8"; 0-100 Psi | Porter | 8310 |
| AG-SF033 | | Analog Gauge - Positioner Valve | 1/8"; 0-100 Psi | U.S. Gauge | |
| PBV-SF034 | | Pneumatic Ball Valve - Gas Sim Run | 3/4"; 6000 Psi | Parker | 12Z(A)-B8LJ2-SS-62AC-3 |
| MDV-SF035 | | 3-Way Manual Diverter Valve - ASF/HPSF | 3/4"; 4000 Psi | Hylok | H2B3B-H12TPC |
| PBV-SF036 | | Pneumatic Ball Valve - Window/Curtain Run | 3/4"; 6000 Psi | Parker | 12Z(A)-B8LJ2-SS-62AC-3 |
| NV-SF037 | | Needle Valve - Window Curtain | 1/2 " | Hylok | NV4H-8T-S316 |
| PDV-SF038 | | Pneumatic Ball Valve - Run Tank Pressure/Vent | 1/2"; 6000 Psi | Parker | 8Z(A)-B8XJ2-V-SS-61ADX |
| MBV-SF039 | | 3 way Manual Ball Valve – Run Tank 3-way hand ball valve | 1/2"; 0-4800 Psi | Hy-lok | H1B3B-H8TPC |
| PT-SF040 | | Pressure Transducer - Pressurized Run Tank | 0-3000 Psi | Honeywell | FPG1DN |
| AG-SF041 | | Analog Gauge - Pres. Run Tank | 0-3000 Psi | Span | 02-0359-D |
| RV-SF042 | | Relief Valve - Pressurized Run Tank | 1/2" NPT; 2050 Psi; 12/15/2017 | Hylok | RV2MH-8N8T-C-S316 |
| BD-SF043 | | Burst Disk – Pressurized Run Tank | 1/2"; 2100 Psi | Fike | SCRD |
| RT-SF044 | | Pressurized Run Tank | 60 gal.; 2000 Psi | Prentex | D220-2007 |
| MBV-SF045 | | Manual Ball Valve - Pump 1 | 1/2"; 6000 Psi | Parker | 8ZA-B8L-T-SS-V-ACT |
| MBV-SF046 | | Manual Ball Valve - Drain | 1/2"; 6000 Psi | Parker | 8Z(A)-B8LS2-EPR-SSP-C3 |

| Labels | No. | Component | Description | Manufacturer | Model |
|---|---|---|---|---|---|
| MBV-SF047 | | Manual Ball Valve - Pump 2 | 1/2"; 6000 Psi | Parker | 8Z(A)-B8LS2-EPR-SSP-C3 |
| PUMP-SF048- | | Pump - Water Tank | 1/10 HP | Little Giant | 977442 E40513 |
| TANK-SF049 | | Water Tank | 300 gallons | Ace | |
| FILT-SF050 | | Filter - Water Tank | 300 gal./day | AquaFX | Mak-50-CBF-CC-10-2 |
| MBV-SF051 | | Manual Ball Valve - Liquid Line | 1"; 2200 Psi | Swagelok | SS-65TS16 |
| PBV-SF052 | | Pneumatic Ball Valve - Liquid Sim Run | 1" 2500 Psi | Whitey | SS-65PF16 |
| MBV-SF053 | | Manual Ball Valve - Chamber Loop | 1/2"; 6000 Psi | Hylok | H1B-H-8TPC |
| MBV-SF054 | | Manual Ball Valve - ASF Loop | 1/2"; 6000 Psi | Hylok | H1B-H-8TPC |
| PGV-SF055 | | Globe Valve - Gas | 1 1/4" NPT; 1930 Psi | Jordan Valve | 8000G |
| PBV-SF056 | | Pneumatic Ball Valve - Chamber Gas Vent | 3/4"; 6000 Psi | Parker | 12Z(A)-B8LJ2-SS-62AC-3 |
| PGV-SF057 | | Globe Valve - Liquid | 3/4" NPT; 4000 Psi | Jordan Valve | 708SP |
| PBV-SF058 | | Pneumatic Ball Valve - Chamber Liquid Vent | 3/4"; 6000 Psi | Parker | 12Z(A)-B8LJ2-SS-62AC-3 |
| OR-SF070 | | Orifice- main vent | | | |
| FILT-SF071 | | Filter inline with pump | | | |
| MBV-SF072 | | Manual Ball valve- venturi table | 1" | Hy-lok | |
| MBV-SF073 | | Manual ball valve- atmospheric bench liquid sim | ½" | Hy-lok | |
| AG-SF074 | | Analog Gauge - High-Pressure Chamber | 0-600 Psi | Duragauge | |
| PT-SF075 | | Venturi upstream transducer | 0-3000 PSI | Honeywell | |
| TC-SF076 | | Venturi upstream thermocouple | K-type | Omega | |
| OR-SF077 | | Mass Flow Venturi | 0.186 inch diameter | Fox | |
| PT-SF078 | | Sample upstream transducer | 0-1500 PSI | Honeywell | |
| TC-SF079 | | Sample upstream thermocouple | K-type | Omega | |
| TA-SF080 | | PHYDRA Test Article | | | |
| PT-SF081 | | Sample Downstream transducer | 0-750 PSI | Honeywell | |
| TC-SF082 | | Sample Downstream Thermocouple | K-type | Omega | |
| PT-SF083 | | Second Sample Downstream transducer | 0-750 PSI | Honeywell | |

APPENDIX F.    Spray Facility Schematic
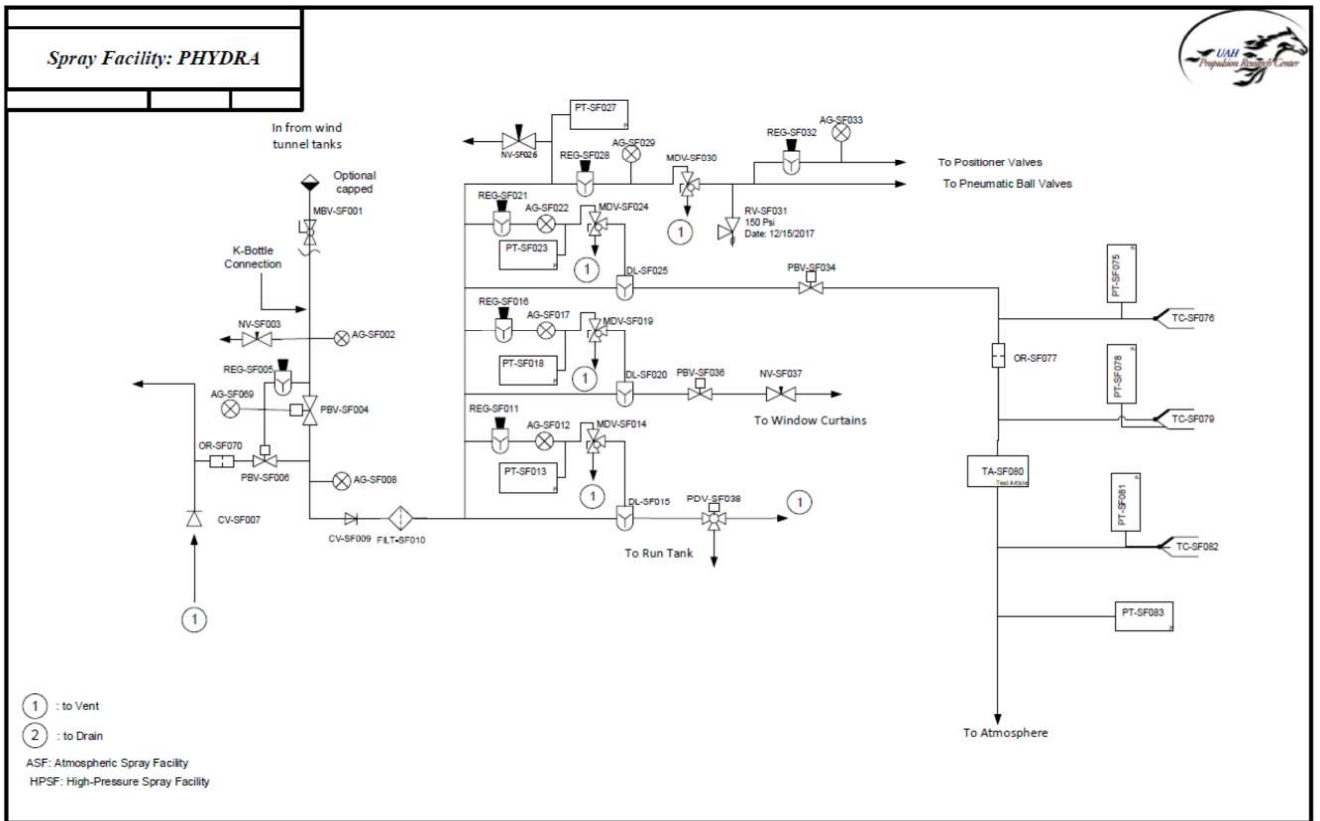
APPENDIX G.    Emergency Contact Numbers

In the event of an emergency, respond in accordance with off-nominal procedures defined in this SOP and in accordance with the appropriate section in the UAH PRC Safety Program dated, 22-Feb-2013.

| Emergency Phone Numbers | |
| --- | --- |
| Police | 911 |
| Fire Department | (256) 824-6911 |
| Hazardous Materials Incident | (6911 from campus phone) |
| Utility Failure | |
| **PRC Contacts** | |
| Tony Hall | Office : (256) 824-2887 <br> Cell: 256-425-1975 |
| David Lineberry | Office : (256) 824-2888 <br> Cell:    (256) 348-8978 |
| Robert Frederick | Office : (256) 824-7200 <br> Cell:    (256) 503-4909 |
| PRC Main Office | (256) 824-7209 |
| High Pressure Lab Phone | (256) 824-6031 |
| JRC Test Stand | (256) 824-2857 |
| Kristy Olive/OEHS (Office of Environmental Health and Safety) | (256) 824-6053 <br> Mobile: (256)335-3425 |
| **Other Emergency Numbers of Interest** | |
| UAH Campus Police Department | (256) 824-6911 |
| Huntsville Police Department | (256) 722-7100 |
| Madison County Sheriff's Office | (256) 722-7181 |
| Alabama State Troopers | (334) 242-4371 |
| Huntsville Hospital | (256) 265-1000 |

**In the event of a non-emergency reportable incident call the numbers below in the following order.**

1. **Dr. Robert Frederick**
   **(Dr. David Lineberry as an alternate)**
   **Office: (256) 824-7200**
   **Cell: (256) 503-4909**
2. **UAH Police (Non-Emergency)**
   **(256) 824-6596**
   **6596 (from campus phone)**

# APPENDIX B

# POROUS HYBRID HOLDER DRAWING



**Figure B.1**: PhYdra Assembly

# REFERENCES

*The secret of creativity is knowing how to hide your sources.*

—Albert Einstein

[1] George P. Sutton. *Rocket Propulsion Elements*. John Wiley and Sons, Inc., New York, 6th edition, 1992.

[2] Whitehead J.J. Knox L.R. Frederick Jr., R.A. and M.D. Moser. Regression rates of mixed hybrid propellants. *AIAA Journal of Propulsion and Power*, 23(1), Jan-Feb 2007.

[3] Okada K. San'da T. Kato T. Akiba R. Satori S. Nagata, H and I. Kudo. Combustion characteristics of fibrous fuels for dry towel hybrid rocket motor. *Journal of Space Technology and Science*, 13(1):11–16, 1997.

[4] B.N. Cassenti, G.J. Nelson, M.B. DeGostin, A.A. Peracchio, and W.K.S. Chiu. Analytical solutions for extended surface electrochemical fin models. *Journal of Power Sources*, 265:282–290, 2014.

[5] A. Cocco, A. Nakajo, and W.K.S. Chiu. Analytical transport network theory to guide the design of 3-d microstructural networks in energy materials: Part 1. flow without reactions. *Journal of Power Sources*, 372:297–311, 2017.

[6] S. Brunauer, P.H. Emmett, and E. Teller. Adsorption of gases in multimolecular layers. *Journal of the American Chemical Society*, 60(2):309–319, 1938.

[7] M. Tanzi and S. Fare. *Characterization of Polymetric Biomaterials*. Woodhead Publishing, Cambridge, MA, 2017.

[8] G. Nelson. Abstract z-99-99. In *17th U.S. National Congress on Theoretical and Applied Mechanics*, Tucson, Arizona, June 15-20 2014.

[9] Joseph R. Buckley, Robin White, and George J. Nelson. Experimental validation of the x-ray determined pore size distribution of porous hybrid motor grains. In $55^{th}$ *AIAA Propulsion and Energy Forum*, number AIAA 2019-4097, Indianapolis, IN, 2019. American Institute of Aeronautics & Astronautics.

[10] George J. Nelson, Aldo A. Peracchio, and Wilson K.S. Chiu. Analytical investigations of varying cross section microstructures on charge transfer in solid oxide fuel cell electrodes. *Journal of Power Sources*, 196(10):4695 – 4704, 2011.

[11] Enno T. de Vries, Amir Raoof, and Martinus Th. van Genuchten. Multiscale modelling of dual-porosity porous media; a computational pore-scale study for flow and solute transport. *Advances in Water Resources*, 105:82 – 95, 2017.

[12] Seungkwan Baek, Woosuk Jung, Hongjae Kang, and Sejin Kwon. Development of high-performance green-monopropellant thruster with hydrogen peroxide and ethanol. *Journal of Propulsion and Power*, 34(5):1256–1261, September 2018.

[13] L. Werling, F. Lauck, D. Freudenmann, N. Rocke, H. Ciezki, and S. Schlechtriem. Experimental investigation of the flame propagation and flashback behavior of a green propellant consisting of n2o and c2h4. *Journal of Energy and Power Engineering*, (11):735–752, 2017.

[14] L. Ya. Paderin, P.V. Prosuntsov, S.V. Reznik, and V. P. P. Fisher. Experimental study of the heat transfer in porous semitransparent heat-shield materials. *Journal of Engineering Physics and Thermophysics*, 78(1):60–67, Jan 2005.

[15] Matthew Hitt. *Regression Rate Study of Porous Axial-Injection, End-Burning Hybrid Fuel Grains*. PhD thesis, University of Alabama in Huntsville, 2016.

[16] Yuji Saito, Toshiki Yokoi, Lukas Neumann, Hiroyuki Yasukochi, Kentaro Soeda, Tsuyoshi Totani, Masashi Wakita, and Harunori Nagata. Investigation of axial-injection end-burning hybrid rocket motor regression. *Advances in aircraft and spacecraft science*, 4:281–296, 05 2017.

[17] Stephen D. Heister, William E. Anderson, Timothee L. Pourpoint, and R. Joseph Cassady. *Rocket Propulsion*. Cambridge University Press, New York, 1st edition, 2019.

[18] Y. Hirata, S. Aso, T. Hayashida, R. Nakawatase, Yasuhiro Tani, K. Morishita, and Toru Shimada. Improvement of regression rate and combustion efficiency of high density polyethylene fuel and paraffin fuel of hybrid rockets with multi-section swirl injection method. In *47th AIAA/ASME/SAE/ASEE Joint Propulsion Conference*, San Diego, CA, 07 2011.

[19] Kengo Ohe, Sho Oyama, Kentaro Araki, Shigeru Aso, Yasuhiro Tani, and Toru Shimada. Study on hybrid rocket with multi-section swirl injection method toward flight experiments of subscale space plane. In *50th AIAA/ASME/SAE/ASEE Joint Propulsion Conference*, Cleveland, OH, 2014.

[20] Hiroshi Tada, Shigeru Aso, Yasuhiro Tani, Sho Oyama, Kentaro Araki, and Toru Shimada. In *50th AIAA/ASME/SAE/ASEE Joint Propulsion Conference*, July 2014.

[21] M. McFarland and E. Antunes. Small-scale static fire tests of 3d printing hybrid rocket fuel grains produced from different materials. *Aerospace*, 6(7), July 2019.

[22] Alex P. Cocco and Kyle N. Grew. Analytical Transport Network Theory for Onsager, Coupled Flows: Part 1—Channel-Scale Modeling of Linear, Electrokinetic Flow. *Journal of Electrochemical Energy Conversion and Storage*, 18(2), 07 2020.

[23] Alex P. Cocco and Kyle N. Grew. Analytical Transport Network Theory for Onsager, Coupled Flows: Part 2—Network-Scale Modeling of Linear, Electrokinetic Flow. *Journal of Electrochemical Energy Conversion and Storage*, 18(2), 07 2020.

[24] Alex P. Cocco and Kyle N. Grew. Analytical transport network theory structural mechanics: Towards computationally inexpensive multi-functional materials design. *Applied Materials Today*, 20:100674, 2020.

[25] S. R. Turns. *An Introduction to Combustion: Concepts and Applications.* McGraw-Hill, Inc., Boston, 2 edition, 2000.

[26] R. Byron Bird, Warren E. Stewart, and Edwin N. Lightfoot. *Transport Phenomena.* John Wiley and Sons, Inc., New York, 2nd edition, 2007.

[27] Henry Darcy. *Les Fontaines Publiques de la Ville de Dijon.* Dalmont, Paris, Paris, France, 1856.

[28] P. Forchheimer. Wasserbewegung durch boden (water movement through the ground). *Z. Ver. Deutsch.Ing.*, 45:1782–1788, 1901.

[29] S. Ergun. Fluid flow through packed columns. *Chemical Engineering Progress*, 48:89–94, 1952.

[30] Esra Erdim, Ömer Akgiray, and İbrahim Demir. A revisit of pressure drop-flow rate correlations for packed beds of spheres. *Powder Technology*, 283:488–504, October 2015.

[31] J.K. Jones and H. Krier. Gas flow resistance measurements through packed beds at high reynolds numbers. *ASME J. Fluids Eng.*, pages 168–172, 1983.

[32] J.A. Tallmadge. Packed bed pressure drop-an extension to higher reynolds numbers. *AIChe J.*, 16:1092–1093, 1970.

[33] L.S. Lee and K. Ogawa. Pressure drop through packed bed. *J. Chem Eng. Jpn.*, 27:691–693, 1994.

[34] Benjamin Dietrich, Wilhelm Schabel, Matthias Kind, and Holger Martin. Pressure drop measurements of ceramic sponges- determining the hydraulic diameter. *Chemical Engineering Science*, 64:3633–3640, May 2009.

[35] Po-Wei Li, Wen Chen, Zhuo-Jia Fu, and Chia-Ming Fan. Generalized finite difference method for solving the double-diffusive natural convection in fluid-saturated porous media. *Engineering Analysis with Boundary Elements*, 95:175 – 186, 2018.

[36] Bigyani Das, Stanly Steinberg, Susan Weber, and Steve Schaffer. Finite difference methods for modeling porous media flows. *Transport in Porous Media*, 17:171–200, 08 1994.

[37] Roland W. Lewis and Peter M. Roberts. *The Finite Element Method in Porous Media Flow*. Springer Netherlands, Dordrecht, 1984.

[38] Johannes Korsawe, Gerhard Starke, Wenqing Wang, and Olaf Kolditz. Finite element analysis of poro-elastic consolidation in porous media: Standard and mixed approaches. *Computer Methods in Applied Mechanics and Engineering*, 195(9):1096 – 1115, 2006.

[39] Richard E. Ewing. Finite element methods for nonlinear flows in porous media. *Computer Methods in Applied Mechanics and Engineering*, 51(1):421 – 439, 1985.

[40] Edo S. Boek and Maddalena Venturoli. Lattice-boltzmann studies of fluid flow in porous media with realistic rock geometries. *Computers  Mathematics with Applications*, 59(7):2305 – 2314, 2010.

[41] Ehsan Fattahi, Christian Waluga, Barbara Wohlmuth, Ulrich Rüde, Michael Manhart, and Rainer Helmig. Lattice boltzmann methods in porous media simulations: From laminar to turbulent flow. *Computers  Fluids*, 140:247 – 259, 2016.

[42] S. Bakhshian, S.A. Hosseini, and N. Shokri. Pore-scale characteristics of multiphase flow in heterogeneous porous media using the lattice boltzmann method. *Sci. Rep*, 1(3377):1–13, March 2019.

[43] George J. Nelson, Brice N. Cassenti, Aldo A. Peracchio, and Wilson K.S. Chiu. Two-dimensional charge transfer and space charge effects in extended surface solid oxide fuel cell electrodes. *Journal of Power Sources*, 205:48 – 56, 2012.

[44] George J. Nelson, A. Nakajo, B.N. Cassenti, and M.B. et al. Degostin. A rapid analytical assessment tool for three dimensional electrode microstructural networks with geometric sensitivity. *Journal of Power Sources*, 246:322–334, 2014.

[45] George J. Nelson, Brice N. Cassenti, Aldo A. Peracchio, and Wilson K. S. Chiu. Microstructural effects on electronic charge transfer in li-ion battery cathodes. 159(5):A598–A603, 2012.

[46] George J. Nelson, Brice N. Cassenti, Aldo A. Peracchio, and Wilson K.S. Chiu. An analytical method for dye-sensitized solar cell geometric design. *Electrochimica Acta*, 90:475 – 481, 2013.

[47] T. Bergman, A. Lavine, F. Incropera, and D. Dewitt. *Fundamentals of Heat and Mass Transfer*. John Wiley and Sons, Inc., Hoboken, New Jersey, 7th edition, 2012.

[48] ASTM. Test methods for apparent porosity water absorption apparent specific gravity and bulk density of burned refractory brick and shapes by boiling water. Technical report, ASTM International.

[49] S. Shukla, F. Wei, M. Mandal, J. Zhou, M. S. Saha, J. Stumper, and M. Secanell. Determination of PEFC gas diffusion layer and catalyst layer porosity utilizing archimedes principle. *Journal of The Electrochemical Society*, 166(15):F1142–F1147, 2019.

[50] John A et al. Slotwinski. Porosity measurements and analysis for metal additive manufacturing process control. *Journal of research of the National Institute of Standards and Technology*, 119:494–528, September 2014.

[51] Beat Munch and Lorenz Holzer. Contradicting geometrical concepts in pore size analysis attained with electron microscopy and mercury intrusion. *Journal of the American Ceramic Society*, 91(12):4059–4067, December 2008.

[52] Irving Langmuir. The constitution and fundamental properties of solids and liquids. part i. solids. *Journal of the American Chemical Society*, 38(11):2221–2295, 1916.

[53] Irving Langmuir. The constitution and fundamental properties of solids and liquids. part ii. liquids. *Journal of the American Chemical Society*, 39(9):1848–1906, 1917.

[54] Hans Swenson and Nicholas P. Stadie. Langmuir's theory of adsorption: A centennial review. *Langmuir*, 35(16):5409–5426, 2019.

[55] J. Rouquerol, P. Llewellyn, and F. Rouquerol. Is the bet equation applicable to microporous adsorbents? In P.L. Llewellyn, F. Rodriquez-Reinoso, J. Rouqerol, and N. Seaton, editors, *Characterization of Porous Solids VII*, volume 160 of *Studies in Surface Science and Catalysis*, pages 49 – 56. Elsevier, 2007.

[56] Krista S. Walton and Randall Q. Snurr. Applicability of the bet method for determining surface areas of microporous metalorganic frameworks. *Journal of the American Chemical Society*, 129(27):8552–8556, 2007.

[57] H.J. Haugen and S. Bertoldi. *Characterization of Polymeric Biomaterials*. Elsevier, New York, 2017.

[58] E. Washburn. The dynamics of capillary flow. *Physical Review*, 17(3):273–283–72, Mar 1921.

[59] C. Causserand and P. Aimar. Characterization of filtration membranes. In *Comprehensive Membrane Science and Engineering*, pages 311–335. Elsevier, 2010.

[60] T. L. BOGGS and K. J. KRAEUTLE. Role of the scanning electron microscope in the study of solid rocket propellant combustion, i. ammonium perchlorate decomposition and deflagration. *Combustion Science and Technology*, 1(2):75–93, 1969.

[61] JAMES E. CRUMP, JACK L. PRENTICE, and KARL J. KRAEUTLE. Role of the scanning electron microscope in the study of solid propellant combustion: Ii. behavior of metal additivest. *Combustion Science and Technology*, 1(3):205–223, 1969.

[62] Elton N. Kaufmann, editor. *Characterization of materials*. John Wiley & Sons, Inc, Hoboken, New Jersey, second edition edition, 2012.

[63] A-N. Zayed and B. Lawton. Methods of measuring the burning rate in solid rockets by usig the computed tomography technique. In *31st AIAA/AS-ME/SAE/ASEE Joint Propulsion Conference and Exhibit*, number AIAA 95-2594, San Diego, California, 1995. American Institute of Aeronautics and Astronautics.

[64] George J. Nelson, K.N. Grew, J.R. Izzo Jr., and J.J. et al. Lombardo. Three-dimensional microstructural changes in the ni-ysz solid oxide fuel cell anode during operation. *Acta Materialia*, 60:3491–3500, 2012.

[65] T.J. Heindel. X-ray imaging techniques to quantify spray characteristics in the near field. *Atomization and Sprays*, 28(11):1029–1059, 2018.

[66] B.R. Halls, T.J Heindel, T.R. Meyer, and A.L. Kastengren. X ray spray diagnostics: Comparing sources and techniques. In *50th AIAA Aerospace Sciences Meeting and Exhibit*, number AIAA 2012-1055, Nashville, TN, 2012. American Institute of Aeronautics and Astronautics.

[67] D.P. Finegan, M. Scheel, J.B. Robinson, and B. et al. Tjaden. In-operando high-speed tomography of lithium-ion batteries during thermal runaway. *Nature Communications*, 6(6924):1–10, 2015.

[68] M. Ebner, F. Geldmacher, F. Marone, and M. et al. Stampanoni. X-ray tomobraphy of porous, transition metal oxide based lithium ion battery electrodes. *Advanced Energy Materials*, 3(7):845–850, 2013.

[69] W. Harris, J. Lombardo, and G.J. et al. Nelson. Three-dimensional microstructural imaging of sulfur poisoning-induced degradation in a ni-ysz anode of solid oxide fuel cells. *Sci. Rep.*, 4:1–7, 2014.

[70] S. Gallier and F. Hiernard. Microstructure of composite propellants using simulated packings and x-ray tomography. *Journal of Propulsion and Power*, 24(1):147–150, Jan-Feb 2008.

[71] N. Kardjilov, I. Manke, A. Hilger, M Strobl, and J. Banhart. Neutron imaging in materials science. *Materials Today*, pages 248–256, June 2011.

[72] Daisuke Ito, Yasushi Saito, and H. et al. Kagawa. Visualization of hydrazine decomposition in a catalyst bed by using neutron radiography. *Physics Procedia*, 69:577–582, September 2015.

[73] H. Kagawa, N. Saitoh, and K. et al. Kajiwara. Neutron radiography used on a mono-propellant thruster. In *47th AIAA/ASME/SAE/ASEE Joint Propulsion Conference and Exhibit*, number AIAA 2011-5841, San Diego, California, 2011. American Institute of Aeronautics and Astronautics.

[74] K. Kushiki, H. Kagawa, T. Nagata, K. Kajiwara, and M. Matsubayashi. Visualization of propellant behavior inside catalyst thruster using neutron radiography. In *45th AIAA/ASME/SAE/ASEE Joint Propulsion Conference and Exhibit*, number AIAA 2009-4972, Denver, Colorado, 2009. American Institute of Aeronautics and Astronautics.

[75] E.E. Looney, G.J. Nelson, Z.K. Van Zandt, and Y. et al. Ulyanova. Ex situ and in situ neutron imaging of enzymatic electrochemical cells. *Electrochimica Acta*, 213:244–251, 2016.

[76] E.H Lehmann, P Vontobel, and N Kardjilov. Hydrogen distribution measurements by neutrons. *Applied Radiation and Isotopes*, 61(4):503–509, oct 2004.

[77] L.F. Gladden, M.H.M. Lim, M.D. Mantle, A.J. Sederman, and E.H. Stitt. Mri visualisation of two-phase flow in structured supports and trickle-bed reactors. *Catalysis Today*, 79-80:203 – 210, 2003. Catalysis in Multiphase Reactors.

[78] N.L. Nguyen, V. van Buren, A. von Garnier, E.H. Hardy, and R. Reimert. Application of magnetic resonance imaging (mri) for investigation of fluid dynamics in trickle bed reactors and of droplet separation kinetics in packed beds. *Chemical Engineering Science*, 60(22):6289 – 6297, 2005. 7th International Conference on Gas-Liquid and Gas-Liquid-Solid Reactor Engineering.

[79] Joseph R. Buckley and George J. Nelson. Computed tomography characterization of a porous hybrid motor grain with added contrast agent. In 52$^{\text{cd}}$ *AIAA/ASME/SAE/ASEE Joint Propulsion Conference & Exhibit*, number AIAA 2016-4870, Salt Lake City, UT, 2016. American Institute of Aeronautics & Astronautics.

*Ph.inisheD.*

—